Review Article

Electromagnetic Radiations from Heavy Ion Collision

Payal Mohanty,[1,2] Sabyasachi Ghosh,[2,3] and Sukanya Mitra[2]

[1] *HENPP Division, Saha Institute of Nuclear Physics, 1/AF Bidhan Nagar, Kolkata 700064, India*
[2] *Theoretical Physics Division, Variable Energy Cyclotron Centre, 1/AF Bidhan Nagar, Kolkata 700064, India*
[3] *Ctr. for Astroparticle Physics and Space Bose Institute, 5/EN Bidhan Nagar, Kolkata 700091, India*

Correspondence should be addressed to Payal Mohanty; payal.mohanty@saha.ac.in

In this review, we have discussed the different sources of photons and dileptons produced in heavy ion collision (HIC). The transverse momentum (p_T) spectra of photons for different collision energies are analyzed with a view of extracting the thermal properties of the system formed in HIC. We showed the effect of viscosity on p_T spectra of produced thermal photons. The dilepton productions from hot hadrons are considered including the spectral change of light vector mesons in the thermal bath. We have analyzed the p_T and invariant mass (M) spectra of dileptons for different collision energies too. As the individual spectra are constrained by certain unambiguous hydrodynamical inputs, so we evaluated the ratio of photon to dilepton spectra, R_{em}, to overcome those quantities. We argue that the variation of the radial velocity extracted from R_{em} with M is indicative of a phase transition from the initially produced partons to hadrons. In the calculations of interferometry involving dilepton pairs, it is argued that the nonmonotonic variation of HBT radii with invariant mass of the lepton pairs signals the formation of quark gluon plasma in HIC. Elliptic flow (v_2) of dilepton is also studied at $\sqrt{s_{NN}} = 2.76$ TeV for 30–40% centrality using the $(2 + 1)d$ hydrodynamical model.

1. Introduction

The main objective of relativistic heavy ion collisions is to study the transient phase, that is, *quark gluon plasma* (QGP) which is believed to permeate the early universe a few microseconds after the *Big Bang*. Collision between nuclei at ultrarelativistic energies produces charged particles either in hadronic or in partonic state depending on the collision energy. Interaction among these charged particles produces electromagnetic (EM) radiation [1–9]. However, hadrons being strongly interacting objects give snapshot of evolution only from the freezeout surface. So they have hardly any information about the interior of the plasma. Whereas EM radiations, for example, the thermal photons and dileptons, are expected to provide an accurate information about the initial condition and the history of evolution of the plasma. This is possible since photons and dileptons interact only through the EM interaction. The EM interaction strength is small compared to that of strong interaction ($\alpha \ll \alpha_s$) and thus dominates the dynamics of nuclear collision processes. Therefore, its mean free path ($\lambda = 1/n\sigma$) is larger than

the size of the system. Because of their negligible final-state interactions with the hadronic environment, once produced it brings the electromagnetic particles about to escape unscathed carrying the clean information of all stages of the collision. The EM radiations produce all stages of collision process which contribute to the measured photon spectra; in principle, a careful analysis may be useful to uncover the whole space-time history of nuclear collision. Hence EM radiations—real and the virtual photons (dilepton)—are considered as efficient probes to study dynamical evolution of the matter formed in relativistic heavy ion collision. However, as they are emitted continuously, they sense in fact the entire space-time history of the reaction. This expectation has led to an intense and concerted efforts toward the identification of various sources of such radiations. While initially these signals were treated as *thermometer* of the dense medium created, but later on recent calculations suggest it might serve as *chronometer* [10] and *flow-meter* [11–16] of HIC.

The review is organized as follows. In Section 2, we start with possible sources of photons and dileptons that were produced in HIC. We have discussed the formalism of static

emission rate of photons and dileptons in Section 3. To get total yield, we need concept of hydrodynamics. So, we briefly outlined relativistic hydrodynamics in Section 4 which takes care of the evolution. In Section 5 we have presented the thermal emission rate of photons from QGP (Section 5.1) and hadronic matter (Section 5.2) which is used to produce the results, and total invariant yield of direct photon for different collision energy is shown in Section 5.4. The effect of viscosity on the transverse momentum (p_T) spectra of photon is discussed in Section 5.5. Similarly, the details of the emission rate of dileptons from QGP and hot hadrons are given in Sections 6.1 and 6.2, respectively. Using these rates, the results of p_T and invariant mass (M) spectra of dileptons are presented in Section 6.4. In Section 7 the radial flow is extracted by simultaneous use of p_T spectra of photons and dileptons and ratio of the spectra, and R_{em} is conferred. The correlation function for dilepton has been calculated and HBT radii are extracted as function of M in Section 8. We have also evaluated the dilepton v_2 in Section 9 taking into account the medium effect on the spectral function of the vector mesons. Finally, we have summarized the work in Section 10.

2. Various Sources of EM Radiations

As argued previously that EM radiations emerge out copiously from all stages of collision, so, in order to proceed, it is useful to identify various sources of photons and dileptons produced in the HIC. So the "inclusive" photon spectrum coming from such collision in usual sense can be defined as the unbiased photon spectrum observed in pp, pA, or AA collision. This spectrum is built up from a cocktail of various components.

Depending on their origin, there are two different types of sources which are "direct photons" and "photons from decay of hadrons." The term "direct photons" is meant for those photons and dileptons which produce directly from collision between the particles. One can subdivide this broad category of "direct photons" into "prompt photons," "preequilibrium photons" and "thermal photons," depending on their origin. On the other hand, the decay photons do not come directly from the collision, rather from the decay of hadrons.

2.1. Transverse Momentum (p_T) Dependence of EM Radiations. The EM spectra provided by the experimentalist are mingled with various sources of photons and dileptons and it is difficult to distinguish different sources experimentally. However, real interest lies in the thermal photons and dileptons since it is expected to render information about the initial condition and the history of evolution of the plasma while it cools and hadronizes. Thus, theoretical models are used with great advantage to identify these sources of photons and their relative importance and characteristics in the spectrum.

Depending on the process through which photons/dileptons produce, they are categorized as follows.

(1) *Prompt*: the EM radiations produced by hard scattering of the partons inside the nucleons of incoming nuclei in the initial stage of collision, before the thermalization sets in, are known as prompt photons and dileptons (Drell Yan). This contribution may be evaluated by using pQCD.

(2) *Preequilibrium*: the *preequilibrium photons and dileptons* are produced in the preequilibrium stage, that is, before the thermalization sets in the system. In such scenario the contribution from preequilibrium stage will be very small and hence neglected.

(3) *Thermal*: EM radiations which are emitted from the thermalized systems of quarks and gluons or hadronic gas.

(4) *Decay*: after the freezeout of the fireball, photons and dileptons are also produced from the decays of long-lived (compared to strong interaction time scale) hadrons and known as "*photons from decay.*"

Out of different sources, the thermal photons and dileptons are privileged as they carry information about the formation of QGP. As indicated in Figure 1, the hard photons dominate the high p_T part of the invariant momentum spectra, and decay photon populates the low p_T part and rest over thermal contribution shines in the intermediate domain of the p_T spectra ~1–3 GeV. And the calculations based on theory infer that the photons and lepton pairs from hadronic matter dominate the spectrum at lower p_T (~1-2 GeV) whereas photons and dileptons form QGP dominate in the intermediate p_T range, that is, p_T ~ 2-3 GeV (depending on the models) [17]. This small window may help in learning the properties of QGP. Thus one has to subtract out the nonthermal sources to understand the properties of the QGP. However, it is not possible experimentally to distinguish between different sources. Thus, theoretical models and calculations can be used to great advantage to identify different sources of direct photons and their relative importance and characteristics in the spectrum. The hard photons and dileptons are well understood in the framework of pQCD, and decay contributions can be filtered out experimentally using different subtraction methods, like invariant mass analysis, mixed event analysis, internal conversion method, and so forth.

The invariant momentum distribution of photons and dileptons produce from a thermal source depends on the temperature (T) of the source through the thermal phase space distributions of the participants of the reaction that produces the photons and dileptons [18]. As a result the p_T spectra of thermal photons and dileptons reflect the temperature of the source through the phase space factor ($e^{-E/T}$). Hence ideally the photons with intermediate p_T values (~2-3 GeV, depending on the value of initial temperature) reflect the properties of QGP (realized when $T > T_c$, T_c is the transition temperature). Therefore, one should look into the p_T spectra for these values of p_T for the detection of QGP. However, for an expanding system the situation is far more complex. The thermal phase space factor changes by flow; for example, the transverse kick received by low p_T photons due to flow originating from the low temperature hadronic phase (realized when $T < T_c$) populates the high p_T part of the
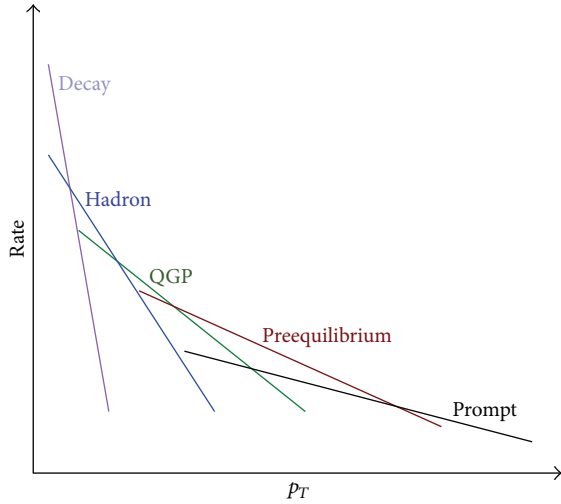
FIGURE 1: Schematic diagram of different sources of photon production in heavy ion collision as function of transverse momentum (p_T).

FIGURE 2: Expected different sources of dilepton production in HIC as function of invariant mass [5].

spectra [19]. As a consequence the intermediate or the high p_T part of the spectra contains contributions from both QGP and hadrons. Thus, it is not an easy task to disentangle the photons coming from pure partonic phase. Thus photons appear to be a more restrictive probe since they are characterized only by their momentum whereas the dileptons have two kinematic variable, p_T and invariant mass (M) to play with. A soft photon (low p_T) in one frame of reference can be hard (high p_T) in another frame, whereas the p_T integrated invariant mass distribution of dileptons is independent of any frame. In addition to it the p_T spectra are affected by the flow; however, the p_T integrated M spectra remain unaltered by the flow in the system. Also in the M spectra of dileptons, again in M spectra, the dileptons from QGP dominates over its hadronic counterpart above the ϕ peak. All these suggests that a judicious choice of p_T and M windows will be very useful to characterize the QGP and hadronic phase separately.

2.2. Invariant Mass (M) Dependence of EM Radiations. Being massive, dileptons make situation different from photons. They have two kinematic variables—p_T and M. As argued before, the p_T spectra are affected by the flow; however, the p_T-integrated M spectra remain unaltered by the flow in the system. It should be mentioned here that for M below ρ peak and above ϕ peak dileptons from QGP dominates over its hadronic counterpart (assuming the contributions from hadronic cocktails are subtracted out) if the medium effect of spectral function of the low mass vector mesons are not taken into account. However, the spectral function of low mass vector mesons (mainly ρ) may shift toward lower invariant mass region due to nonzero temperature and density effects. As a consequence the contributions from the decays of ρ mesons to lepton pairs could populate the low M window and may dominate over the contributions from the QGP phase [5, 8, 20]. All these suggest that the invariant mass distribution of dilepton can be used as a clock for HIC, and a
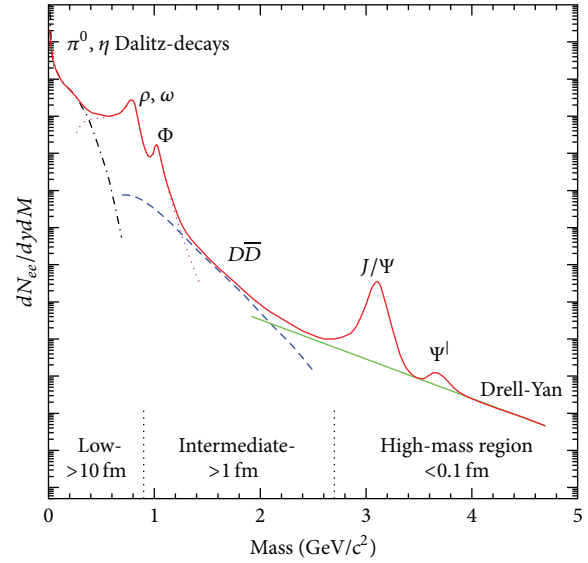
judicious choice of p_T and M windows will be very useful to characterize the flow in QGP and hadronic phase.

The measured dilepton spectra can be divided into several phases. Depending on the invariant mass of the emitted dileptons, it can be classified into three distinct regimes (discussed below [5]), and a schematic diagram of dilepton mass distribution is shown in **Figure 2**.

(i) High mass region (HMR):

$$\left(M \geq M_{J/\Psi} \left(= 3.1\,\text{GeV}\right), p_T \sim 3\text{–}5\,\text{GeV}\right). \qquad (1)$$

The HMR region corresponds to early preequilibrium phase ($\tau < \tau_i$), where the lepton pairs are produced with large invariant mass ($M > 3$ GeV) and the dominant contributions are from the hard scattering between the partons, like Drell Yan annihilation [21, 22]. The final abundance of the heavy quarkonia ($J/\Psi, \Upsilon$) and their contribution to the spectrum is suppressed due to the Debye screening and as a result the bound states are dissolved.

(ii) Intermediate mass region (IMR):

$$\left(M_\phi \leq M \leq M_{J/\Psi}, p_T \sim 1\text{–}3\,\text{GeV}\right). \qquad (2)$$

Thermalization is achieved in the system after a time scale ($> \tau_i$). In this domain, the dileptons from the QGP are produced via quark-antiquark annihilation. In this regime, due to higher temperature the continuum radiation from QGP dominates the dilepton mass spectrum and thus this region is important for the detection of QGP. The decays of "open charm" mesons, that is, pairwise produced $D\bar{D}$ mesons [23] followed by semileptonic decays, contribute largely in this domain of M. Although an enhanced charm production is interesting in itself—probably related to the very early collision states—it may easily mask the thermal plasma

signal. To somewhat lesser extent, this also holds true for the lower-mass tail of Drell-Yan production [21, 22]. If the heavy quark does not get thermalized, then their contribution may be estimated from pp collision data with the inclusion of nuclear effects like shadowing, and so forth, and they do not contribute to the flow also [24].

(iii) Low mass region (LMR):

$$\left(M \le M_\phi \ (= 1.02 \, \text{GeV})\,, p_T < 1 \, \text{GeV}\right). \tag{3}$$

With subsequent expansion and cooling, the QGP converts into a hot hadron gas at the transition temperature, T_c. At later stages, the dileptons are preferentially radiated from hot hadron gas from the decay of (light) vector meson, such as the ρ, ω, and ϕ. The low M domain of the lepton pairs is dominated by the decays of ρ. Medium modification of ρ will change the yield in this domain of M. The change of ρ spectral function is connected with the chiral symmetry in the bath; therefore, the measurement of low M lepton pairs has great importance to study the chiral symmetry restoration [25, 26] at high temperature and density. Thus the invariant mass of the lepton pair directly reflects the mass distribution of the light vector mesons. This explains the distinguished role that vector mesons in conjunction with their in-medium modifications play for dilepton measurements in HIC.

So far, we have discussed the different sources of photons and dileptons. As QGP is expected to form in the HIC experiments, the basic intention of the present study is to study the properties of QGP. Therefore, we have emphasized more on the study of thermal photons and dileptons in this review, as they may provide information to understand the formation and unique properties of the novel matter.

The emission of thermal photons and dileptons coming from HIC consists of two important segments:

$$\frac{dN}{d^4p} = \int \frac{dR}{d^4p} d^4x, \tag{4}$$

(1) firstly, static emission rate (dR/d^4p) which takes care of the basic interactions in respective phases (QGP or hadronic phase),

(2) Secondly, the space-time integration over four volume (d^4x) which takes care of the evolution of the thermal matter created in HIC. As the EM radiations produced from each space-time point of the evolving matter, we need the concept of relativistic hydrodynamics (described in Section 4) for understanding the evolution.

3. Formulation of Thermal Emission Rate of EM Radiations

The importance of the electromagnetic probes for the study of thermodynamic state of the evolving matter was first proposed by Feinberg in 1976 [27]. Feinberg showed that the emission rates can be related to the electromagnetic current-current correlation function in a thermalized system.

3.1. Dilepton Emission Rate from Thermal Medium. Let us consider an initial state $|I\rangle$ which goes to a final state $|F\rangle$ producing a lepton pair l^+l^- with momenta p_1 and p_2, respectively. The dilepton multiplicity thermally averaged over initial states is given by [4, 28]

$$N = \sum_I \sum_F \left| \left\langle F, l^+l^- \left| e^{i \int \mathscr{L}_{\text{int}} d^4x} \right| I \right\rangle \right|^2$$
$$\times \frac{e^{-\beta E_I}}{Z} \frac{d^3 p_1}{(2\pi)^3 2E_1} \frac{d^3 p_2}{(2\pi)^3 2E_2}, \tag{5}$$

where $\mathscr{L}_{\text{int}} = e\overline{\psi}_l(x)\gamma_\mu \psi_l(x) A^\mu(x) + eJ_\mu(x) A^\mu(x)$ in which $\psi_l(x)$ is the lepton field operator and $J_\mu(x)$ is the electromagnetic current and $Z = \text{Tr}[e^{-\beta H}]$. Following [1, 4, 8] this expression can be put in the form

$$\frac{dN}{d^4q d^4x} = -\frac{\alpha^2}{6\pi^3 q^2} L\left(M^2\right) f_{BE}(q_0) g^{\mu\nu} W_{\mu\nu}(q_0, \vec{q})\,, \tag{6}$$

where the factor $L(M^2) = (1 + 2m_l^2/M^2)(1 - 4m_l^2/M^2)^{1/2}$ is of the order of unity for electrons, $M(= \sqrt{q^2})$ being the invariant mass of the pair, and the electromagnetic (e.m.) current correlator $W_{\mu\nu}$ is defined by

$$W_{\mu\nu}(q_0, \vec{q}) = \int d^4x e^{iq\cdot x} \left\langle \left[J_\mu^{\text{em}}(x), J_\nu^{\text{em}}(0) \right] \right\rangle. \tag{7}$$

Here $J_\mu^{\text{em}}(x)$ is the electromagnetic current and $\langle \rangle$ indicates ensemble average. The rate given by (6) is to leading order in electromagnetic interactions but exact to all orders in the strong coupling encoded in the current correlator $W_{\mu\nu}$. The q^2 in the denominator indicates the exchange of a single virtual photon and the Bose distribution implies the thermal weight of the source. We can also express the dilepton rate in terms of a photon spectral function $A_\gamma^{\mu\nu}$. Using the relation [4],

$$4\pi\alpha W_{\mu\nu} = 2\pi \left(q^2 g_{\mu\alpha} - q_\mu q_\alpha \right) A_\gamma^{\alpha\beta}(-q) \left(q^2 g_{\beta\nu} - q_\beta q_\nu \right) \tag{8}$$

in (6), we have

$$\frac{dN}{d^4q d^4x} = -\frac{\alpha}{(\cdots)} \frac{L^{\mu\nu}}{q^4} f_{BE}(q_0) \, \text{Im}\, \Pi_{\mu\nu}^{\text{em}}(q_0)\,, \tag{9}$$

where $A_{\mu\nu}(q_0, \vec{q}) = \text{Im}\, \Pi_{\mu\nu}^{\text{em}}(q_0)$.

3.2. Photon Emission Rate from Thermal Medium. The photon emission rate is calculated in the similar way to that of dilepton rate. The photon emission rate differs from the dilepton rate in the following way: the factor $e^2 L_{\mu\nu}/q^4$ appearing in the dilepton rate (in (9)) which is nothing but the product of electromagnetic vertex $\gamma^* \rightarrow l^+l^-$, the leptonic current involving Dirac spinors, and the square of the photon propagator should be replaced by the factor $\sum \epsilon^\mu \epsilon^{\nu^*} (= -g^{\mu\nu})$. And the phase space factor $d^3 p_1/(2\pi)^3 E_1 d^3 p_2/(2\pi)^3 E_2$ should be replaced by $d^3 p/(2\pi)^3 E$. Then the photon emission rate becomes

$$q_0 \frac{dR}{d^3q} = \frac{\alpha}{2\pi^3} g^{\mu\nu} f_{BE}(q_0) \, \text{Im}\, \Pi_{\mu\nu}^{\text{em}}. \tag{10}$$

The above emission rate is correct up to order e^2 in electromagnetic interaction but exact, in principle, to all order in strong interaction. However, for all practical purposes, one is able to evaluate up to a finite order of loop expansion. Now it is clear from the above results that to evaluate photon and dilepton emission rate from a thermal system we need to evaluate the imaginary part of the photon self-energy. The Cutkosky rules at finite temperature or the thermal cutting rules [29–32] give a systematic procedure to calculate the imaginary part of a Feynman diagram. The Cutkosky rule expresses the imaginary part of the n-loop amplitude in terms of physical amplitude of lower order ($n - 1$ loop or lower). This is shown schematically in Figure 3. When the imaginary part of the self-energy is calculated up to and including L order loops where L satisfies $x + y < L + 1$, then one obtains the photon emission rate for the reaction x particles $\rightarrow$ y particles $+\gamma$, and the above formalism becomes equivalent to the relativistic kinetic theory formalism [2, 3].

3.3. Emission Rate Using Relativistic Kinetic Theory Formalism.
According to relativistic kinetic theory formulation, the production of i-type particles from the reaction of type $1(p_1) + 2(p_2) \rightarrow 3(p_3) + 4(p)$ is given as follows:

$$
\begin{aligned}
\mathcal{R}_i = \mathcal{N} \int & \frac{d^3 p_1}{(2\pi)^3 2E_1} \frac{d^3 p_2}{(2\pi)^3 2E_2} \frac{d^3 p_3}{(2\pi)^3 2E_3} \frac{d^3 p}{(2\pi)^3 2E} \\
& \times (2\pi)^4 \delta^{(4)} (p_1 + p_2 - p_3 - p) \overline{|\mathcal{M}|^2} \\
& \times f_1 f_2 (1 \pm f_3)(1 \pm f_4),
\end{aligned} \tag{11}
$$

where $\mathcal{N}$ is the overall degeneracy for the reaction under consideration, $\overline{|\mathcal{M}|^2}$ is the square of the invariant amplitude for the process under consideration, p_i, E_i, and $f_i(E_i)$ are the three momentum, energy, and thermal distribution functions (Fermi-Dirac or Bose-Einstein) of the incoming and outgoing particles "i."

The transverse momentum (p_T) distribution of photons from a reaction of the type: $1 + 2 \rightarrow 3 + \gamma$ taking place in a thermal bath at a temperature, T is given by [2, 3]:

$$
\begin{aligned}
E \frac{dR}{d^3 p} = \frac{\mathcal{N}}{2(2\pi)^8} \int & \frac{d^3 p_1}{2E_1} \frac{d^3 p_2}{2E_2} \frac{d^3 p_3}{2E_3} f_1 f_2 (1 \pm f_3) \\
& \times \delta^{(4)} (p_1 + p_2 - p_3 - p) \overline{|\mathcal{M}|^2}.
\end{aligned} \tag{12}
$$

Using the Mandelstam variables (s, t, u) we can write the differential photon production rate as [33]

$$
\begin{aligned}
E \frac{dR}{d^3 p} = \frac{\mathcal{N}}{16(2\pi)^7 E} \int_{(m_1 + m_2)^2}^{\infty} & ds \int_{t_{\min}}^{t_{\max}} dt |\mathcal{M}(s, t, u)|^2 \\
& \times \int dE_1 \int dE_2 \frac{f(E_1) f(E_2) [1 + f(E_3)]}{\sqrt{aE_2^2 + 2bE_2 + c}},
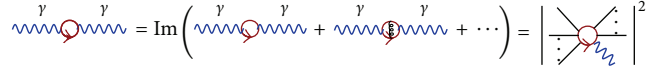\end{aligned} \tag{13}
$$

Figure 3: Optical Theorem in Quantum Field Theory.

where

$$
\begin{aligned}
a &= -\left(s + t - m_2^2 - m_3^2\right)^2, \\
b &= E_1 \left(s + t - m_2^2 - m_3^2\right)\left(m_2^2 - t\right) \\
&\quad + E\left[\left(s + t - m_2^2 - m_3^2\right)\left(s - m_1^2 - m_2^2\right) - 2m_1^2 \left(m_2^2 - t\right)\right], \\
c &= -E_1^2 \left(m_2^2 - t\right)^2 - E^2 \left[\left(s - m_1^2 - m_2^2\right)^2 - 4m_1^2 m_2^2\right] \\
&\quad + m_2^2 \left(s + t - m_2^2 - m_3^2\right)^2 + m_1^2 \left(m_2^2 - t\right)^2 - 2E_1 E \\
&\quad \times \left[2m_2^2 \left(s + t - m_2^2 - m_3^2\right) - \left(m_2^2 - t\right)\left(s - m_1^2 - m_2^2\right)\right] \\
&\quad - \left(s + t - m_2^2 - m_3^2\right)\left(m_2^2 - t\right)\left(s - m_1^2 - m_2^2\right), \\
E_{1\,\min} &= \frac{\left(s + t - m_2^2 - m_3^2\right)}{4E} + \frac{Em_1^2}{s + t - m_2^2 - m_3^2}, \\
E_{2\,\min} &= \frac{Em_2^2}{m_2^2 - t} + \frac{m_2^2 - t}{4E}, \\
E_{2\,\max} &= -\frac{b}{a} + \frac{\sqrt{b^2 - ac}}{a}.
\end{aligned} \tag{14}
$$

In a similar way the dilepton emission rate for a reaction $a\bar{a} \rightarrow l^+ l^-$ can be obtained as

$$
\begin{aligned}
\frac{dR}{d^4 p} = \mathcal{N} \int & \frac{d^3 p_a}{2E_a(2\pi)^3} \frac{d^3 p_{\bar{a}}}{2E_{\bar{a}}(2\pi)^3} \frac{d^3 p_1}{2E_1(2\pi)^3} \frac{d^3 p_2}{2E_2(2\pi)^3} \\
& \times (2\pi)^4 \delta^{(4)} (p_a + p_{\bar{a}} - p_1 - p_2) \delta^{(4)} \\
& \times (p - p_a - p_{\bar{a}}) |\mathcal{M}|_{a\bar{a} \rightarrow l^+ l^-}^2 f(p_a) f(p_{\bar{a}}),
\end{aligned} \tag{15}
$$

where $f(p_a)$ is the appropriate occupation probability for bosons or fermions.

4. Relativistic Hydrodynamics

To evaluate the photon and dilepton production from HIC we need to convolute the static rate over space-time integration. Thus, we need to know hydrodynamics which takes care of the evolution of the matter. In this section, we briefly discuss the relativistic hydrodynamics for an ideal as well as viscous medium formed in HIC. Ideally, one cannot describe heavy ion experimental data from the first principle, that is, quantum chromodynamics (QCD) due to its complexity which mainly arises from nonlinearity of interactions of gluons, strong coupling, dynamical many body system, and color confinement. One promising strategy to connect the first

principle with phenomena is to introduce hydrodynamics as a phenomenological theory. *Relativistic hydrodynamics* [18, 34–43] plays an important role for an expanding system where pressure, temperature, and so forth vary with space and time. It is assumed that, due to intense rescatterings among the produced secondaries, the system reaches a state of local thermal equilibrium and then the evolution of the system is described by relativistic fluid dynamics. To describe the space-time evolution of such expanding system during the collision, the prescription of relativistic hydrodynamics is essential which assumes the system to be in local thermodynamic equilibrium, which means that pressure and temperature are not constant but rather are the function of space and time. This prescription is valid in the regime where the mean-free path in this "thermalised" system λ is much smaller than the characteristic dimensions of the system (L); that is, $L \geq \lambda$.

4.1. Basic Equations of Ideal Hydrodynamics. The space-time evolution of the pressure, energy density, particle densities, and the local fluid velocities is controlled by energy momentum conservation equations from hydrodynamics. The basic equations of relativistic hydrodynamics which result from applying constraints of energy-momentum conservations relevant for heavy ion collision at relativistic energies are expressed in

$$\partial_\mu T^{\mu\nu} = 0, \tag{16}$$

where $T^{\mu\nu}$ is the energy-momentum tensor of fluid element, and in its local rest frame it is given by

$$T_0^{\mu\nu} = \text{diag}\left[\epsilon(x), -P(x), -P(x), -P(x)\right]. \tag{17}$$

Local rest frame is the frame in which the velocity of the fluid element is zero. In such a frame the $T^{\mu\nu}$ becomes diagonal since the energy flux of the fluid T^{i0} and the momentum density T^{0j} turns to be zero. In absence of any dissipative processes the T^{00} component becomes the energy density ϵ and $T^{ij} = P\delta^{ij}$ since $T^{ij}dS_j$ is the ith component of force acting on the surface element which according to Pascal's law is isotropic and perpendicular to the surface. P is the pressure of the fluid element in the local rest frame. Isotropy implies that the energy flux T_{i0} and the momentum density T_{0j} vanish in the rest frame of fluid. In addition, it implies that the pressure tensor is proportional to the identity matrix, that is, $T_{ij} = P\delta_{ij}$, where P is the thermodynamic pressure.

By doing a proper Lorentz transformation, the energy-momentum tensor $T^{\mu\nu}$ in a moving frame, where the fluid moves with an arbitrary four-velocity, $u^\mu = \gamma(1, \vec{v})$ where $\gamma = (1 - v^2)^{-1/2}$, is given in

$$T^{\mu\nu} = \left[\epsilon(x) + P(x)\right] u^\mu u^\nu - P(x) g^{\mu\nu}, \tag{18}$$

where $g^{\mu\nu} \equiv \text{diag}(1, -1, -1, -1)$ is the Mankowski metric tensor and u^μ is the fluid 4-velocity referred to as "collectivity" of the system which can be defined as $u^\mu = \gamma(1, \vec{v})$ with $\gamma = 1/\sqrt{1 - \vec{v}^2}$ and $u^\mu u_\mu = 1$, where $\vec{v}$ is the velocity of fluid element. In the above equation, the ϵ and P are the energy density and pressure, respectively, in the fluid rest frame, and both are functions of space time coordinate x^μ.

Apart from the energy-momentum conservation, a fluid may contain several conserved charges, such as total electric charge, and net baryon number. The conserved charges obey the following continuity equation given in (19):

$$\partial_\mu N_B^\mu = 0. \tag{19}$$

$N_B^\mu = n_B u^\mu$ is the conserved net baryonic current and n_B is baryon number density. For the present work the net baryon number is assumed to be negligible small, so (16) is the only relevant equation to deal with. In addition to it, the total entropy of an inviscid fluid is conserved throughout (S = constant). If we define the entropy current: $s^\mu = su^\mu$, then the conservation of entropy results in $\partial_\mu s^\mu = 0$ [44].

4.2. Basic Equations of Viscous Hydrodynamics. In the above discussion we considered an idealized situation of a perfect fluid with no internal friction or energy dissipation. But in practice most of the times we have to deal with a system of imperfect fluid in which the density, pressure, and fluid velocity changes over a distance of the order of mean-free path. Such presence of a space-time gradient of those thermodynamic quantities results in modifying the energy momentum tensor $T^{\mu\nu}$ and the conserved current N^μ to the first-order gradient of these quantities:

$$T^{\mu\nu} = (\epsilon + P) u^\mu u^\nu - Pg^{\mu\nu} + \Delta T^{\mu\nu},$$
$$N^\mu = nu^\mu + \Delta N^\mu. \tag{20}$$

One thing should be mentioned here that for a relativistic fluid it is necessary to specify whether u^μ is the velocity of energy transport or velocity of particle transport. In the approach of Landau and Lifshitz, u^μ is taken to be the velocity of energy transport and so T^{i0} vanishes in a comoving frame. In the approach of Eckart, u^μ is taken to be the velocity of particle transport and so $N^i = nu^i = 0$ in a comoving frame. The second approach is adopted here to obtain the following assumptions. The modification in the energy momentum tensor $\Delta T^{\mu\nu}$ and conserved current ΔN^μ is such that in a comoving frame:

$$u_\mu u_\nu \Delta T^{\mu\nu} = 0,$$
$$\Delta N^\mu = 0. \tag{21}$$

With these assumptions we need to construct $\Delta T^{\mu\nu}$ to quantify the dissipative processes within the system. This has to be done in such a way that the rate of entropy production per unit volume is positive, which is again required from second law of thermodynamics. To accomplish this task some guidelines are to be followed.

(1) The thermodynamic quantities ϵ, P, and u^μ vary slightly over the mean-free path of the particles within the fluid; that is, the system is only very slightly away from equilibrium. So the dissipative term in energy momentum tensor $\Delta T^{\mu\nu}$ must be a linear combination of space-time derivatives of ϵ, P, u^μ, and so forth.

(2) Only the space time derivative of T and u^μ can occur in $\Delta T^{\mu\nu}$ because if derivative of ϵ, P, or n appeared in $\Delta T^{\mu\nu}$, then $\partial_\mu S^\mu$ would contain pressure or density gradient, with velocity or temperature gradient and these products are not always positive for all fluid configurations.

The entropy production rate comes out to be

$$\frac{\partial S^\mu}{\partial x^\mu} = \left[\frac{1}{T}\dot{u}_i - \frac{1}{T^2}\frac{\partial T}{\partial x^i}\right]\Delta T^{i0} + \frac{1}{T}\left(\partial_j u_i\right)\Delta T^{ij}. \qquad (22)$$

From the condition that $\partial_\mu s^\mu \geq 0$ for all fluid configuration we obtain

$$\Delta T^{ij} = \eta\left(\frac{\partial u^i}{\partial x^j} + \frac{\partial u^j}{\partial x^i} - \frac{2}{3}\vec{\nabla}\cdot\vec{u}\delta^{ij}\right) + \zeta\vec{\nabla}\cdot\vec{u}\delta^{ij},$$

$$\Delta T^{i0} = -\chi\frac{\partial T}{\partial x^i} + \zeta\frac{\partial u^i}{\partial t}, \qquad (23)$$

$$\Delta T^{00} = 0,$$

where η is the coefficient of shear viscosity, ζ is coefficient of bulk viscosity, and χ is thermal conductivity.

Generalizing this expression $\Delta^{\mu\nu}$ comes out to be [45]

$$\Delta T^{\mu\nu} = \eta\left(\nabla^\mu u^\nu + \nabla^\nu u^\mu - \frac{2}{3}\Delta^{\mu\nu}\nabla_\rho u^\rho\right) + \zeta\Delta^{\mu\nu}\nabla_\rho u^\rho. \qquad (24)$$

Here we have ignored the terms related to thermal conductivity since we are not showing any effect of that on any observables. We have defined $\nabla^\mu = \Delta^{\mu\nu}\partial_\nu$, where $\Delta^{\mu\nu} = g^{\mu\nu} - u^\mu u\nu$ is the projection operator.

For the present study, the evaluation of matter from QGP (initial) to the hadronic system (final) via an intermediate quark-hadron transition is studied by applying relativistic hydrodynamics.

4.3. Space-Time Evolution. Hydrodynamics is a general framework to describe the space-time evolution of locally thermalized matter for a given equation of state (EoS). The basic ingredients required to solve the ideal hydrodynamic equations are EoS and initial conditions. As the system expands from its initial state, the mean-free path between particles within the system increases. At certain stage, the mean-free path becomes comparable to the system size, and then the hydrodynamic description breaks down and the phase space distribution of the particle gets fixed by the temperature of the system at this stage. This stage of evolution is called freezeout state and the corresponding temperature of the system is called thermal freezeout temperature (T_f). The hydrodynamic evolution stops at the freezeout point.

4.3.1. Initial Condition. The initial conditions are crucial to the description of space-time evolution. Initial conditions in hydrodynamics may be constrained in the following ways to reproduce the measured final multiplicity. We assume that the system reaches equilibration at a time τ_i (called initial thermalization time) after the collision. The T_i can be

related to the measured hadronic multiplicity (dN/dy) by the following relation [46]:

$$T_i^3 \tau_i \approx \frac{2\pi^4}{45\zeta(3)}\frac{1}{4a_{\text{eff}}}\frac{1}{\pi R_A^2}\frac{dN}{dy}, \qquad (25)$$

where $R_A \sim 1.1 N_{\text{part}}^{1/3}$ is the radius of the system, $\zeta(3)$ is the Riemann zeta function, and $a_{\text{eff}} = \pi^2 g_{\text{eff}}/90$, $g_{\text{eff}}(= 2 \times 8 + (7/8)\times 2 \times 2 \times N_c \times N_F)$ is the degeneracy of quarks and gluons in QGP, N_c = number of colors, N_F = number of flavors. The factor "7/8" originates from the difference between the Bose-Einstein and the Fermi-Dirac statistics. T_i depends on the centrality through the multiplicity, dN/dy. The value of dN/dy for various beam energies and centralities can be obtained directly from experiment or calculated using the following relation [47]:

$$\frac{dN}{dy} = (1 - x)n_{\text{pp}}\frac{\langle N_{\text{part}}\rangle}{2} + xn_{\text{pp}}\langle N_{\text{coll}}\rangle, \qquad (26)$$

where n_{pp} is the multiplicity per unit rapidity measured in pp collisions: $n_{\text{pp}} = 2.5 - 0.25\ln(s) + 0.023\ln^2(s)$, the fraction x of n_{pp} is due to "hard" processes, with the remaining fraction $(1 - x)$ being "soft" processes. The multiplicity in nuclear collision has then two components: "soft," which is proportional to number of participants, N_{part} and "hard," which is proportional to number of binary collision, N_{coll}.

After the initial thermalization time, τ_i, the system can be treated hydrodynamically. The initial conditions to solve the hydrodynamic equations are given through the energy density and velocity profile:

$$\epsilon(\tau_i, r) = \frac{\epsilon_0}{1 + \exp\left((r - R_A)/\delta\right)},$$

$$v(\tau_i, r) = 0, \qquad (27)$$

where ϵ_0 is the initial energy density which is related to initial (T_i), R_A is the nuclear radius, and δ is the diffusion parameter taken as 0.5 fm.

4.3.2. Equation of State (EoS). The set of hydrodynamic equations are not closed by itself; the number of unknown variable exceeds the number of equations by one. Thus a functional relation between any two variables is required so that the system become deterministic. The most natural course is to look for such relation between the pressure P and the energy density ϵ. Under the assumption of local thermal equilibrium, this functional relation between P, ϵ, and n_B is the EoS:

$$P = P(\epsilon, n_B) \qquad (28)$$

which expresses the pressure as function of energy density, ϵ, and baryon density, n_B. This can be obtained by exploiting numerical lattice QCD simulation [48].

Different EoSs (corresponding to QGP vis-a-vis that of hadronic matter) will govern the hydrodynamic flow quite differently. It is thus imperative to understand in what
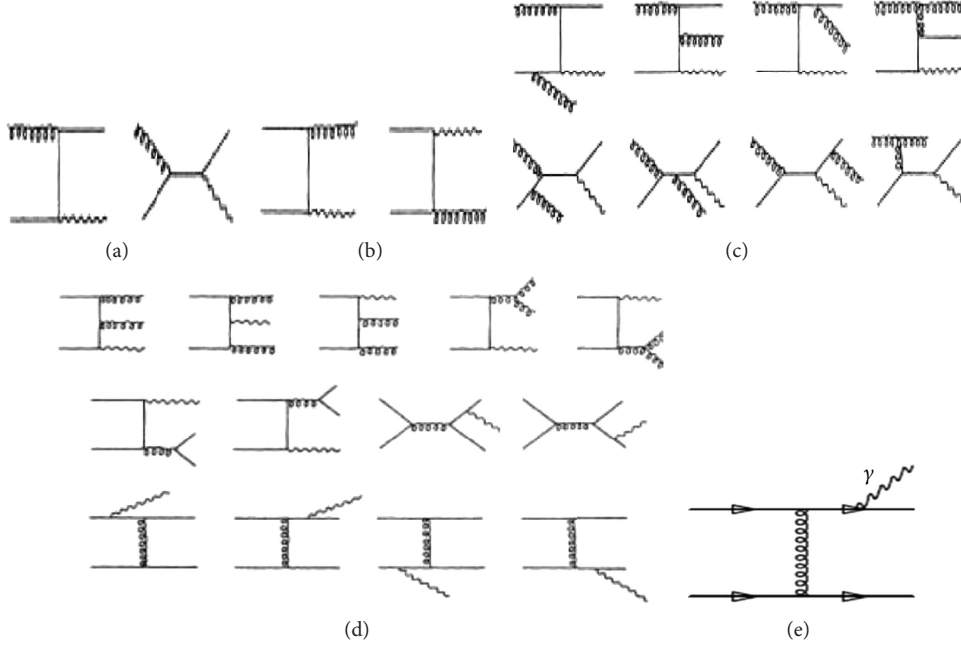
Figure 4: Partonic processes for production of photons.

respects the two EoSs differ and how they affect the evolution in space and time. The role of the EoS in governing the hydrodynamic flow lies in the fact that the velocity of sound, $c_s^2 = (\partial P/\partial \epsilon)$ sets an intrinsic scale in hydrodynamic evolution. One can thus write simple parametric form of the EoS: $P = c_s^2 \epsilon$, for baryon-free system which is relevant for the present study.

4.3.3. Freeze-Out Criteria. The expansion persists as long as the fluid particles interact. At sufficiently longer λ when it is comparable to system size the particles decouple to behave as free particles which is called "freeze-out" stage. This freeze-out scenario is characterized by a system temperature T_f which is of the order of pion mass and defines a space-time surface $T(x,t) = T_f$ which serves as the boundary of the hydrodynamical flow [49].

5. Emission of Thermal Photons from Heavy Ion Collision

The *thermal* photons emerge just after the system thermalizes ($\tau > \tau_i$) from both QGP due to partonic interactions and hot hadrons due to interactions among the hadrons. Now with the formalism discussed in Section 3, the production of thermal photons from QGP and hot hadronic gas is given in Sections 5.1 and 5.2, respectively. And using the hydrodynamic equations, we have convoluted these static rates by space-time integration (discussed in Section 4) and obtained the total invariant yield of photon for different collision energies. The space-time integration is constrained to the hydrodynamical inputs which has been discussed elaborately in this section.

5.1. Photons Emission from Quark Gluon Plasma. The contribution from QGP to the spectrum of thermal photons due to annihilation ($q\bar{q} \rightarrow g\gamma$) and Compton ($q(\bar{q})g \rightarrow q(\bar{q})\gamma$) processes has been calculated in [17, 50] using hard thermal loop (HTL) approximation [51, 52]. The rate of hard photon emission is then obtained as [17]

$$E\frac{dR_\gamma^{\mathrm{QGP}}}{d^3q} = \sum_f e_f \frac{\alpha\alpha_s}{2\pi^2} T^2 e^{-E/T} \ln\left(\frac{2.912E}{g_s^2 T}\right), \quad (29)$$

where α_s is the strong coupling constant. Later, it was shown that photons from the processes [53]: $gq \rightarrow gq\gamma$, $qq \rightarrow qq\gamma$, $q q\bar{q} \rightarrow q\gamma$, and $gq\bar{q} \rightarrow g\gamma$ contribute in the same order $O(\alpha\alpha_s)$ as Compton and annihilation processes (shown in Figure 4). The complete calculation of emission rate from QGP to order α_s has been performed by resuming ladder diagrams in the effective theory [54, 55]. In the present work this rate has been used. The temperature dependence of the strong coupling, α_s, has been taken from [56].

5.2. Photons Emission from Hot Hadronic Gas. For the photon spectra from hadronic phase we consider an exhaustive set of hadronic reactions and the radiative decay of higher resonance states [33, 57, 58].

To evaluate the photon emission rate from a hadronic gas we model the system as consisting of π, ρ, ω, and η. The relevant vertices for the reactions $\pi\pi \rightarrow \rho\gamma$ and $\pi\rho \rightarrow \pi\gamma$ and the decay $\rho \rightarrow \pi\pi\gamma$ are obtained from the following Lagrangian [57] (see Figure 5):

$$\mathcal{L} = -g_{\rho\pi\pi}\vec{\rho}^{\,\mu} \cdot \left(\vec{\pi} \times \partial_\mu \vec{\pi}\right) - eJ^\mu A_\mu + \frac{e}{2} F^{\mu\nu}\left(\vec{\rho}_\mu \times \vec{\rho}_\nu\right)_3, \quad (30)$$
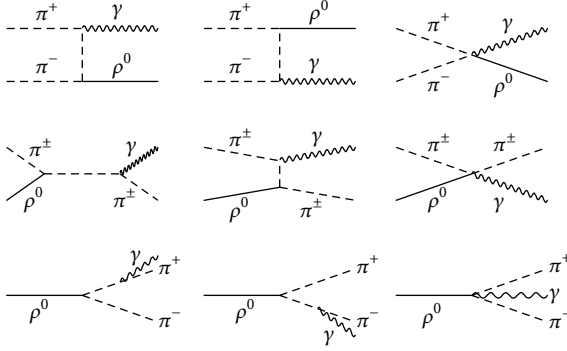
FIGURE 5: Photon-producing reactions and decays in hadronic gas.

where $F_{\mu\nu} = \partial_\mu A_\nu - \partial_\nu A_\mu$ is the Maxwell field tensor and J^μ is the hadronic part of the electromagnetic current given by

$$J^\mu = \left(\vec{\rho}_\nu \times \vec{B}^{\nu\mu}\right)_3 + \left(\vec{\pi} \times \left(\partial^\mu \vec{\pi} + g_{\rho\pi\pi}\vec{\pi} \times \vec{\rho}^\mu\right)\right)_3 \qquad (31)$$

with $\vec{B}_{\mu\nu} = \partial_\mu \vec{\rho}_\nu - \partial_\nu \vec{\rho}_\mu - g_{\rho\pi\pi}(\vec{\rho}_\mu \times \vec{\rho}_\nu)$.

For the sake of completeness we have also considered the photon production due to the reactions $\pi\eta \rightarrow \pi\gamma$, $\pi\pi \rightarrow \eta\gamma$, and the decay $\omega \rightarrow \pi\gamma$ using the following interaction:

$$\mathscr{L} = \frac{g_{\rho\rho\eta}}{m_\eta}\epsilon_{\mu\nu\alpha\beta}\partial^\mu\rho^\nu\partial^\alpha\rho^\beta\eta$$
$$+ \frac{g_{\omega\rho\pi}}{m_\pi}\epsilon_{\mu\nu\alpha\beta}\partial^\mu\omega^\nu\partial^\alpha\rho^\beta\pi + \frac{em_\rho^2}{g_{\rho\pi\pi}}A_\mu\rho^\mu. \qquad (32)$$

The last term in the above Lagrangian is written down on the basis of vector meson dominance (VMD) [60, 61]. To evaluate the photon spectra, we have taken the relevant amplitudes for the abovementioned interactions from [33, 57]. The effects of hadronic form factors [62] have also been incorporated in the present calculation. The reactions involving strange mesons: $\pi K^* \rightarrow K\gamma$, $\pi K \rightarrow K^*\gamma$, $\rho K \rightarrow K\gamma$, and $KK^* \rightarrow \pi\gamma$ [62, 63] have also been incorporated in the present work. Contributions from other decays, such as $K^*(892) \rightarrow K\gamma$, $\phi \rightarrow \eta\gamma$, $b_1(1235) \rightarrow \pi\gamma$, $a_2(1320) \rightarrow \pi\gamma$, and $K_1(1270) \rightarrow \pi\gamma$, have been found to be small [63] for $p_T > 1$ GeV.

With all photon-producing hadronic reaction, the static thermal emission rate of photons for hadronic phase has been evaluated [17, 33, 54, 55, 57, 62]. The reaction involving ρ mesons has dominant contribution. The rate at low photon energy is dominated by reaction with ρ in final state, because these reactions are endothermic with most of the available energy going into rho mass. At high photon energy reactions with the ρ in initial state are dominant because these reactions are exothermic; most of the rho mass is available for the production of high energy photons. Similar remarks can be made concerning reactions involving η mesons, but as the value of $g_{\rho\rho\eta}$ is smaller, thus so are the rates. All the isospin combinations for the above processes have properly been implemented.

5.3. Total Invariant Momentum Spectra of Thermal Photons.
In this section we evaluate photon spectrum from a dynamically evolving system. The evolution of the system is governed by relativistic hydrodynamic. The photon production from an expanding system can be calculated by convoluting the static thermal emission rate with the expansion dynamics, which can be expressed as follows:

$$\frac{dN_\gamma}{d^2p_T dy} = \sum_i \int_i \left[\frac{dR_\gamma}{d^2p_T dy}\left(E^*, T\right)\right]_i d^4x, \qquad (33)$$

where the d^4x is the four volume. The energy, E^*, appearing in (33) should be replaced by $u^\mu p_\mu$ for a system expanding with space-time-dependent four-velocity u^μ. Under the assumption of cylindrical symmetry and longitudinal boost invariance, u^μ can be written as

$$u = \gamma_T(\tau, r)\left(\frac{t}{\tau}, v_r(\tau, r), \frac{z}{\tau}\right)$$
$$= \gamma_T\left(M_T \cosh\eta, u_x, u_y, M_T \sinh\eta\right) \qquad (34)$$
$$= \gamma_T\left(M_T \cosh\eta, v_r \cos\phi, v_r \sin\phi, M_T \sinh\eta\right),$$

where $v_r(\tau, r)$ is the radial velocity, $\gamma_r(\tau, r) = (1 - v_r(\tau, r))^{-1/2}$ and, therefore, for the present calculations,

$$u^\mu p_\mu = \gamma_r\left(M_T \cosh(y - \eta) - v_r p_T \cos\phi\right). \qquad (35)$$

For massless photon the factor $u^\mu p_\mu$ can be obtained by replacing M_T in (35) by p_T. For the system produced in QGP phase reverts to hot hadronic gas at a temperature $T \sim T_c$. Thermal equilibrium may be maintained in the hadronic phase until the mean-free path remains comparable to the system size. The term "$(dR/d^2 p_T dy)_i = [(\cdots)f_{BE}]$" is the static rate of photon production where i stands for quark matter (QM), mixed phase (M) (in a 1st-order phase transition scenario), and hadronic matter (HM), respectively. The p_T dependence of the photon and dilepton spectra originating from an expanding system is predominantly determined by the thermal factor f_{BE}. The total momentum distribution can be obtained by summing the contribution from QM and HM, where the distribution for both the phases can be obtained by choosing the phase space appropriately.

The d^4x integration has been performed by using relativistic hydrodynamics with longitudinal boost invariance [41] and cylindrical symmetry [64] along with the inputs (given in Table 1) as the initial conditions for SPS and RHIC energies.

To estimate dN/dy for RHIC, we have taken $dn_{pp}/dy = 2.43$ and $x = 0.1$ at $\sqrt{s_{NN}} = 200$ GeV. It should be mentioned here that the values of dN/dy (through N_{part} and N_{coll} in (26)) and hence the T_i (through dN/dy in (25)) depend on the centrality of the collisions. For SPS, dN/dy is taken from experimental data [65]. We use the EoS obtained from the lattice QCD calculations by the MILC collaboration [66]. We consider kinetic freeze-out temperature, $T_f = 140$ MeV for all the hadrons. The ratios of various hadrons measured experimentally at different $\sqrt{s_{NN}}$ indicate that the system formed in heavy ion collisions chemically decouple at T_{ch}

TABLE 1: The values of various parameters—thermalization time (τ_i), initial temperature (T_i), and hadronic multiplicity dN/dy (the value of dN/dy for various beam energies and centralities is calculated from (26))—used in the present calculations.

$\sqrt{s_{NN}}$	Centrality	dN/dy	τ_i (fm)	T_i (MeV)
17.3 GeV	0–06%	700	1.0	200
	0–20%	496	0.6	227
200 GeV	20–40%	226	0.6	203
	min. bias	184	0.6	200
2.76 TeV	0–40%	1212	0.1	553

which is higher than T_f which can be determined by the transverse spectra of hadrons [67, 68]. Therefore, the system remains out of chemical equilibrium from T_{ch} to T_f. The deviation of the system from the chemical equilibrium is taken into account by introducing chemical potential for each hadronic species. The chemical nonequilibration affects the yields through the phase space factors of the hadrons which in turn affects the productions of the EM probes. The value of the chemical potential has been taken into account following [69].

5.4. Results and Discussion on p_T Distributions of Photons. For comparison with direct photon spectra as extracted from HIC two further ingredients are required. With all the ingredients we have reproduced the p_T spectra of direct photon for both SPS and RHIC energies. The prompt photons are normally estimated by using perturbative QCD. However, to minimize the theoretical model dependence here, we use the available experimental data from p-p collisions to estimate the hard photon and normalized it to A-A data with $T_{AA}(b)$ for different centrality; that is, the photon production from A-A collision and p-p collision are related to the following relation:

$$\frac{dN^{AA}}{d^2 p_T dy} = \frac{N_{coll}(b)}{\sigma_{in}^{pp}} \frac{d\sigma^{NN}}{d^2 p_T dy} = T_{AA}(b) \frac{d\sigma^{NN}}{d^2 p_T dy}, \quad (36)$$

where $N_{coll}(b)$ is taken for the corresponding experiments and the the typical σ_{in}^{pp} (σ_{in}^{pp} 41 mb for RHIC and 30 mb for SPS).

5.4.1. Photon Spectrum for WA98 Collaboration. The WA98 photon spectra from Pb+Pb collisions are measured at $\sqrt{s_{NN}}$ = 17.3 GeV. However, no data at this collision energy is available for pp interactions. Therefore, prompt photons for p+p collision at $\sqrt{s_{NN}}$ = 19.4 GeV have been used [70] to estimate the hard contributions for nuclear collisions at $\sqrt{s_{NN}}$ = 17.3 GeV. Appropriate scaling [65] has been used to obtain the results at $\sqrt{s_{NN}}$ = 17.3 GeV. For the Pb+Pb collisions the result has been appropriately scaled by the number of collisions at this energy (this is shown in Figure 6 as prompt photons). The high p_T part of the WA98 data is reproduced by the prompt contributions reasonably well. At low p_T the hard contributions underestimate the data indicating the presence of a thermal source. The thermal photons with initial temperature = 200 MeV along with the
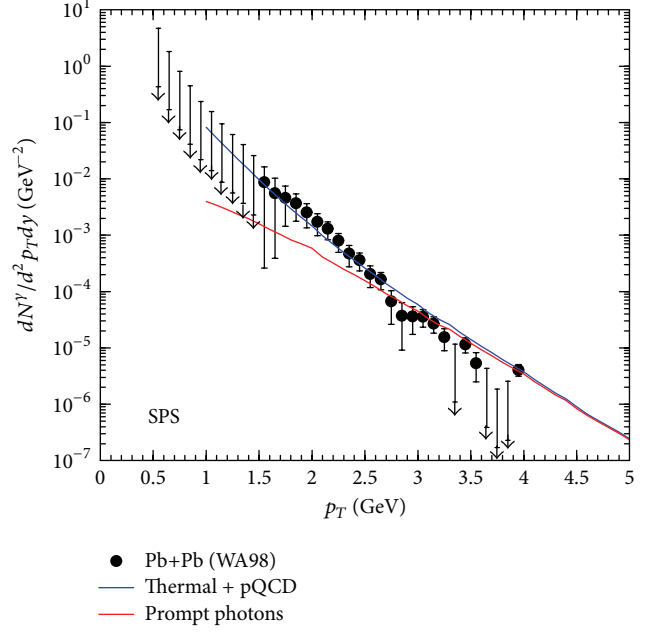

FIGURE 6: Transverse momentum spectra of photon at SPS energy for Pb+Pb collision at midrapidity [12].

prompt contributions explain the WA98 data well (Figure 6), with the inclusion of nonzero chemical potentials for all hadronic species considered [25, 26, 69, 71, 72]. In some of the previous works [73–78] the effect of chemical freezeout is ignored. As a result either a higher value of T_i or a substantial reduction of hadronic masses in the medium was required [73]. In the present work, the data has been reproduced without any such effects.

5.4.2. Photon Spectrum for PHENIX Collaboration. In Figure 7, transverse momentum spectra of photons at RHIC energy for Au-Au collision for three different centralities (0–20%, 20–40%, and min. bias.) at midrapidityi shown, where the red tangles are the direct photon data measured by PHENIX collaboration [79] from Au-Au collision at $\sqrt{s_{NN}}$ = 200 GeV, blue-dashed line is the contribution of the prompt photons and the black solid line is thermal + prompt photons. For the prompt photon contribution at $\sqrt{s_{NN}}$ = 200 GeV, we have used the available experimental data from pp collision and normalized it to Au-Au data with $T_{AA}(b)$ for different centrality [80] (using (36)). At low p_T the prompt photons underestimate the data indicating the presence of a possible thermal source. The thermal photons along with the prompt contributions explain the data [79] from Au-Au collisions at $\sqrt{s_{NN}}$ = 200 GeV reasonably well. The reproduction of data is satisfactory (Figure 7) for all the centralities with the initial temperature shown in Table 1 [81].

5.4.3. Photon Spectrum for ALICE Collaboration. The direct photon spectra from Pb+Pb collisions are measured at $\sqrt{s_{NN}}$ = 2.76 TeV for 0–40% centrality by ALICE collaboration. However, no data at this collision energy is available
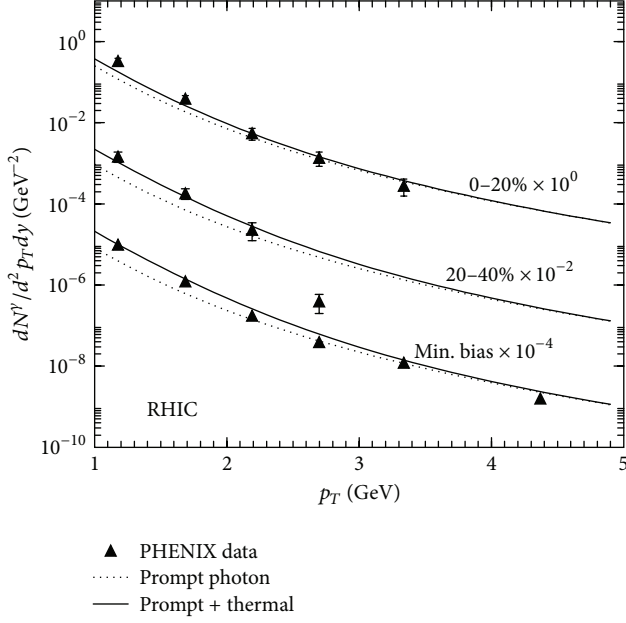
Figure 7: Transverse momentum spectra of photons at RHIC energy for Au-Au collision for different centralities at midrapidity [12].

▲ PHENIX data
⋯⋯ Prompt photon
—— Prompt + thermal

Figure 8: Transverse momentum spectra of photons at LHC energy for Pb-Pb collision for different 0–40% centrality at midrapidity [59].

—— Thermal + prompt photon
– – – Prompt photon from pp data
⋯⋯ Thermal photon

for pp interactions. Therefore, prompt photons from p+p collision at $\sqrt{s_{NN}} = 7$ TeV have been used to estimate the hard contributions for nuclear collisions at $\sqrt{s_{NN}} = 2.76$ TeV by using the scaling (with $\sqrt{s_{NN}}$) procedure used in [65]. For the Pb+Pb collisions the result has been scaled up by the number of collisions at this energy (this is shown in Figure 8 as prompt photons). The high p_T part of the data is reproduced by the prompt contributions reasonably well. At low p_T the hard contributions underestimate the data indicating the presence of a possible thermal source.

The thermal photons with initial temperature ~553 MeV along with the prompt contributions explain the data well (Figure 8), with the inclusion of nonzero chemical potentials for all hadronic species considered [69] (see also [71, 72]).

It is well known that transverse momentum spectra of photons act as a thermometer of the interior of the plasma. The inverse slope of the thermal distribution is a measure of the average (over evolution) effective (containing flow) temperature of the system. We have extracted the average effective temperature ($\sim \langle p_T \rangle$) from the thermal distributions of photons at different collision energies—that is, for SPS, RHIC, and LHC energies. Figure 9 shows the variation of $\langle p_T \rangle$ with multiplicity for different collision energies. To minimize the centrality dependence of the results the $dN_{ch}/d\eta$ is normalized by N_{part}. The results clearly indicate a significant rise in the average p_T ($\langle p_T \rangle$) while going from SPS to RHIC to LHC. The values of $\langle p_T \rangle$ for different collision energies are given in Table 1. Since photons are emitted from each space time point of the system, therefore, the measured slope of the p_T spectra represents the average effective temperature of the system.

The quantity, $\rho_{eff}^{av}(= 1/N_{part} dN_{ch}/d\eta)$, is proportional to the entropy density. Therefore, $\rho_{eff}^{av}/\langle p_T \rangle^3 \propto g_{eff}^{av}$, the average
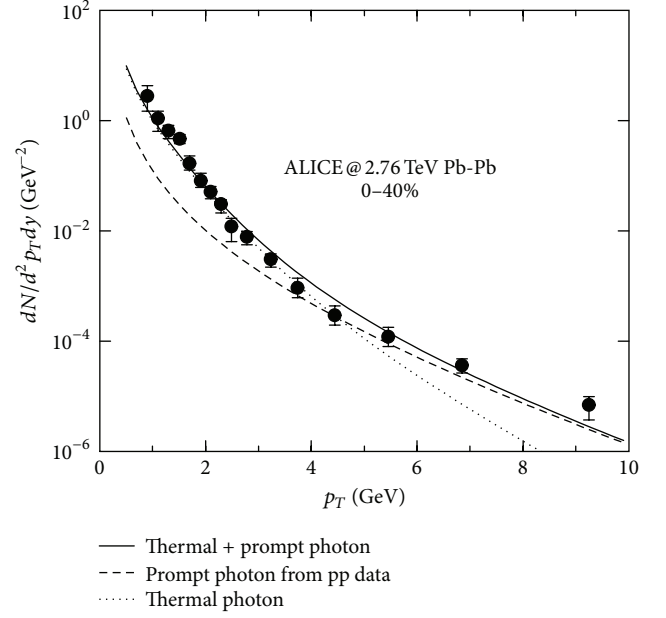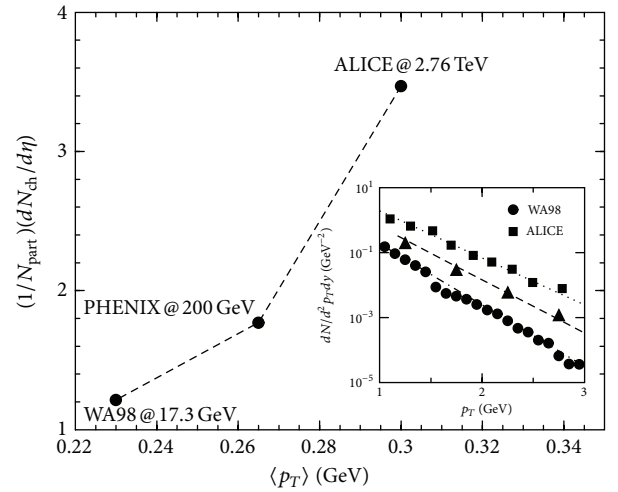

Figure 9: The variation of $\langle p_T \rangle$ with the increase in multiplicity for different collision energies.

effective statistical degeneracy, a quantity which changes drastically if the colour degrees of freedoms deconfined; that is, if a phase transition takes place in the system. We find that the entropy density ($s \sim g_{eff} T^3$) at LHC increases by almost 96% compared to RHIC, and there is an enhancement of 46% at RHIC compared to SPS. However, part of this increase is due to the increase in the temperature and part is due to increase in degeneracy. To estimate the increase in the degeneracy we normalize the quantity ρ_{eff}^{av} by $\langle p_T \rangle^3$. Therefore, we estimate $\rho_{eff}^{av}/\langle p_T \rangle^3$ from the analysis of the experimental data and found that there is a 15% increase in this quantity from SPS to RHIC and 35% increase from RHIC to LHC.

5.5. Total Invariant Momentum Spectra of Thermal Photons in Viscous Medium. Effects of viscosity on the transverse momentum distribution of photons were earlier considered in [82, 83] and recently the interest in this field is renewed [84–86]. The measured photon spectra ($dN/d^2 p_T dy$) are the yield obtained after performing the space time integration over the entire evolution history—from the initial state to the freezeout point using (33). Beyond a certain threshold in collision energy the system is expected to be formed in QGP phase which will inevitably make a transition to the hadronic matter later. The measured spectra contain contributions from both QGP and hadronic phases. Therefore, it becomes imperative to estimate the photon emission with viscous effects from QGP as well as hadrons and identify a kinematic window where photons from QGP dominate. While in some of the earlier works [84–86] contributions from hadrons were ignored, in others [82, 83] the effects of dissipation on the phase space factors were omitted. In the present work we study the effects of viscosity on the thermal photon spectra originating from QGP and hadronic matter and argue that photons can be used as a very useful tool to estimate η/s and hence characterize the matter.

Equation (12) can be simplified to the following form (see the appendix) [87]:

$$
\begin{aligned}
\frac{dR}{d^2 p_T dy} = \frac{\mathcal{N}}{16(2\pi)^8} &\int p_{1T} dp_{1T} dp_{2T} d\phi_1 dy_1 dy_2 \\
&\times f_1(p_1) f_2(p_2)(1 \pm f_3(p_3)) \times \overline{|\mathcal{M}|^2} \\
&\times |p_{1T}\sin(\phi_1 - \phi_2) + p_T \sin\phi_2|_{\phi_2 = \phi_2^0}^{-1}.
\end{aligned}
\tag{37}
$$

The effects of viscosity on the photon spectra resulting from HIC enter through two main factors: (i) the modification of the phase space factor due to the deviation of the system from equilibrium and (ii) the space time evolution of the matter governed by dissipative hydrodynamics. One more important issue deserves to be mentioned here. Normally, the initial temperature (T_i) and the thermalization time (τ_i) are constrained by the measured hadron multiplicity (dN/dy). This approach is valid for a system where there is no viscous loss and the time reversal symmetry is valid. However, for a viscous system the entropy at the freezeout point (which is proportional to the multiplicity) contains the initially produced entropy as well as the entropy produced during the space time evolution due to nonzero shear and bulk viscosity. Therefore, the amount of entropy generated during the evolution has to be subtracted from the total entropy at the freezeout point, and the remaining part which is produced initially should be used to estimate the initial temperature. Therefore, for a given dN/dy (which is associated with the freezeout point) and τ_i the magnitude of T_i will be lower in case of viscous dynamics compared to ideal flow.

5.5.1. Viscous Correction to the Distribution Function. We assume that the system is slightly away from equilibrium which relaxes back to equilibrium through dissipative processes. Here we briefly recall the main considerations leading to the commonly used form for the first viscous correction, δf, to the phase space factor, f, defined as follows [88]:

$$
\begin{aligned}
f_i(p) &= f_{i0}(1 + \delta f_i) \\
&= f_{i0}\left(1 + \frac{p^\alpha p^\beta}{2T^3}\left[C\langle\nabla_\alpha u_\beta\rangle + A\Delta_{\alpha\beta}\nabla \cdot u\right]\right),
\end{aligned}
\tag{38}
$$

where f_{i0} is the equilibrium distribution function of "ith" particle, $\langle\nabla_\alpha u_\beta\rangle \equiv \nabla_\alpha u_\beta + \nabla_\beta u_\alpha - (2/3)\Delta_{\alpha\beta}\nabla_\gamma u^\gamma$, $\Delta_{\alpha\beta} = g_{\alpha\beta} - u_\alpha u_\beta$, $\nabla_\alpha = (g_{\alpha\beta} - u_\alpha u_\beta)\partial^\beta$, u_μ being the four-velocity of the fluid. The coefficients C and A can be determined in the following way. Substituting f in the expression for stress-energy tensor $T^{\mu\nu}$ we get

$$
\begin{aligned}
T^{\mu\nu} &= \int \frac{d^3 p}{(2\pi)^3 E} p^\mu p^\nu f_0 (1 + \delta f) \\
&= T_0^{\mu\nu} + \Delta T^{\mu\nu},
\end{aligned}
\tag{39}
$$

where $T_0^{\mu\nu} = (\epsilon + P)u^\mu u^\nu - g^{\mu\nu}P$ is the energy momentum tensor for ideal fluid. From general considerations [44] the dissipative part can be written as

$$
\Delta T^{\mu\nu} = \eta\langle\nabla^\mu u^\nu\rangle + \zeta\Delta^{\mu\nu}\nabla \cdot u.
\tag{40}
$$

Equating the part containing δf from (38) with (40), C and A can be expressed in terms of the coefficients of shear (η) and bulk (ζ) viscosity, respectively, in terms of which the phase space distribution for the system can be written as

$$
f = f_0\left(1 + \frac{\eta/s}{2T^3}p^\alpha p^\beta\langle\nabla_\alpha u_\beta\rangle - \frac{\zeta/s}{5T^3}p^\alpha p^\beta\Delta_{\alpha\beta}\nabla \cdot u\right).
\tag{41}
$$

For a boost invariant expansion in $(1+1)$ dimension this can be simplified to get

$$
f = f_0\left[1 + \delta f_\eta - \delta f_\zeta\right],
\tag{42}
$$

where

$$
\begin{aligned}
\delta f_\eta &= \frac{\eta/s}{3T^3\tau}\left(p_T^2 - 2{p_z'}^2\right), \\
\delta f_\zeta &= \frac{\zeta/s}{5T^3\tau}\left(p_T^2 + {p_z'}^2\right),
\end{aligned}
\tag{43}
$$

where $p_z' = m_T \sinh(y - \eta)$ is the z-component of the momentum in the fluid comoving frame. The phase space distribution with viscous correction (42) thus enters the production rate of photon through (37).

5.5.2. Viscous Correction to the Expansion Dynamics. As mentioned before the p_T distribution of thermal photons is obtained by integrating the emission rate over the evolution history of the expanding fluid. Relativistic viscous hydrodynamics can be used as a tool for the space-time dynamics of the fluid.

For a $(1 + 1)$ dimensional boost invariant expansion [41] the evolution equation, $\partial_\mu T^{\mu\nu} = 0$, can be written as [89]

$$\frac{d\epsilon}{d\tau} + \frac{\epsilon + P}{\tau} = \frac{(4/3)\eta + \zeta}{\tau^2}, \tag{44}$$

where P is the pressure and ϵ is the energy density. We assume that the baryonic chemical potential is small in the central rapidity region for RHIC/LHC collision energies. Therefore, the equation corresponding to the net baryon number conservation need not be considered in these situations.

We assume that the system achieves thermal equilibrium at a time τ_i after the collision at an initial temperature T_i. With this initial condition and equation of state (EoS) $P = \epsilon/3$ the solution of (44) can be written as [82]

$$T = T_i\left(\frac{\tau_i}{\tau}\right)^{1/3} + \frac{A_Q}{8a_Q\tau_i}\left[\left(\frac{\tau_i}{\tau}\right)^{1/3} - \frac{\tau_i}{\tau}\right], \tag{45}$$

where $A_Q = ((4/3)\eta_{Q0} + \zeta_{Q0})$, $\eta_{Q0} = \eta_Q/T^3 = 4a_Q(\eta/s)_Q$, and $\zeta_{Q0} = \zeta_Q/T^3 = 4a_Q(\zeta/s)_Q$.

Equation (45) dictates the cooling of the QGP phase from its initial state to the transition temperature, T_c, at a time, τ_q, when the QGP phase ends.

In a first-order phase transition scenario, the pure QGP phase is followed by a coexistence phase of QGP and hadrons. The energy density, shear, and bulk viscosities in the mixed phase can be written in terms of the corresponding quantities of the quark and hadronic phases at temperature T_c as follows [82]:

$$\epsilon_M(\tau) = f_Q\epsilon_Q(T_c) + (1 - f_Q(\tau))\epsilon_H(T_c),$$

$$\eta_M(\tau) = f_Q\eta_Q(T_c) + (1 - f_Q(\tau))\eta_H(T_c), \tag{46}$$

$$\zeta_M(\tau) = f_Q\zeta_Q(T_c) + (1 - f_Q(\tau))\zeta_H(T_c),$$

where $f_Q(\tau)(f_H(\tau))$ indicates the fraction of the quark (hadronic) matter in the mixed phase at a proper time τ. We have $\epsilon_Q(T_c) = 3a_QT_c^4 + B$, $\epsilon_H(T_c) = 3a_HT_c^4$, $a_Q = g_Q\pi^2/90$, $a_H = g_H\pi^2/90$, B is the bag constant, g_Q (g_H) denote statistical degeneracy for the QGP (hadronic) phase. In the mixed phase the temperature remains constant but the energy density varies with time as the conversion of QGP to hadrons continues. This time variation is executed through $f_Q(\tau)$. Substituting (46) in (44) and solving for $f_Q(\tau)$ we get [82]

$$f_Q = \frac{e^{-b/\tau}}{\tau}\int_{\tau_Q}^{\tau'}\left[\frac{ce^{b/\tau'}}{\tau'} - ae^{b/\tau'}\right]d\tau' + \frac{\tau_Q}{\tau}e^{(b/\tau_Q - b/\tau)}, \tag{47}$$

where $a = 4\epsilon_H/(3\Delta\epsilon)$, $b = [4(\eta_Q - \eta_H)/3 + 2(\zeta_Q - \zeta_H)]/\Delta\epsilon$, $c = ((4/3)\eta_H + 2\zeta_H)/\Delta\epsilon$, and $\Delta\epsilon = \epsilon_Q - \epsilon_H$. Equation (47) indicates how the fraction of QGP in the coexistence phase evolves with time.

The variation of T with τ in the hadronic phase can be obtained by solving (44) with the boundary condition $T = T_c$ and $\tau = \tau_H$, where τ_H is the (proper) time at which the mixed

TABLE 2: The values of various η/s and parameters—initial temperature (T_i), starting time of mixed phase (τ_q), and ending time of mixed phase (τ_h)—used in the present calculations.

η/s	T_i (MeV)	τ_q (fm)	τ_h (fm)
0	328	3.95	8.8
$1/4\pi$	315	3.93	8.78
$2/4\pi$	302	3.92	8.76

phase ends; that is, when the conversion of QGP to hadronic matter is completed,

$$T = T_c\left(\frac{\tau_H}{\tau}\right)^{1/3} + \frac{A_H}{8a_H\tau_H}\left[\left(\frac{\tau_H}{\tau}\right)^{1/3} - \frac{\tau_H}{\tau}\right]. \tag{48}$$

Similar to QGP, $P = \epsilon/3$ has been used for hadronic phase. For a vanishing bulk viscosity ($\zeta = 0$) the cooling of the QGP is dictated by

$$T = T_i\left(\frac{\tau_i}{\tau}\right)^{1/3} + \frac{2}{3\tau_i}\left(\frac{\eta}{s}\right)_Q\left[\left(\frac{\tau_i}{\tau}\right)^{1/3} - \frac{\tau_i}{\tau}\right]. \tag{49}$$

Similarly the time variation of temperature in the hadronic phase is given by

$$T = T_c\left(\frac{\tau_H}{\tau}\right)^{1/3} + \frac{2}{3\tau_H}\left(\frac{\eta}{s}\right)_H\left[\left(\frac{\tau_H}{\tau}\right)^{1/3} - \frac{\tau_H}{\tau}\right]. \tag{50}$$

In a realistic scenario the value of η/s may be different for QGP [90–94] and hadronic phases [95–98]. However, in the present work we take the same value of η/s both for QGP and hadronic matter as shown in Table 2.

5.5.3. Results and Discussion on Viscous Effect on p_T Distributions of Photons. In case of an ideal fluid, the conservation of entropy implies that the rapidity density dN/dy is a constant of motion for the isoentropic expansion [41]. In such circumstances, the experimentally observed (final) multiplicity, dN/dy, may be related to a combination of the initial temperature T_i and the initial time τ_i as $T_i^3\tau_i$. Assuming an appropriate value of τ_i (taken to be ~0.6 fm/c in the present case), one can estimate T_i.

For dissipative systems, such an estimate is obviously inapplicable. Generation of entropy during the evolution invalidates the role of dN/dy as a constant of motion. Moreover, the irreversibility arising out of dissipative effects implies that estimation of the initial temperature from the final rapidity density is no longer a trivial task. We can, nevertheless, relate the experimental dN/dy to the freezeout temperature, T_f, and the freezeout time, τ_f, by the relation:

$$\frac{dN}{dy} = \frac{\pi R_A^2 4a_H T_f^3\tau_f}{\kappa}, \tag{51}$$

where R_A is the radius of the colliding nuclei (we consider AA collision for simplicity) and κ is a constant ~3.6 for massless bosons.

To estimate the initial temperature for the dissipative fluid we follow the following algorithm. We treat T_i as a parameter;

for each T_i, we let the system evolve forward in time under the condition of dissipative fluid dynamics (44) till a given freezeout temperature T_f is reached. Thus τ_f is determined. We then compute dN/dy at this instant of time from (51) and compare it with the experimental dN/dy. The value of T_i for which the calculated dN/dy matches the experimental number is taken to be the value of the initial temperature. Once T_i is determined, the evolution of the system from the initial to the freezeout stage is determined by (45), (47), and (48).

In Figure 10 we display the variation of temperature with proper time. It is clear from the results shown in the inset (Figure 10) that initial temperature for system which evolves with nonzero viscous effects is lower compared to the ideal case for a fixed dN/dy. Because of a nonviscous isentropic evolution scenario the multiplicity (measured at the freezeout point) is fixed by the initial entropy. However, for a viscous evolution scenario the generation of entropy due to dissipative effects contributes to the multiplicity. Therefore, for a given multiplicity (which is proportional to the entropy) at the freezeout point one requires lower initial entropy; hence, initial temperature will be lower. It is also seen (Figure 10) that the cooling of the system is slower for viscous dynamics because of the extra heat generated during the evolution.

In this section we present the shift in the p_T distribution of the photons due to viscous effects. The integrand in (33) is a Lorentz scalar; consequently the Lorenz transformation of the integrand from the laboratory to the comoving frame of the fluid can be effected by just transforming the argument; that is, the energy of the photon ($E = p_T \cosh(y)$) in the laboratory frame should be replaced by $u_\mu p^\mu$ in the comoving frame of the fluid, where p^μ is the four momenta of the photon.

The results presented here are obtained with vanishing bulk viscosity. The effects of viscosity enter into the photon spectra through the phase space factor as well as through the space time evolution. We would like to examine these two effects separately. For convenience we define two scenarios:

(i) the effects of viscosity on the phase space factor are included ($\delta f_\eta \neq 0$) in (42), but the viscous effects on the evolution are neglected ($\eta = 0$) in (44),

(ii) the effects of $\eta \neq 0$ are taken into account in the phase space factors as well as in the evolution dynamics.

The space time-integrated photon yield originating from the QGP in scenario (i) is displayed in Figure 11. Note that the value of the initial temperatures for the results displayed in Figure 11 is the same (for all η/s) because the viscous effects on the evolution are ignored in scenario (i). The viscous effects on the p_T distribution of the photons are distinctly visible. The higher values of η/s make the spectra flatter through the p_T dependence of the correction, δf_η.

Next we assess the effects of viscosity on photon spectra for scenario (ii). In Figure 12 we depict the photon spectra for various values of η/s. In this scenario the value of T_i is lower for higher η/s for reasons described above. As a result the enhancement in the photon production due to change
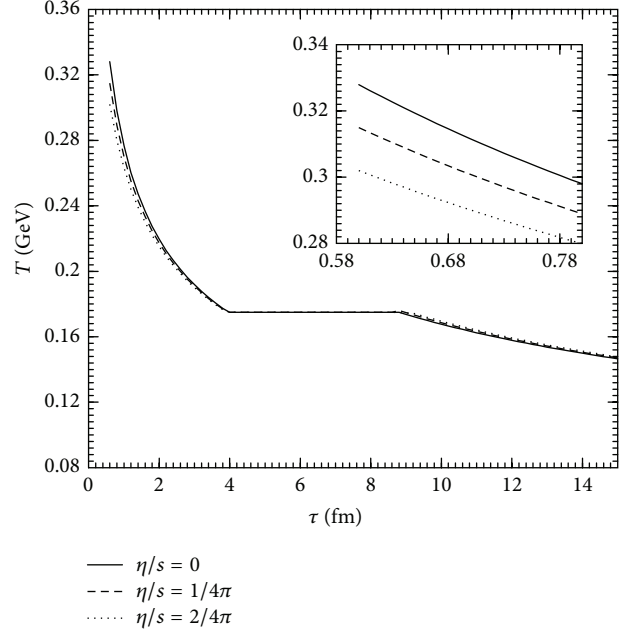

FIGURE 10: Variation of temperature with proper time for different phases for various values of the shear viscosities. Inset shows the effect of viscosity on the cooling of the QGP phase (in an amplified scale) for different values of η/s.
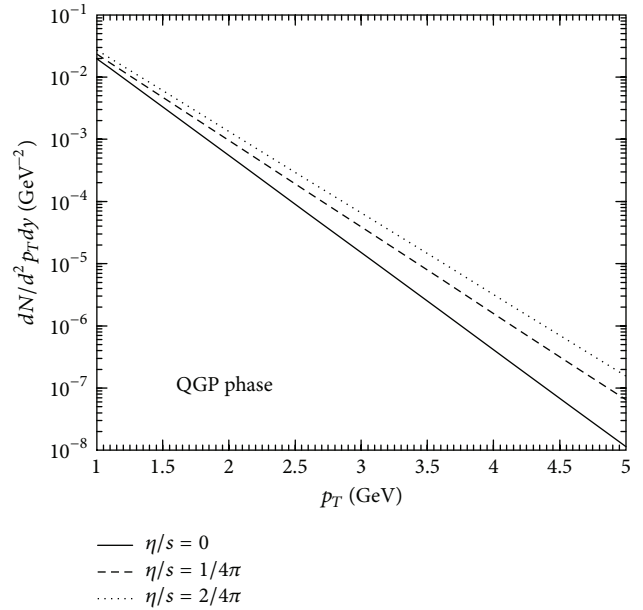

FIGURE 11: Transverse momentum distribution of thermal photons from QGP for various values of η/s in the scenario (i).

in phase space factor, δf_η, is partially compensated by the reduction in T_i for nonzero η, which is clearly seen in the results displayed in Figures 11 and 12.

In Figures 13 and 14 we exhibit results for the hadronic phase for scenarios (i) and (ii), respectively. The effects of dissipation on the p_T distribution of photons from hadronic phase are qualitatively similar to the QGP phase; that is,
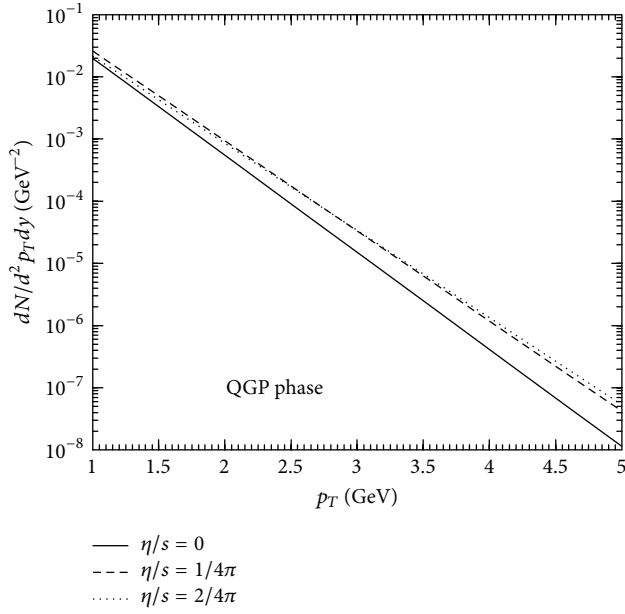
FIGURE 12: Transverse momentum distribution of thermal photons from QGP for various values of η/s in the scenario (ii).
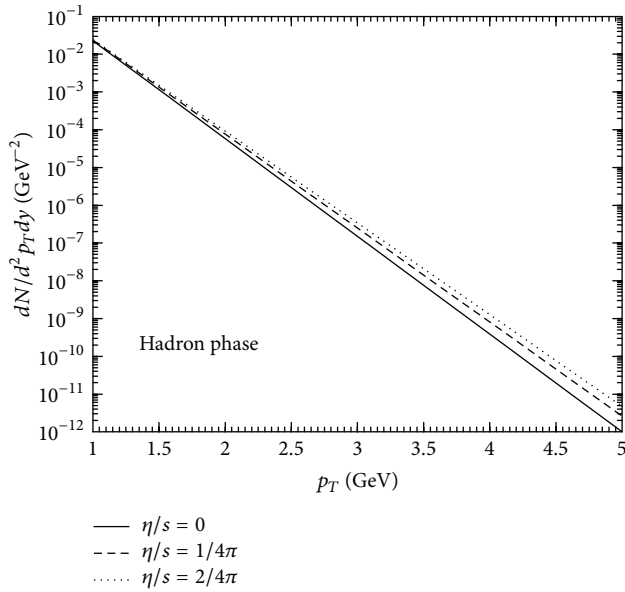

FIGURE 14: Transverse momentum distribution of photons from thermal hadrons for various values of η/s in the scenario (ii).

FIGURE 13: Transverse momentum distribution of photons from thermal hadrons for various values of η/s in the scenario (i).

FIGURE 15: Transverse momentum distribution of thermal photons from the entire evolution history of the system for various values of η/s in the scenario (i).

the effect is more prominent in scenario (i) than in (ii). It is also clearly seen that the effects of viscosity though the effect is stronger in the QGP phase than in the hadronic phase. It is expected that the observed shift in the photon spectra due to viscous effects may be detected in future high precision experiments.

Finally in Figures 15 and 16 we plot the p_T spectra of photons for the entire life time of the thermal system; that is, the photon yield is obtained by summing up contributions from QGP, mixed and hadronic phases for different values of
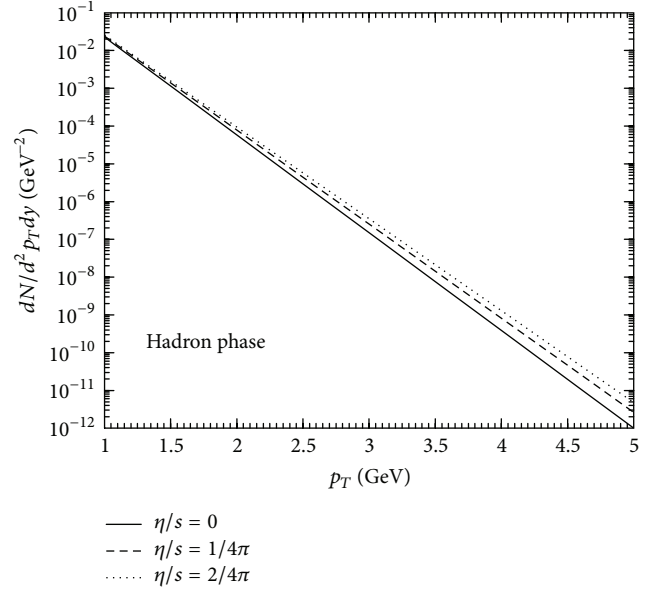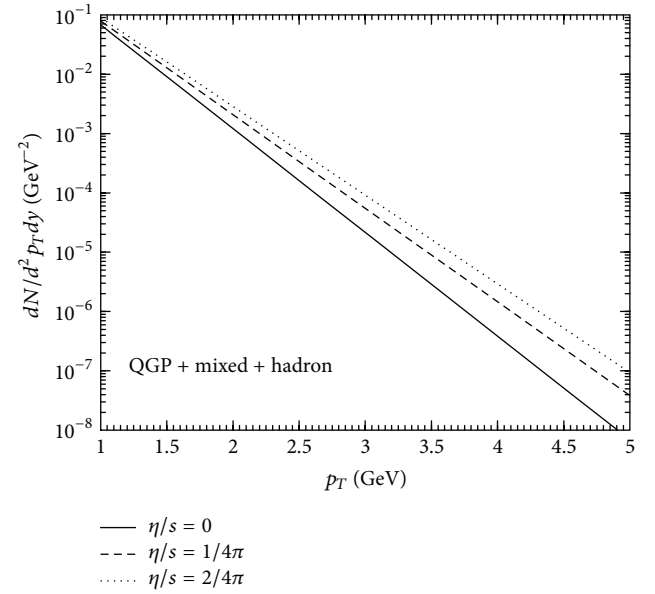
η/s for scenario (i) and (ii), respectively. The effect of viscosity for the scenario (i) is stronger than (ii).

6. Emission of Thermal Dileptons from Heavy Ion Collision

Unlike real photon, dilepton is massive. Thus dilepton has two kinematic variables, invariant mass (M) and transverse momentum (p_T). Again, the p_T spectra are affected due to
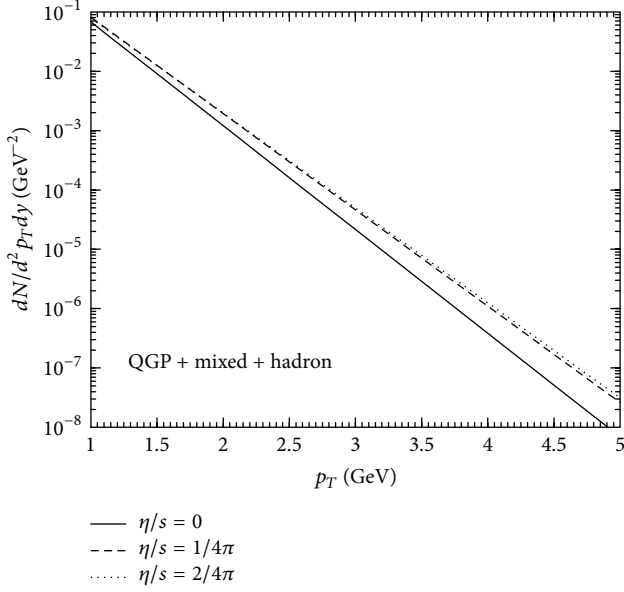
FIGURE 16: Transverse momentum distribution of thermal photons from the entire evolution history of the system for various values of η/s in the scenario (ii).

flow, whereas the p_T-integrated M spectra remain unaltered by flow. By tuning these two parameters, different stages of expanding fireball can be understood. Dileptons having large M and high p_T are emitted early from the hot zone of the system. On the other hand, those having lower M and p_T produced at later stage of the fireball when the temperature is low. Because of an additional variable, the invariant pair mass M, dileptons have the advantage over real photons [99].

The production of thermal dileptons from QGP (Section 6.1) and hot hadronic gas (Section 6.2) is described below.

6.1. Dileptons Emission from QGP. In the QGP, where quarks and gluons are the relevant degrees of freedom, the $W_{\mu\nu}$ can be directly evaluated by writing the electromagnetic current in terms of quarks of flavor f, that is, $J_\mu^{em} = \sum_f e_f \overline{\psi}_f \gamma_\mu \psi_f$. Confining to the leading order contribution we obtain

$$g^{\mu\nu} W_{\mu\nu} = -\frac{3q^2}{2\pi} \sum_f e_f^2 \left(1 - \frac{4m_q^2}{q^2} \right). \tag{52}$$

The rate in this case corresponds to dilepton production due to process $q\overline{q} \to \gamma^* \to l^+l^-$. The static thermal emission rate of dilepton from QM is given by $(q\overline{q} \to \gamma^* \to l^+l^-)$ [100, 101] (also [102, 103]),

$$\frac{dR_{l^+l^-}}{d^4p} = -\frac{\alpha^2}{4\pi^4} L\left(M^2\right) f_{BE} \sum_f e_f^2 \left[1 + \frac{2T}{\vec{p}} \ln\left(\frac{n_+}{n_-}\right) \right], \tag{53}$$

where e_f is the charge of the quark and $n_\pm = 1/(e^{(p_0 \pm |\vec{p}|/2T)+1})$.

6.2. Dileptons Emission from Hot Hadronic Gas. To obtain the rate of dilepton production from hadronic interactions it is convenient to break up the quark current J_μ^h into parts with definite isospin:

$$J_\mu^h = \frac{1}{2} \left(\overline{u}\gamma_\mu u - \overline{d}\gamma_\mu d \right) + \frac{1}{6} \left(\overline{u}\gamma_\mu u + \overline{d}\gamma_\mu d \right) + \cdots$$
$$= J_\mu^V + J_\mu^S + \cdots = J_\mu^\rho + \frac{J_\mu^\omega}{3} + \cdots, \tag{54}$$

where V and S denote iso-vector and iso-scalar currents and the dots denote currents comprising of quarks with strangeness and heavier flavors. These currents couple to individual hadrons as well as multiparticle states with the same quantum numbers and are usually labeled by the lightest meson in the corresponding channel [104]. We thus identify the isovector and isoscalar currents with the ρ and ω mesons, respectively. Defining the correlator of these currents $W_{\mu\nu}^{\rho,\omega,\phi}$ analogously as in (7), we can write

$$W_{\mu\nu} = W_{\mu\nu}^\rho + \frac{W_{\mu\nu}^\omega}{9} + \cdots. \tag{55}$$

The correlator of vector-isovector currents $W_{\mu\nu}^\rho$ has in fact been measured [105, 106] in vacuum along with the axial-vector correlator by studying τ decays into even and odd number of pions. The former is found to be dominated at lower energies by the prominent peak of the ρ meson followed by a continuum at high energies. The axial correlator, on the other hand, is characterized by the broad hump of the a_1. The distinctly different shape in the two spectral densities is an experimental signature of the fact that chiral symmetry of QCD is dynamically broken by the ground state [107]. It is expected that this symmetry may be restored at high temperature and/or density and will be signaled by a complete overlap of the vector and axial-vector correlators [17].

In the medium, both the pole and the continuum structure of the correlation function gets modified [8, 108]. We will first evaluate the modification of the pole part due to the self-energy of vector mesons in the following. Using vector meson dominance the isovector and scalar currents are written in terms of dynamical field operators for the mesons allowing us to express the correlation function in terms of the exact (full) propagators or the interacting spectral functions of the vector mesons in the medium. To reach that goal we have to specify the coupling of the currents to the corresponding vector fields. For this purpose we write, in the narrow width approximation [104],

$$\left\langle 0 \left| J_\mu^{em}(0) \right| R \right\rangle = F_R m_R \epsilon_\mu, \tag{56}$$

where R denotes the resonance in a particular channel and ϵ_μ is the corresponding polarization vector. The coupling constants F_R are obtained from the partial decay widths into e^+e^- through the relation

$$F_R^2 = \frac{3m_R \Gamma_{R \to e^+e^-}}{4\pi\alpha^2} \tag{57}$$

yielding F_R = 0.156 GeV, 0.046 GeV, and 0.079 GeV for ρ, ω, and ϕ, respectively. Equation (56) suggests the operator relations:

$$J_\mu^\rho(x) = F_\rho m_\rho V_\mu^\rho(x),$$
$$J_\mu^\omega(x) = 3F_\omega m_\omega V_\mu^\omega(x), \text{ and so forth,} \quad (58)$$

where $V_\mu^{\rho(\omega)}(x)$ denotes the field operator for the $\rho(\omega)$ meson. So using the above relations connecting currents to fields (so-called field-current identity), the current commutator becomes

$$W_{\mu\nu} = \sum_{R=\rho,\omega,...} F_R^2 m_R^2 \int d^4x e^{iq\cdot x} \left\langle \left[V_\mu^R(x), V_\nu^R\right]\right\rangle$$
$$= \sum_{R=\rho,\omega,...} F_R^2 m_R^2 A_{\mu\nu}^R(q_0, \vec{q}) \quad (59)$$
$$= 2\epsilon(q_0) \sum_{R=\rho,\omega,...} F_R^2 m_R^2 \operatorname{Im} \overline{D}_{\mu\nu}^R(q_0, \vec{q}),$$

where $A_{\mu\nu}^R$ are the spectral functions of corresponding vector meson resonances (R) and $\overline{D}_{\mu\nu}^R$ is the diagonal element of the thermal propagator matrix. The form of the diagonal element of the exact thermal propagator matrix for the spin 1 particle is given by

$$\overline{D}_{\mu\nu}^R(q) = \overline{G}_{\mu\nu}^R - \frac{q_\mu q_\nu}{q^2 m_R^2}, \quad (60)$$

where

$$\overline{G}_{\mu\nu}^R = -\frac{P_{\mu\nu}}{q^2 - m_R^2 - \overline{\Pi}_t^R(q)} - \frac{Q_{\mu\nu}/q^2}{q^2 - m_R^2 - q^2\overline{\Pi}_l^R(q)}. \quad (61)$$

The imaginary part is then put in (59) and then in (6) to arrive at the dilepton emission rate:

$$\frac{dN}{d^4q d^4x} = \frac{\alpha^2}{\pi^3 q^2} L(q^2) f_{BE}(q_0)$$
$$\times \left[F_\rho^2 m_\rho^2 A_\rho(q_0, \vec{q}) + F_\omega^2 m_\omega^2 A_\omega(q_0, \vec{q}) + \cdots\right], \quad (62)$$

where, for example, $A_\rho(= -g^{\mu\nu} \operatorname{Im} \overline{D}_{\mu\nu}^\rho/3)$ is given by

$$A_\rho = -\frac{1}{3}\left[\frac{2\sum \operatorname{Im} \overline{\Pi}_t^R}{\left(q^2 - m_\rho^2 - \sum \operatorname{Re} \overline{\Pi}_t^R\right)^2 + \left(\sum \operatorname{Im} \overline{\Pi}_t^R\right)^2}\right.$$
$$\left. + \frac{q^2 \sum \operatorname{Im} \overline{\Pi}_l^R}{\left(q^2 - m_\rho^2 - q^2 \sum \operatorname{Re} \overline{\Pi}_l^R\right)^2 + q^4\left(\sum \operatorname{Im} \overline{\Pi}_l^R\right)^2}\right], \quad (63)$$

the sum running overall meson loops πH and baryon loops NB. Here $\overline{\Pi}_{t,l}^R$ is the diagonal element of vector meson ($R = \rho$ and ω) self-energy at finite temperature and density which
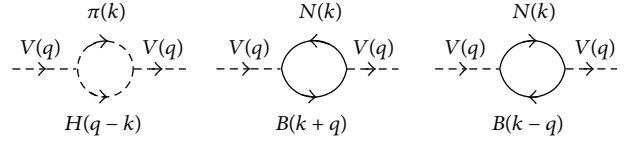

FIGURE 17: One-loop Feynman diagrams for ρ or ω self-energy involving mesons (first figure) and baryons (second and third figures). V stands for the ρ or ω in the external line. In the internal lines of meson loops, $H = \pi, \omega, a_1,$ and h_1 for $V = \rho$ whereas $H = \rho$ for $V = \omega$. For the baryonic loops, N and B indicate, respectively, nucleon and baryonic internal lines.

is also a matrix in the real-time formalism. We have taken $H = \pi, \omega, a_1, h_1$ [109] and $B = N(940), N^*(1520), N^*(1650), N^*(1700), N^*(1720), \Delta(1230),$ and $\Delta^*(1620)$ [110] for ρ meson whereas for ω meson, $H = \rho$ (with $\pi\pi$ folding), and $B = N(940), N^*(1440), N^*(1520), N^*(1535), N^*(1650),$ and $N^*(1720)$ [111] are taken. These self-energy graphs are diagrammatically represented in Figure 17.

The general expression of $\overline{\Pi}_{t,l}^R$ for meson loop πH (representing the first diagram of Figure 17) is given by [109, 111]

$$\overline{\Pi}_{t,l}^R(q) = \int \frac{d^3k}{(2\pi)^3} \frac{1}{4\omega_\pi \omega_H}$$
$$\times \left[\frac{\left(1 + n^\pi\right) L_{t,l}^1 + n^H L_{t,l}^3}{q_0 - \omega_\pi - \omega_H + i\eta\epsilon(q_0)}\right.$$
$$+ \frac{-n^\pi L_{t,l}^1 + n^H L_{t,l}^4}{q_0 - \omega_\pi + \omega_H + i\eta\epsilon(q_0)} \quad (64)$$
$$+ \frac{n^\pi L_{t,l}^2 - n^H L_{t,l}^3}{q_0 + \omega_\pi - \omega_H + i\eta\epsilon(q_0)}$$
$$\left. + \frac{-n^\pi L_{t,l}^2 - \left(1 + n^H\right) L_{t,l}^4}{q_0 + \omega_\pi + \omega_H + i\eta\epsilon(q_0)}\right],$$

where n's are Bose-Einstein distribution functions for the internal meson lines and ω's are their on-shell energies. In the above expression $L_{t,l}^{i=1,...,4}$ denote the values of $L_{t,l}(k_0)$ for $k_0 = \omega_\pi, -\omega_\pi, q_0 - \omega_H,$ and $q_0 + \omega_H$, respectively. The corresponding expression for the baryon loop NB (second diagram of Figure 17) is given by [110, 111]

$$\overline{\Pi}_{t,l}^R(q) = \int \frac{d^3k}{(2\pi)^3} \frac{1}{4\omega_N \omega_B}$$
$$\times \left[\frac{\left(1 - n_+^N\right) L_{t,l}^1 - n_-^B L_{t,l}^3}{q_0 - \omega_N - \omega_B + i\eta\epsilon(q_0)}\right.$$
$$+ \frac{n_+^N L_{t,l}^1 - n_+^B L_{t,l}^4}{q_0 - \omega_N + \omega_B + i\eta\epsilon(q_0)} \quad (65)$$
$$+ \frac{-n_-^N L_{t,l}^2 + n_-^B L_{t,l}^3}{q_0 + \omega_N - \omega_B + i\eta\epsilon(q_0)}$$
$$\left. + \frac{n_-^N L_{t,l}^2 + \left(-1 + n_+^B\right) L_{t,l}^4}{q_0 + \omega_N + \omega_B + i\eta\epsilon(q_0)}\right],$$
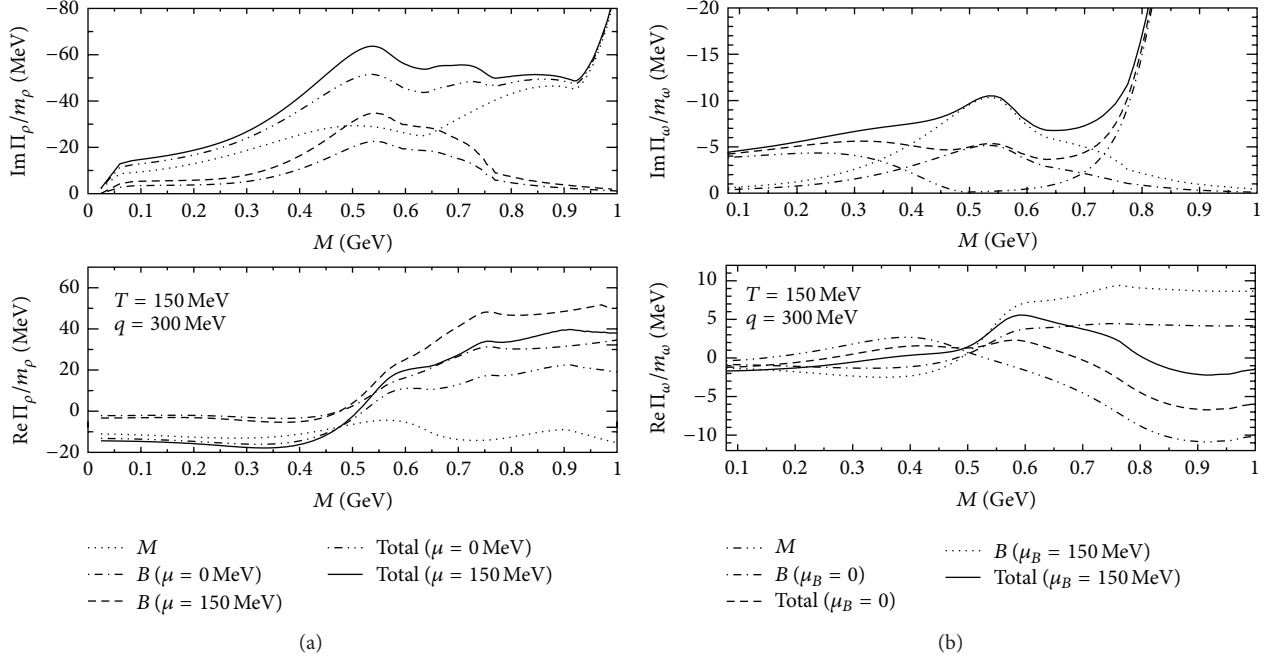
FIGURE 18: The imaginary (upper) and real (lower) part of self-energy function of ρ (a) and ω (b) at different chemical potential (μ or μ_B). The contribution coming from meson, baryon loops, and their sum is shown.

where $n_{+(-)}$'s are Fermi-Dirac distribution functions for the internal baryon (antibaryon) lines. Here, $L_{t,l}^{i=1,\ldots,4}$ denote the values of $L_{t,l}(k_0)$ for $k_0 = \omega_N$, $-\omega_N$, $q_0 - \omega_B$, $q_0 + \omega_B$, respectively. The expression for the third diagram of Figure 17 can be obtained by changing the sign of the external momentum q in (65).

The numerical results for the ρ and ω meson self-energy are, respectively, shown in Figures 18(a) and 18(b). The individual contribution from the meson and baryon loops is also shown for two values of the baryon chemical potential. For both ρ and ω mesons, the small positive contribution from the baryon loops to the real part is partly compensated by the negative contributions from the meson loops which can be clearly seen in the lower panels of Figure 18.

We now use these self-energy functions in the expression for the exact propagator (60) to obtain an explicit results of in-medium spectral functions for ρ and ω meson. In view of the fact that the ρ and ω peaks are close to each other, it is worthwhile to compare their relative spectral strengths below their nominal masses. This is shown in Figure 19 for two values of the chemical potential. The characteristic 2π and 3π thresholds for the ρ and ω in the vacuum case are also visible. At fixed temperature and density, the ω contribution is lower than ρ but of comparable magnitude below their nominal masses. However, the fact that the ω is suppressed by a factor ~ 10 ($\simeq F_\rho^2/F_\omega^2$) compared to the ρ in the dilepton emission rate makes a quantitative study of the ω difficult. In the above expressions the meson (H) and baryon resonances (B) have been treated in the narrow width approximation. These have then been folded with the width of the resonances as shown in [110].
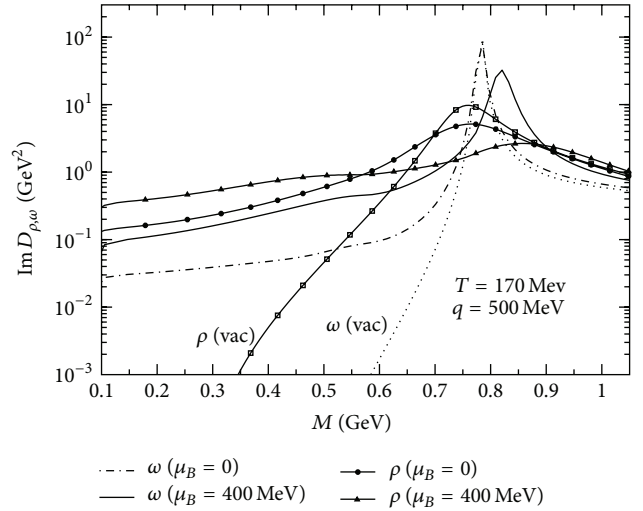

FIGURE 19: The ω spectral function seen in comparison with the ρ.

Thus, the dilepton emission rate in the present scenario actually boils down to the evaluation of the self-energy graphs of ρ and ω as a function of q_0, $\vec{q}$, temperature (T), and net baryon density (ρ_B). Using those functions in (63) we can get a numerical estimation of dilepton static rates. With all the ingredients discussed previously, we have calculated the static emission rate of dilepton from QGP and hadronic matter. The emission rate from both the phases is plotted in Figure 20 for a given temperature of 175 MeV and baryonic chemical potential of 30 MeV. We observe significant enhancement in the dilepton yield in the mass region below the ρ pole
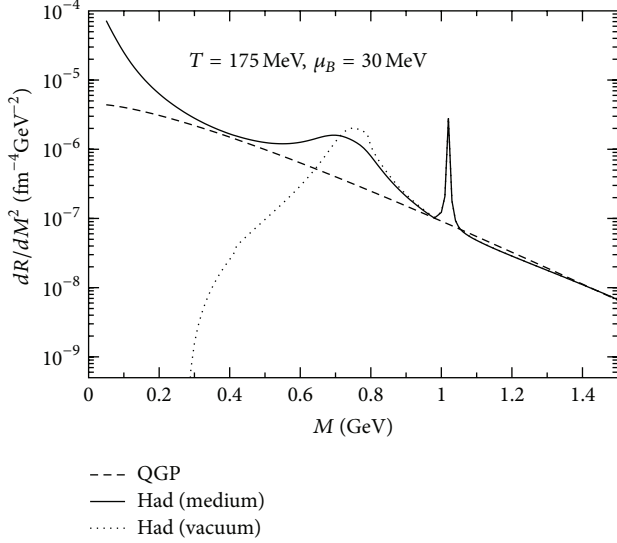
FIGURE 20: The dilepton emission rate from different sources at $T = 175$ MeV and $\mu_B = 30$ MeV.

compared to vacuum. This rate has been used in the analysis of the dimuon spectra obtained from In-In collisions at 17.3 GeV at CERN SPS [112, 113] (discussed in Section 6.4.1). The calculations show a reasonable agreement with the invariant mass spectra for different p_T ranges as well as the M_T spectra for different M bins.

As indicated earlier, coupling of the hadronic current to multiparticle states gives rise to a continuum structure in the current correlation function $W^{\mu\nu}$. Following [104], we take a parameterized form for this contribution and augment the dilepton emission rate with

$$\frac{dN}{d^4 q d^4 x} = \frac{\alpha^2}{\pi^3} L\left(q^2\right) f_{BE}\left(q_0\right) \sum_{V=\rho,\omega} A_V^{\text{cont}}, \qquad (66)$$

where

$$A_\rho^{\text{cont}} = \frac{1}{8\pi}\left(1 + \frac{\alpha_s}{\pi}\right)\frac{1}{1 + \exp\left(\omega_0 - q_0\right)/\delta} \qquad (67)$$

with $\omega_0 = 1.3, 1.1$ GeV for ρ, ω, and $\delta = 0.2$ for both ρ and ω. The continuum contribution for the ω contains an additional factor of $1/9$.

6.3. Invariant Mass and Momentum Spectra of Dileptons.
The total invariant transverse momentum distribution of thermal dileptons (l^+l^-) is obtained as follows:

$$\frac{d^2 N_{l^+l^-}}{d^2 p_T dy} = \sum_{i=Q,M,H} \int_i \left(\frac{dR_{l^+l^-}}{d^2 p_T dy dM^2}\right)_i M dM d^4 x. \qquad (68)$$

In a similar manner, the invariant transverse mass distribution of thermal dileptons (l^+l^-) can be obtained by integrating static emission rate over certain p_T window and by convoluting that by four volume and expressed as follows:

$$\frac{d^2 N_{l^+l^-}}{2M dM dy} = \sum_{i=Q,M,H} \int_i \left(\frac{dR_{l^+l^-}}{d^2 p_T dy dM^2}\right)_i p_T dp_T d^4 x. \qquad (69)$$

The limits for integration over p_T and M can be fixed judiciously to detect contributions either from quark matter or hadronic matter. Experimental measurements [79, 114, 115] are available for different M window.

6.4. Results and Discussion on p_T and M Distributions of Dileptons.
Thus far we have discussed the dilepton emission rate for a given temperature. In HIC the dilepton yield is obtained by convoluting the static emission rate over space and time.

6.4.1. Dileptons at SPS Energy.
With all these ingredients the M_T and M spectra of dileptons measured by NA60 collaboration at SPS energy are reproduced as follows.
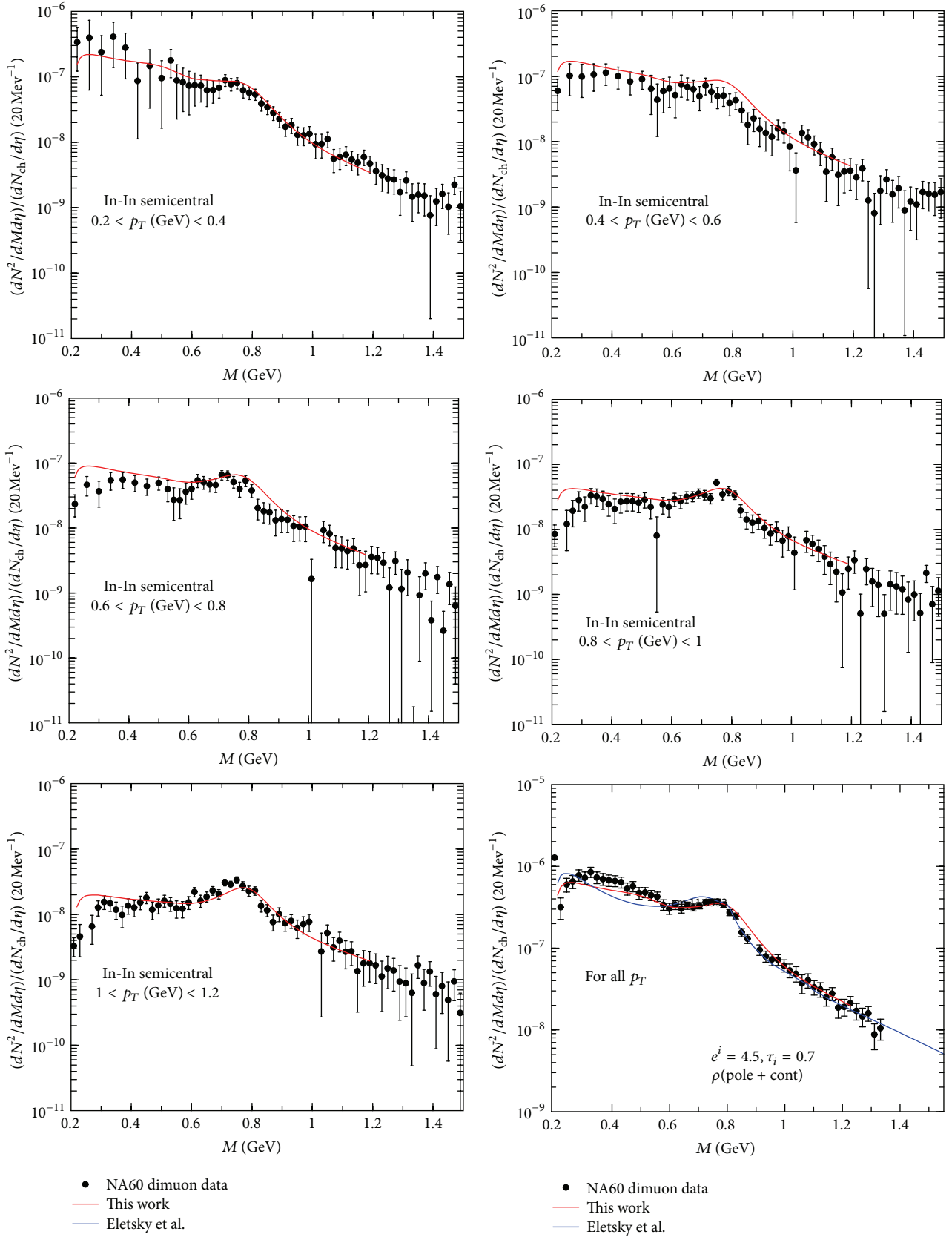
Finally, we have obtained the dimuon yield (dN/dM) in In-In collisions at SPS at a center of mass energy of 17.3 GeV. The initial energy density is taken as 4.5 GeV/fm^3 corresponding to a thermalisation time $\tau_i = 0.7$ fm, the QGP to hadronic matter transition temperature $T_c = 175$ MeV, and the freezeout temperature $T_f = 120$ MeV (fixed from the slope of the hadronic spectra measured by the NA60 Collaboration) has been taken to compare the data measured by NA60 collaboration. In Figure 21 we have shown the invariant mass spectra for different transverse momentum (p_T) windows calculated for 17.3 GeV energies.

The theoretical curves agree quite well with the experimental data [114, 115] for all the p_T ranges. The strong enhancement in the low M domain is clearly due to the large broadening of the ρ in the thermal medium which comes entirely from the Landau cut in the self-energy diagrams. In the last panel, the blue-dashed line curve is the result of a previous calculation [113] where the self-energy due to baryons has been evaluated following the approach of [116]. In the present work [112] we have included an exhaustive set of baryon loops using the real-time thermal field theoretical approach where we have employed the full relativistic baryon propagators in which baryons and anti-baryons appear on an equal footing. This [112] is seen to be in better agreement with the experimental data [114, 115] than [113] in the range $0.35 \leq M \leq 0.65$ GeV.

Apart from the M spectra, we have also evaluated the transverse mass spectra of dimuon pairs at SPS energy measured by NA60 collaboration [114, 115].

The results are compared with the data obtained by NA60 collaborations [114, 115, 117, 118] at SPS energy (Figure 22). Theoretical results contain contributions from the thermal decays of light vector mesons (ρ, ω, and ϕ) and also from the decays of vector mesons at the freezeout [10, 49] of the system has also been considered. The nonmonotonic variation of the effective slope parameter extracted from the M_T spectra of the lepton pair with $\langle M \rangle$ evaluated within the ambit of the present model [113] reproduces the NA60 [114, 115] results reasonably well.

6.4.2. Dileptons at RHIC Energy.
For Au+Au collisions at $\sqrt{s_{NN}} = 200$ GeV, we have evaluated the dilepton spectra for different invariant mass bins with the initial condition (min bias) shown in Table 1 and lattice QCD equation of

FIGURE 21: Dilepton invariant mass spectra for different p_T bins compared with the NA60 data.
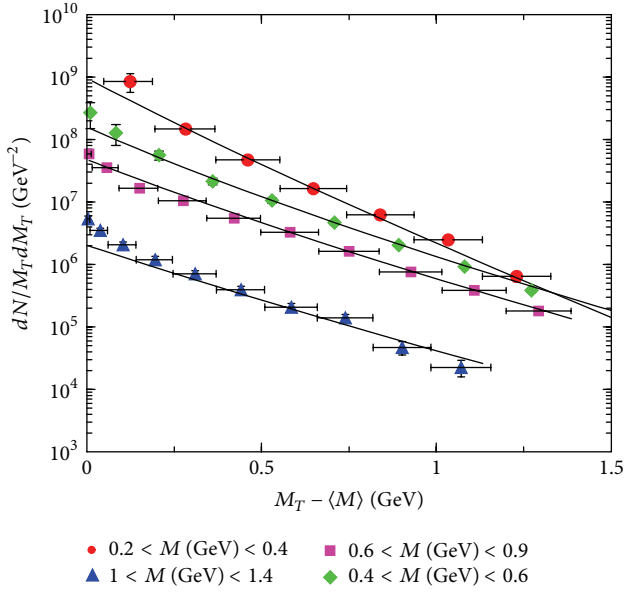
FIGURE 22: Transverse mass spectra of dimuons in In+In collisions at SPS energy. Solid lines denote the theoretical results [12].

FIGURE 23: Transverse momentum spectra of dileptons for different invariant mass windows for minimum bias Au-Au collisions at RHIC energy [12].

state. The results are displayed in **Figure 23**. The slopes of the experimental data on p_T distribution of lepton pairs for different invariant mass windows measured by the PHENIX collaboration [119, 120] could be reproduced well with the same initial condition that reproduces photon spectra [79]. In fact, the reproduction of data for the mass bins $0.5 < M(\text{GeV}) < 0.75$ and $0.81 < M(\text{GeV}) < 0.99$ does not need any normalization factors (**Figure 23**). For lower mass windows slopes are reproduced well but fail to reproduce the absolute normalization. Therefore, it should be clarified here that the theoretical results shown in **Figure 22** for lower mass windows (to be precise for $0.1 < M(\text{GeV}) < 0.2$, $0.2 < M(\text{GeV}) < 0.3$ and $0.3 < M(\text{GeV}) < 0.5$) contain arbitrary normalization constant.

Assuming 10% hard (i.e., $x = 0.10$) and 90% soft collisions for initial entropy production the value of $dN_{\text{pp}}^{\text{ch}}/dy$ turns out to be about 2.43 at $\sqrt{s} = 200$ GeV. For RHIC energy, we take $T_i = 320$ MeV with initial time $\tau_i = 0.2$ fm/c which acts as inputs to the hydrodynamic evolution.

For studying thermal dileptons at the RHIC energy (as well as the LHC energy) we have included the vacuum spectral function of ϕ meson because its mass appears at a boundary between quark and hadronic sources of dileptons.

We begin by plotting the space-time integrated invariant mass spectra of dileptons. In **Figure 24** we plot the yield of lepton pairs from the hadronic matter (HM), evaluated with and without the modified ρ spectral function for RHIC energy. The enhancement in the region $0.1 \leq M \leq 0.7$ GeV is purely a medium effect and is a contribution from the Landau cut of the meson and baryon loops. In contrast, the vacuum spectral function naturally starts from the $2m_\pi$ threshold coming from the unity in the unitary cut contribution. The (small) kink at 0.42 GeV in this curve is due to the $3m_\pi$
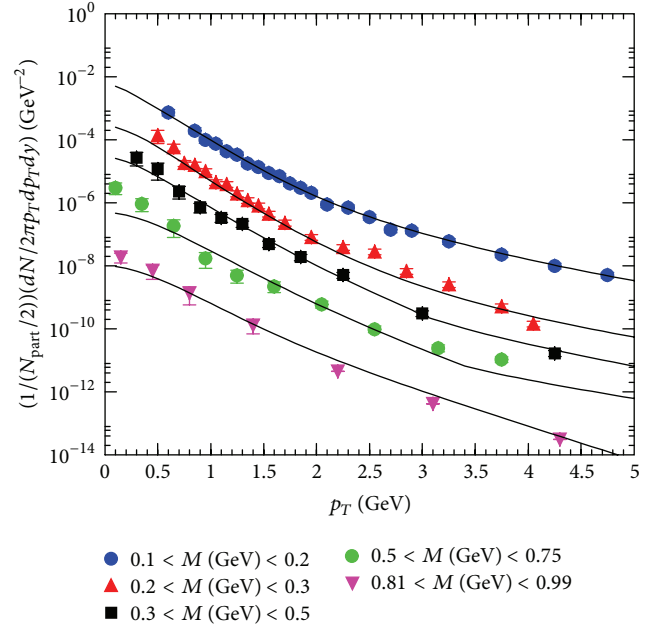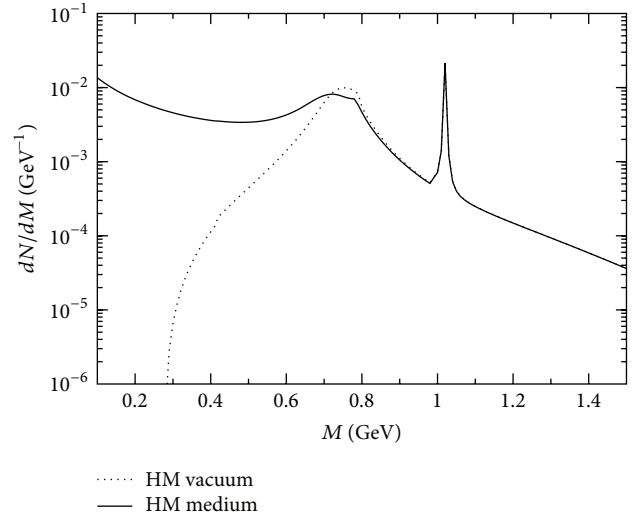

FIGURE 24: Invariant mass distribution of dileptons from hadronic matter (HM) for modified and unmodified ρ meson for RHIC energy.

threshold for ω production. The enhancement in the yield due to medium effects is ~20 for M around 400 MeV.

In **Figure 25**, we have shown the dependence of the yield from the two phases on the EoS. Dilepton radiation from hadronic phase outshines the emission from quark matter for M up to ϕ mass. Since the internal loops of ρ self-energy contain $a_{1\pi}$ and ω_π interactions, we ignore the four pion annihilation process [121] to avoid double counting. The contributions from quark matter phase dominate over its hadronic counter part for both the EoS for M beyond ϕ
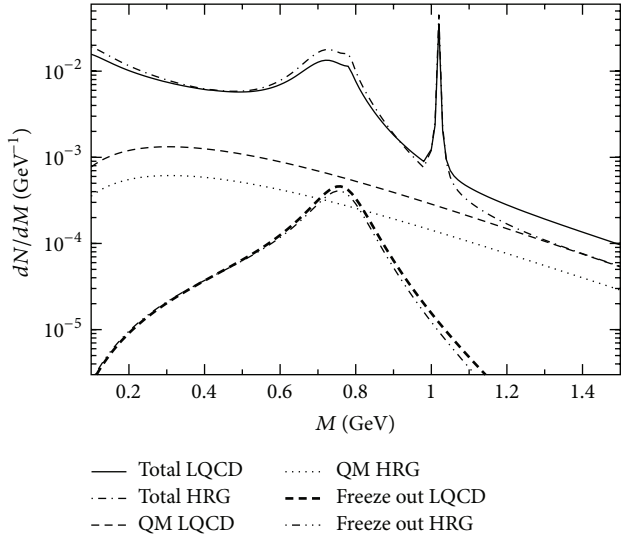
FIGURE 25: Freeze-out, QGP, and total contribution for EoS (a) HRG (dash-double dotted, dotted, and dash-dotted lines) and EoS (b) LQCD (bold dashed, dashed, and solid lines) at RHIC energy.

FIGURE 26: QGP and total contribution for EoS (a) HRG (dotted and dash-dotted lines) and EoS (b) LQCD (dashed and solid lines) at LHC energy.

peak. This fact may be used to extract various properties, that is, *average flow, temperature, and so forth* of quark matter and hadronic matter by selecting M windows judiciously. The dilepton yield from hadronic matter is observed to be larger when the HRG EoS is employed in comparison with LQCD. This can be understood in terms of the velocity of sound $c_s^2 (= \ dP/d\epsilon$ evaluated at constant entropy) which controls the rate of expansion. For EoS of the type (a) $c_s^2 \sim$ 1/3 in the QGP phase which is larger than the value of the corresponding quantity for EoS of the type (b). Therefore, the rate of expansion in the scenario (b) is comparatively slower, allowing the QGP to emit lepton pairs for a longer time resulting in greater yield for LQCD EoS. In contrast, for the EoS (a), the lower value of c_s^2 for the hadronic phase results in a slower cooling and hence a larger yield. Also shown for comparison is the yield from the decays of ρ mesons at the freezeout for the two types of EoS used. The yield from this source is much smaller and we will not consider it any further.

6.5. Dileptons at LHC Energy. At LHC the measured values of dN_{pp}^{ch}/dy for $\sqrt{s_{NN}}$ = 900 GeV, 2.36 TeV, and 7 TeV are 3.02, 3.77, and 6.01, respectively [122]. The value dN_{pp}^{ch}/dy at $\sqrt{s_{NN}}$ = 5.25 TeV is obtained by interpolating the above experimental data mentioned above. Assuming x = 0.2 in (26) we obtain dN/dy = 2607 in Pb+Pb collision for 0–10% centrality. For τ_i = 0.1 fm/c we get T_i = 756 MeV.

The invariant mass spectra of lepton pairs are displayed for LHC initial conditions in Figure 26. Although the results are qualitatively similar to RHIC, quantitatively the yield at LHC is larger by an order of magnitude, primarily because of the large initial temperature. This enhancement is also seen in the transverse mass distributions of the lepton pairs at LHC.

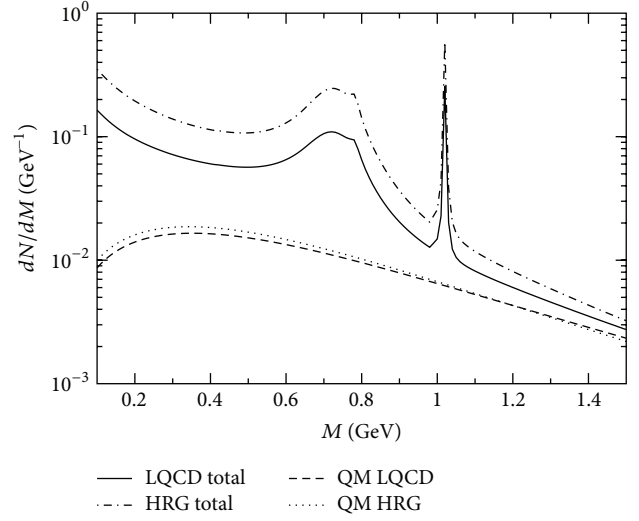All the results presented above for photon and dilepton production are reproduced using hydrodynamical model with cylindrical symmetry [64] and boost invariance along the longitudinal direction [41]. The two approximations, such as cylindrical symmetry and boost invariance, remain intact at very high p_T and in central collision. So our results will not differ much even if $(3+1)$ hydrodynamics is used at very high p_T and in central collision. In [123], the transverse momentum spectra of photons and v_2 of photons are calculated at RHIC energy using $(3 + 1)$ hydrodynamical model. Recently, in [124, 125], a realistic $(3 + 1)$ hydrodynamical model is established which can be used further to calculate the dilepton production, higher harmonics of flow of dileptons, interferometry with dileptons, and many more.

7. Radial Flow of Thermal Photons and Dileptons

The average magnitude of radial flow can be extracted from the transverse mass spectra $m_T (= \ \sqrt{p_T^2 + m_h^2})$ spectra of the hadrons only at freezeout surface. However, hadrons being strongly interacting objects can bring the information of the state of the system when it is too dilute to support collectivity; that is, the parameters of collectivity extracted from the hadronic spectra are limited to the evolution stage where the collectivity ceases to exist. These collective parameters have hardly any information about the interior of the matter. On the other hand, electromagnetic (EM) probes; that is, photons and dileptons are produced and emitted [1–8] from each space time point. Therefore, estimating radial flow from the EM probes will shed light on the time evolution of the collectivity in the system.

The calculations of EM probes from thermal sources depend on the parameters such as T_i, τ_i, T_{ch}, T_f, are EoS, which are not known uniquely. These abovementioned uncertainties have been used in the evaluation of individual single spectra of photon as well as dilepton. In order to
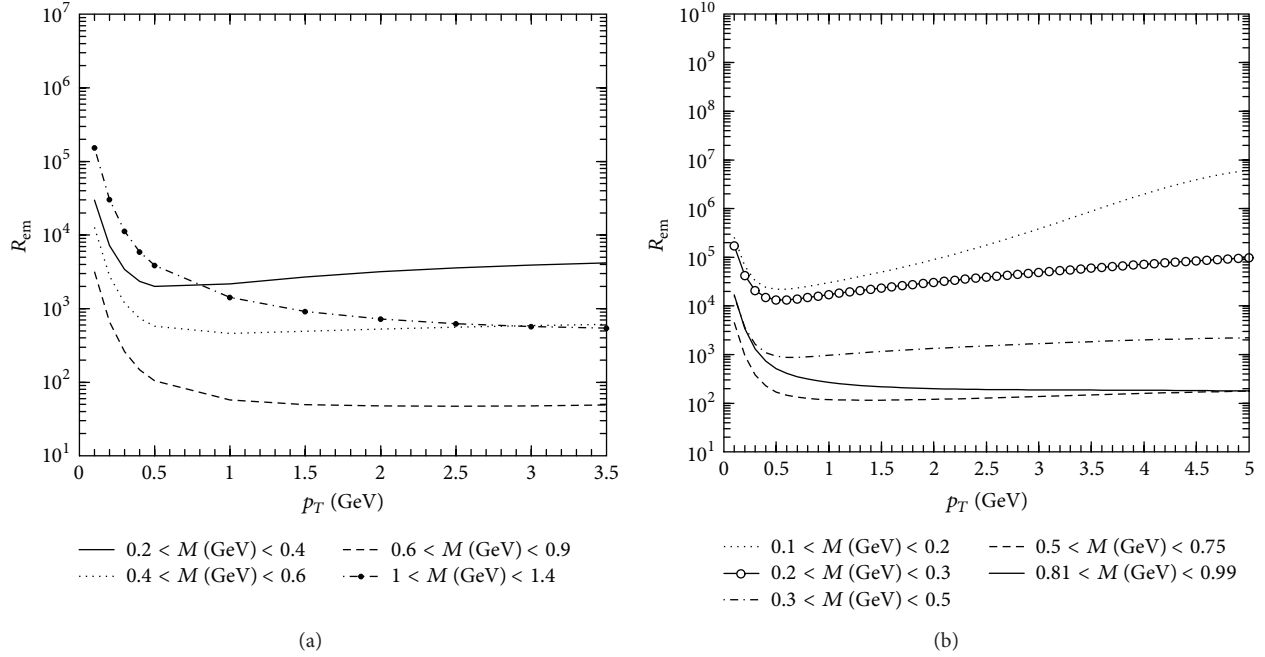
(a)

(b)

FIGURE 27: Variation thermal photon to dilepton ratio, R_{em}, with p_T for different invariant mass windows at SPS energy (a) and RHIC energy (b) (see text).

overcome the uncertainties and minimize the dependence of thermal sources on these parameters, the importance of the ratio of the transverse momentum spectra of photon to dilepton (R_{em}) has been emphasized in the present study (see [12, 16, 126, 127]), where the uncertainties are canceled out partially. It may be mentioned here that in the limit of $M \rightarrow 0$ the lepton pairs (virtual photons) emerge as real photons. Therefore, the evaluation of the ratio of the p_T spectra of photons to dileptons for various invariant mass bins along with a judicious choice of the p_T and M windows will be very useful to extract the properties of QGP as well as those of hadronic phase. This will be demonstrated in the present work by analyzing WA98 and PHENIX photons (results are shown in Section 5.4) and NA60 and PHENIX dilepton (results are shown in Section 6.4) spectra.

The p_T spectra of photon and dilepton can be parametrized as follows:

$$\left(\frac{dN}{d^2 p_T dy}\right)_\gamma = A_1 \left(\frac{1}{p_T}\right)^{B_1} \exp\left[-c_1 p_T\right]; \quad c_1 = \frac{1}{T_{eff_1}},$$

$$\left(\frac{dN}{d^2 p_T dy}\right)_{l^+ l^-} = A_2 \left(\frac{1}{M_T}\right)^{B_2} \exp\left[-c_2 M_T\right]; \quad c_2 = \frac{1}{T_{eff_2}},$$

$$(70)$$

where $T_{eff_1} = T_{av}\sqrt{(1 + v_r)/(1 - v_r)}$ is the blue-shifted effective temperature for massless photons and $T_{eff_2} = T_{av} + M v_r^2$ is the effective temperature for massive dileptons. T_{av} is the average temperature and v_r is the average radial flow of the system. The $T_{eff_{1,2}}$ can be obtained by parameterizing the p_T spectra of photons and dileptons (see Sections 5.4 and 6.4), respectively, with the expressed form of (70). The ratio, R_{em},

for different M windows (Figure 27) can be parametrized as follows:

$$R_{em} = A\left(\frac{M_T}{p_T}\right)^B \exp\left[-c\left(M_T - p_T\right)\right]; \quad c = \frac{1}{T_{eff}} \quad (71)$$

with different values of T_{eff} for different invariant mass windows. The argument of the exponential in (71) can be written as [126]

$$\frac{M_T - p_T}{T_{eff}} = \frac{M_T}{T_{eff_2}} - \frac{p_T}{T_{eff_1}}$$

$$= \frac{M_T}{T_{av} + M v_r^2} - \frac{p_T}{T_{av}\sqrt{(1 + v_r)/(1 - v_r)}}.$$

$$(72)$$

As mentioned before some of the uncertainties prevailing in the individual spectra may be removed by taking the ratio, R_{em}, of the p_T distribution of thermal photon to dileptons. In the absence of experimental data for both photon and dilepton from the same colliding system for SPS energies, we have calculated the ratio R_{em} for Pb+Pb system, where the initial condition and the EoS are constrained by the measured WA98 photon spectra. The results are displayed in Figure 27.

Also we evaluate the ratio of the thermal photon to dilepton spectra constrained by the experimental data from Au+Au collisions measured by PHENIX collaboration. The results for the thermal ratio, R_{em}, displayed in Figure 27(b) are constrained by the experimental data on the single-photon and -dilepton spectra. The behavior of R_{em} with p_T for different invariant mass windows which is extracted from the available data is similar to the theoretical results obtained
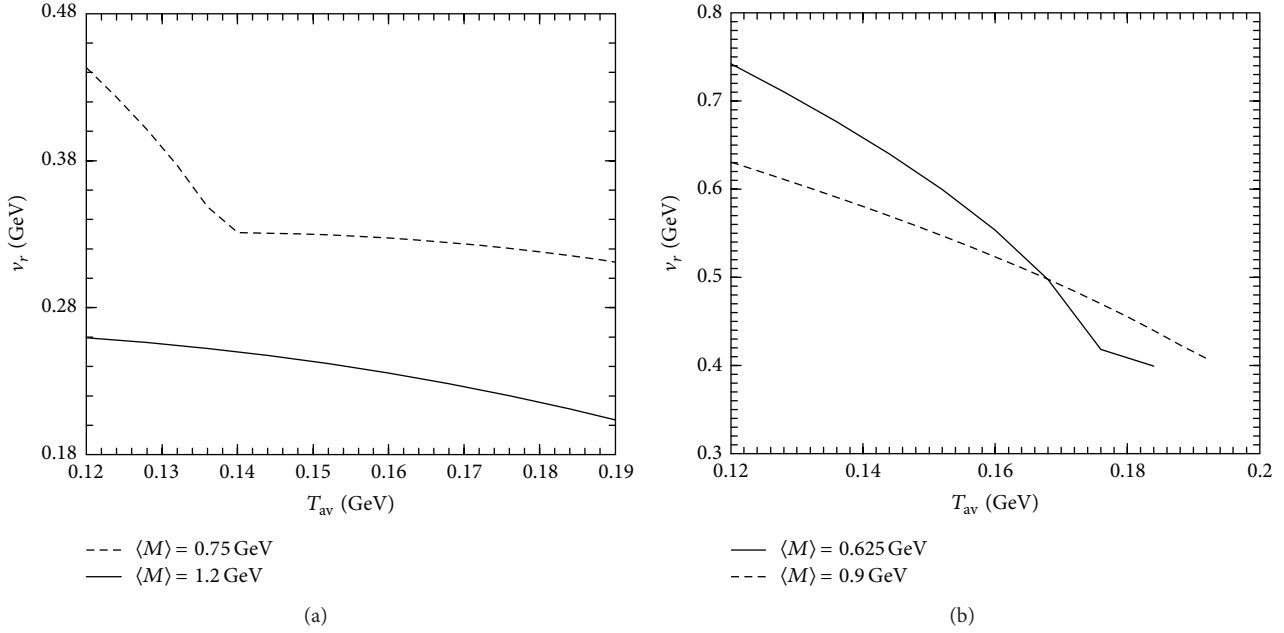
FIGURE 28: The variation of radial flow velocity with average temperature of the system for $\langle M \rangle$ = 0.75 GeV and 1.2 GeV at SPS energy (a) and for $\langle M \rangle$ = 0.625 GeV and 0.9 GeV at RHIC energy (b).

in [16, 126]. It is observed that the ratio decreases sharply and reaches a plateau beyond $p_T > 1.5$ GeV.

This behavior of R_{em} as a function of p_T can be understood as follows: (i) for $p_T \gg M$, $M_T \sim p_T$ and consequently $R_{em} \sim A$ giving rise to a plateau at large p_T. The height of the plateau is sensitive to the initial temperature of the system [16, 126] and (ii) for $p_T < M$, $R_{em} \sim \exp(-p_T/T_{eff})/p_T^B$ indicating a decrease of the ratio with p_T (at low p_T) as observed in Figure 27.

7.1. Variation of Radial Flow with Average Temperature. For a given p_T and M, (72) can be written as $v_r = f(T_{av})$. The T_{eff}'s are obtained from the ratio of individual spectra of photon and dilepton (by parametrising the R_{em} in Figure 27 using (71)). Thus we obtained the variation of radial flow with average temperature ($v_r(T_{av})$) for SPS (a) and RHIC (b) that has been depicted in Figure 28. It is clear from Figure 28 that the magnitude of the flow is larger in case of RHIC than SPS because of the higher initial pressure. Because of the larger initial pressure and QGP life time the radial velocity for QGP at RHIC is larger compared to SPS.

The T_{eff} obtained from the parametrization of ratio at SPS energy is 263 MeV and 243 MeV for M = 0.75 and 1.2 GeV, respectively. The average flow velocity v_r versus T_{av} has been displayed for M = 0.75 GeV and 1.2 GeV in Figure 28(a). The hadronic matter (QGP) dominates the $M \sim$ 0.75(1.2) GeV region. Therefore, these two mass windows are selected to extract the flow parameters for the respective phases. The v_r increases with decreasing T_{av} (increase in time) and reaches its maximum when the temperature of the system is minimum; that is, when the system attains T_f, the freezeout temperature. Therefore, the variation of v_r with T_{av} may be

treated as to show how the flow develops in the system. The v_r is larger in the hadronic phase because the velocity of sound in this phase is smaller, which makes the expansion slower, as a consequence system lives longer—allowing the flow to fully develop. On the other hand, v_r is smaller in the QGP phase because it has smaller life time where the flow is only partially developed. In Figure 28(b) the variation of average transverse velocity with average temperature for RHIC initial conditions is depicted.

7.2. Variation of Radial Flow with Invariant Mass. Obtaining T_{eff_1} and T_{eff_2} from the individual spectra and eliminating T_{av} one gets the variation of v_r with M. Figure 29(a) shows the variation of v_r with M for SPS conditions. The radial flow velocity increases with invariant mass M up to $M = M_\rho$ and then drops. How can we understand this behavior? From the invariant mass spectra, it is well known that the low M (below ρ mass) and high M (above ϕ peak) pairs originate from a partonic source [16]. The collectivity (or flow) does not develop fully in the QGP because of the small life time of this phase, which means that the radial velocity in QGP will be smaller for both low and high M. Whereas the lepton pairs with mass around ρ-peak mainly originate from a hadronic source (at a late stage of the evolution of system) are largely affected by the flow resulting in higher values of flow velocity. In summary, the value of v_r for M below and above the ρ-peak is small but around the ρ peak is large— with the resulting behavior displayed in Figure 29. Similar nonmonotonic behavior is observed in case of elliptic flow of photon as a function of p_T [128]. The variation of v_r with M in RHIC (Figure 29(b)) is similar to SPS though the values
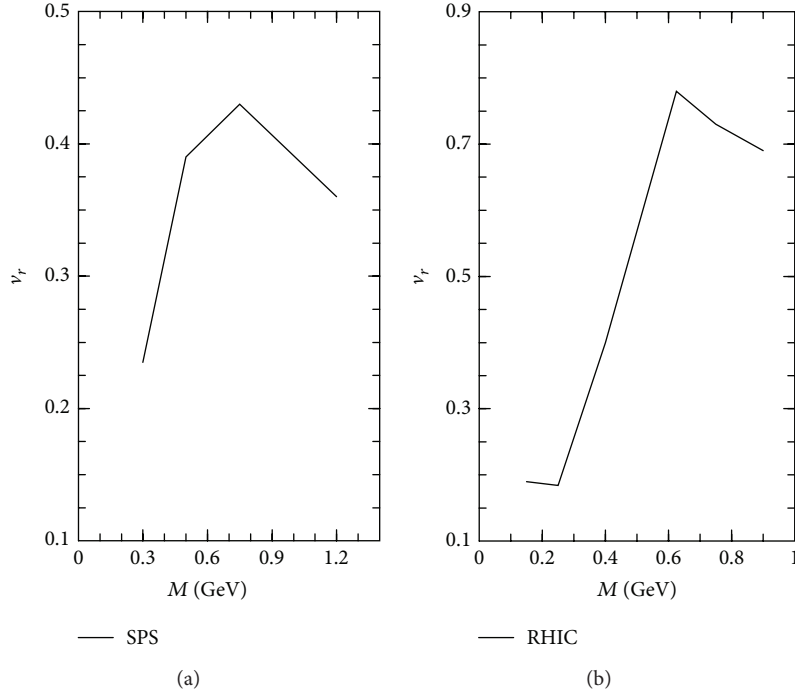
(a)

(b)

FIGURE 29: The variation of radial flow with invariant mass pairs for SPS (a) and RHIC (b) energies.

of v_r at RHIC are larger than those of SPS as expected due to higher initial pressure.

It is shown that simultaneous measurements of photon and dilepton spectra in HIC will enable us to quantify the evolution of the average radial flow velocity for the system, and the nature of the variation of radial flow with invariant mass indicates the formation of partonic phase at SPS and RHIC energy. The stronger radial flow at RHIC compared to SPS is due to higher initial energy densities and a longer lifetime of the reaction zone.

8. Dilepton Interferometry

The two-particle intensity interferometry, commonly known as Hanbury Brown Twiss (HBT) interferometry [129], is considered as one of the efficient methods to extract the information of space-time structure of the fireball formed in HIC. The utility of the intensity interferometry with dileptons [14, 15] for extracting fireball properties is as follows. As EM radiation produces from each stages of HIC, it retains information of the fireball at each space-time point. In contrast to correlation studies with hadrons which give information of the system when the system has frozen out, two-particle intensity interferometry using lepton pairs [14, 15], or photon [130, 131], can provide the information on the history of evolution of hot matter efficiently because EM probes do not rescatter after its production. As argued previously, photons appear to be more restrictive compared to dilepton, and we have attempted to do the correlation calculations with dileptons. So that with judicious choice of p_T and M windows we can get the spatial as well as temporal information of QGP and the hadronic phases separately by making use of correlations between two dilepton pairs.

8.1. Formalism and Equation of Bose-Einstein Correlation Function (BECF). As interferometry of the dilepton pairs actually reflects correlations between two virtual photons, the analysis then concentrates on computing the Bose-Einstein correlation function (BECF) for two identical particles defined as

$$C_2\left(\vec{p}_1, \vec{p}_2\right) = \frac{P_2\left(\vec{p}_1, \vec{p}_2\right)}{P_1\left(\vec{p}_1\right) P_1\left(\vec{p}_2\right)}, \tag{73}$$

where $\vec{p}_i$ is the three momenta of the particle i, and $P_1(\vec{p}_i)$ and $P_2(\vec{p}_1, \vec{p}_2)$ represent the one- and two-particle inclusive lepton pair spectra, respectively, and is expressed as follows:

$$P_1\left(\vec{p}\right) = \int d^4 x \omega\left(x, K\right),$$

$$P_2\left(\vec{p}_1, \vec{p}_2\right) = P_1\left(\vec{p}_1\right) P_1\left(\vec{p}_2\right)$$

$$+ \frac{\lambda}{3} \int d^4 x_1 d^4 x_2 \omega\left(x_1, K\right) \tag{74}$$

$$\times \omega\left(x_2, K\right) \cos\left(\Delta x^\mu q_\mu\right),$$

where $K = (p_1 + p_2)/2$, $q_\mu = p_{1\mu} - p_{2\mu} = q_\mu$, $\Delta x_\mu = x_{1\mu} - x_{2\mu}$, $x_{i\mu}$ and $p_{i\mu}$ are four coordinates for position and momentum variables, respectively, and $\omega(x, K)$ is the source function related to the thermal emission rate of lepton pairs per unit four volume, expressed as as follows:

$$\omega\left(x, K\right) = \int_{M_1^2}^{M_2^2} dM^2 \frac{dR}{dM^2 d^2 K_T dy}. \tag{75}$$

TABLE 3: Values of the various parameters used in the relativistic hydrodynamical calculations.

Input	RHIC	LHC
dN/dy	1100	2376
T_i	290 MeV	640 MeV
τ_i	0.6 fm	0.1 fm
T_c	175 MeV	175 MeV
T_{ch}	170 MeV	170 MeV
T_{fo}	120 MeV	120 MeV
EoS	2 + 1 Lattice QCD	2 + 1 Lattice QCD

With further simplification, the C_2 can be redefined as

$$C_2\left(\vec{p}_1, \vec{p}_2\right) = 1 + \left(\frac{\lambda}{3} \frac{\left[\int d^4x\,\omega\left(x, K\right) \cos\left(\Delta\alpha\right)\right]^2}{P_1\left(\vec{p}_1\right) P_1\left(\vec{p}_2\right)}\right.$$
$$\left. + \frac{\left[\int d^4x\,\omega\left(x, K\right) \sin\left(\Delta\alpha\right)\right]^2}{P_1\left(\vec{p}_1\right) P_1\left(\vec{p}_2\right)}\right),$$

$$(76)$$

where $\Delta\alpha = \alpha_1 - \alpha_2$, $\alpha_i = \tau M_{iT} \cosh(y_i - \eta) - r p_{iT} \cos(\theta - \psi_i)$, $M_{iT} = \sqrt{p_{iT}^2 + M^2}$ is the transverse mass, y_i is the rapidity, and ψ_i's are the angles made by p_{iT} with the x-axis.

The inclusion of the spin of the virtual photon will reduce the value of $C_2 - 1$ by $1/3$. The correlation functions can be evaluated for different average mass windows, $\langle M \rangle (\equiv M_{l^+l^-}) = (M_1 + M_2)/2$. The leading order process through which lepton pairs are produced in QGP is $q\bar{q} \to l^+l^-$ [100, 101]. For the low M dilepton production from the hadronic phase the decays of the light vector mesons ρ, ω, and ϕ have been considered including the continuum [1, 5, 7, 8, 104]. Since the continuum part of the vector meson spectral functions is included in the current work, the processes like four pions annihilations [121] are excluded to avoid double counting.

For the space time the evolution of the system relativistic hydrodynamical model with cylindrical symmetry [64] and boost invariance along the longitudinal direction [41] has been used. The values of the parameters required for space-time evolution are displayed in Table 3. With all these ingredients we evaluate the correlation function C_2 for 0–5% Au+Au collisions centrality for RHIC at $\sqrt{s_{NN}} = 200$ GeV [132] and Pb+Pb collisions at for LHC at $\sqrt{s_{NN}} = 2.76$ TeV [133] for different invariant mass windows as a function of q_{side} and q_{out} which are related to transverse momenta of individual pair [134, 135]. By choosing appropriate phase space for the QGP and hadron gas and performing the space time integration using the initial condition tabulated in Table 3, the C_2 for different phase has been evaluated. We have evaluated the C_2 for $\langle M \rangle = 0.3, 0.5, 0.7, 1.2, 1.6,$ and 2.5 GeV. In Figure 30 the results for only three values of $\langle M \rangle$ corresponding to low and high mass which are expected to be dominated by radiations from QGP ($\langle M \rangle \sim 1.6$ GeV) and hadronic phase ($\langle M \rangle \sim 0.77$ GeV), respectively, are displayed.

In Figure 30, we plot the C_2 as a function of q_{side} and q_{out} for RHIC initial conditions as tabulated in Table 3. A clear difference of dilepton pair mass dependence of the BEC studied as a function of q_{side} is observed for the contributions from different M domains. The differences are however small when BEC is studied as a function of q_{out}.

8.2. Source Dimension. The source dimensions can be obtained by parameterizing the calculated correlation function of the dilepton pairs with the empirical (Gaussian) form:

$$C_2\left(q, K\right) = 1 + \lambda \exp\left(-R_i^2\left(K\right) q_i^2\right), \qquad (77)$$

where i stands for side, out, and long. Thus R_{side}, R_{out}, and R_{long} appearing in (77) are commonly referred to as HBT radii, which is measure of Gaussian widths of source size and can be expressed as follows:

$$R_{\text{side}}^2\left(K\right) = \left\langle \tilde{y}^2 \right\rangle,$$
$$R_{\text{out}}^2\left(K\right) = \left\langle \left(\tilde{x} - v_r \tilde{t}\right)^2 \right\rangle, \qquad (78)$$
$$R_{\text{long}}^2\left(K\right) = \left\langle \left(\tilde{z} - v_z \tilde{t}\right)^2 \right\rangle.$$

The q_{out}, q_{side}, and q_{long} can be expressed in terms of individual particle momenta as [136]

$$q_{\text{side}} = \left| \vec{q}_T - q_{\text{out}} \frac{\vec{K}_T}{K_T} \right| = \frac{2 p_{1T} p_{2T} \sqrt{1 - \cos^2\left(\psi_1 - \psi_2\right)}}{f\left(k_{1T}, k_{2T}\right)},$$

$$q_{\text{out}} = \frac{\vec{q}_T \cdot \vec{K}_T}{\left|K_T\right|} = \frac{\left(p_{1T}^2 - p_{2T}^2\right)}{f\left(k_{1T}, k_{2T}\right)}, \qquad (79)$$

$$q_{\text{long}} = p_{1z} - p_{2z} = p_{1T} \sinh y_1 - p_{2T} \sinh y_2,$$

where $f(k_{1T}, k_{2T}) = \sqrt{p_{1T}^2 + p_{2T}^2 + 2 p_{1T} p_{2T} \cos(\psi_1 - \psi_2)}$ and λ (in this review, $\lambda = 1/3$) represents the degree of chaotic of the source. The deviation of λ from $1/3$ will indicate the presence of nonthermal sources. A representative fit to the correlation functions is shown in Figure 30 (solid lines). While the radius (R_{side}) corresponding to q_{side} is closely related to the transverse size of the system and considerably affected by the collectivity, the radius (R_{out}) corresponding to q_{out} measures both the transverse size and duration of particle emission [136–139]. The extracted R_{side} and R_{out} for different $\langle M \rangle$ are shown in Figures 31(a) and 31(b), respectively.

8.2.1. Variation of R_{side} and R_{out} with $\langle M \rangle$

R_{side}. The variation of R_{side} for QGP, hadronic and QGP + hadronic phase, is obtained from the respective C_2 in that phase with an appropriate selection of phase space in space-time integration. Figure 31(a) shows nonmonotonic dependence of R_{side} on M, starting from a value close to QGP value (indicated by the dashed line); it drops with increase in M finally again approaching the QGP value for $\langle M \rangle > m_\phi$. It can be shown that $R_{\text{side}} \sim 1/(1 + E_{\text{collective}}/E_{\text{thermal}})$ [134, 135].
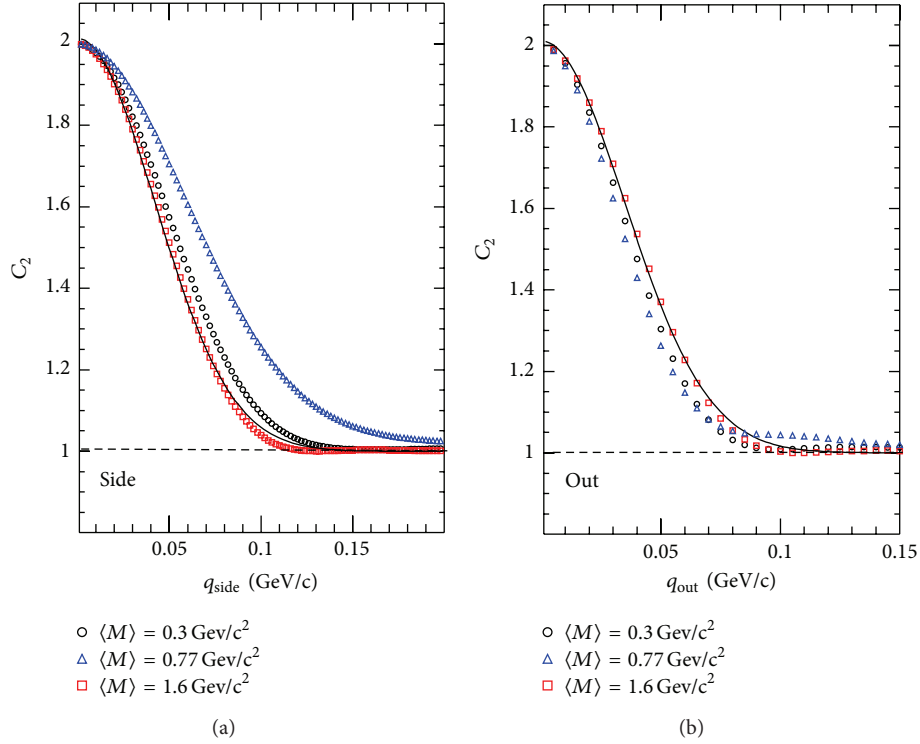
FIGURE 30: Correlation function for dilepton pairs as a function of q_{side} ((a), for $p_{1T} = p_{2T} = 2$ GeV and $\psi_2 = 0$) and q_{out} ((b), for $\psi_1 = \psi_2 = 0$ and $p_{1T} = 2$ GeV) for three values of $\langle M \rangle$ [14, 15]. The solid lines show the parameterization of C_2 using (77).
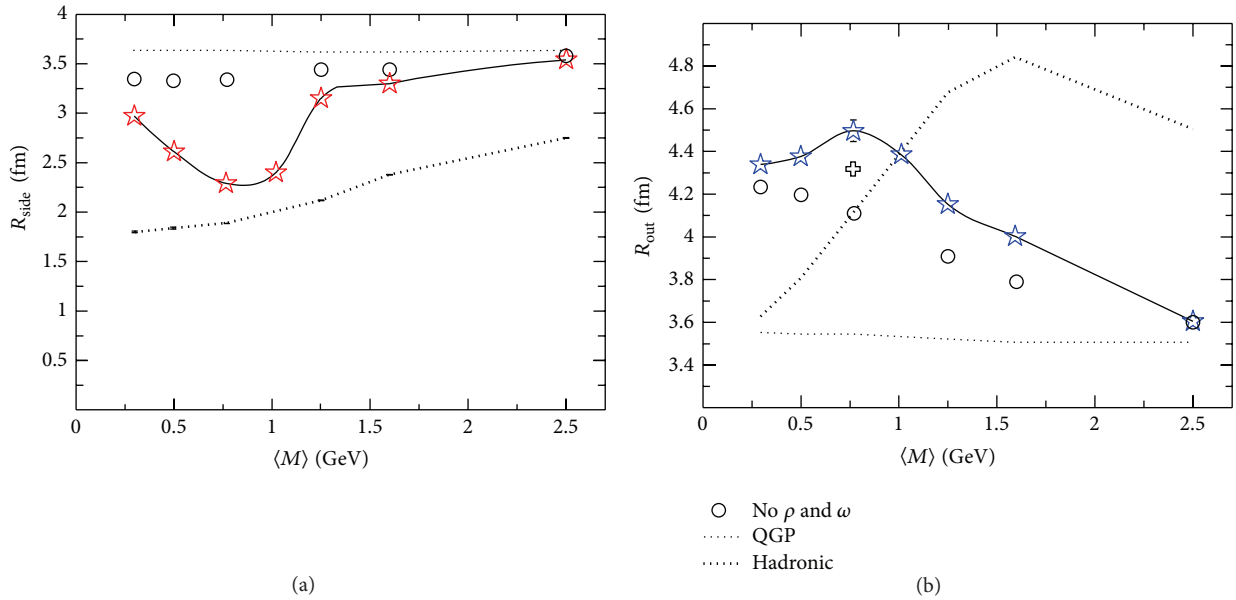

FIGURE 31: (a) R_{side} is evaluated with $p_{1T} = p_{2T} = 2$ GeV and $\psi_2 = 0$ as a function of $\langle M \rangle$ for RHIC energy and (b) R_{out} is evaluated with $\psi_1 = \psi_2 = 0$ and $p_{1T} = 2$ as a function of $\langle M \rangle$ for RHIC [14, 15].

In the absence of radial flow, R_{side} is independent of q_{side}. With the radial expansion of the system a rarefaction wave moves toward the center of the cylindrical geometry; as a consequence the radial size of the emission zone decreases with time. Therefore, the size of the emission zone is larger at early times and smaller at late time. The high $\langle M \rangle$ regions are dominated by the early partonic phase where the collective flow has not been developed fully; that is, the ratio of collective-to-thermal energy is small, and hence the source has larger R_{side}. In contrast, the lepton pairs with $M \sim m_\rho$
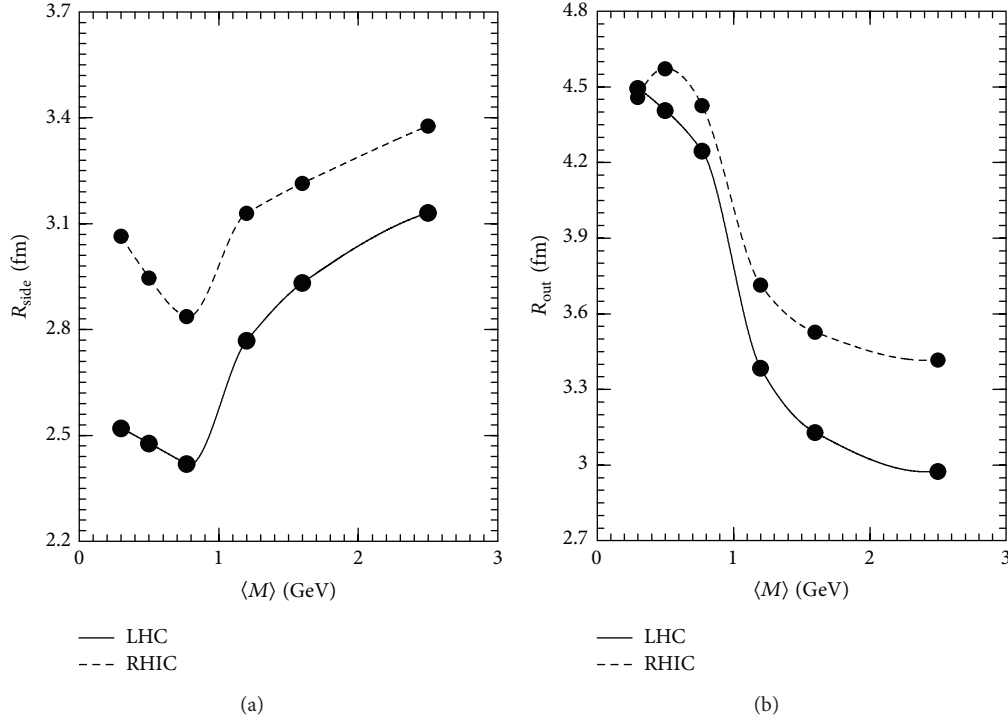
(a)

(b)

FIGURE 32: R_{side} (a) is evaluated with $p_{1T} = p_{2T} = 1$ GeV and $\psi_2 = 0$ and R_{out} (b) is evaluated with $p_{1T} = 1$ GeV and $\psi_1 = \psi_2 = 0$ as a function of $\langle M \rangle$ for RHIC (dashed line) and LHC (solid line) energies [14, 15].

are emitted from the late hadronic phase where the size of the emission zone is smaller due to larger collective flow giving rise to a smaller R_{side}. The ratio of collective to thermal energy for such cases is quite large, which is reflected as a dip in the variation of R_{side} with $\langle M \rangle$ around the ρ-mass region (Figure 31(a)). Thus the variation of R_{side} with M can be used as an efficient tool to measure the collectivity in various phases of matter. The dip in R_{side} at $\langle M \rangle \sim m_\rho$ is due to the contribution dominantly from the hadronic phase. We observe that, by keeping the ρ and ω contributions and setting radial velocity, $v_r = 0$, the dip in R_{side} vanishes, confirming the fact that the dip is caused by the radial flow of the hadronic matter. Therefore, the value of R_{side} at $\langle M \rangle \sim m_\rho$ may be used to estimate the average v_r in the hadronic phase.

R_{out}. The R_{out} probes both the transverse dimension and the duration of emission, and unlike R_{side} it does not remain constant even in the absence of radial flow. As a result its variation with M is complicated. The values R_{out} for different phases are obtained in a similar fashion as followed for obtaining the R_{side} values for the different phases. The large M regions are populated by lepton pairs from early partonic phase where the effect of flow is small and the duration of emission is also small—resulting in smaller values of R_{out}. For lepton pair from $M \sim m_\rho$ the flow is large which could have resulted in a dip as in R_{side} in this M region. However, R_{out} probes the duration of emission too which is large for hadronic phase because the expansion is slower in this phase for the EoS used in the present work. The velocity of sound which controls the rate of expansion and hence the

duration of the phase has larger value in hadronic phase than in the partonic phase. Thus resulting in the larger R_{out} in the hadronic phase than that in partonic phase, the larger duration compensates the reduction of R_{out} due to flow in the hadronic phase resulting is a bump in R_{out} in this region of M (Figure 31(b)). Again the duration of particle emission from both the phases obviously is larger than that from the individual phases.

Both R_{side} and R_{out} approach QGP values for $\langle M \rangle \sim$ 2.5 GeV implying dominant contributions from partonic phase.

8.3. Comparison of HBT Radii with Different Collision Energies. Now we study the sensitivity of the HBT radii on the different collision energy. The R_{side} and R_{out} extracted from the C_2's evaluated for 0–5% centrality in Au+Au collisions for RHIC at $\sqrt{s_{NN}}$ = 200 GeV [132] and Pb+Pb collisions for LHC at $\sqrt{s_{NN}}$ = 2.76 TeV [133] for different invariant mass windows as a function of q_{side} and q_{out} are shown in Figure 32. The change of R_{side} with $\langle M \rangle$ for RHIC and LHC is qualitatively similar but quantitatively different. The smaller values of R_{side} for LHC are due to the larger radial expansion which can be understood from the fact that the quantity $E_{\text{collective}}/E_{\text{thermal}}$ is larger at LHC than RHIC. So, the dip in the R_{side} variation at LHC is below than that at RHIC confirming a larger flow at LHC than RHIC. As the R_{out} probes both the transverse size and the duration of emission, from the previous discussion in Section 8.2.1, the larger duration compensates the reduction of R_{out} due to that flow resulting is a bump in R_{out} for $M \sim m_\rho$.
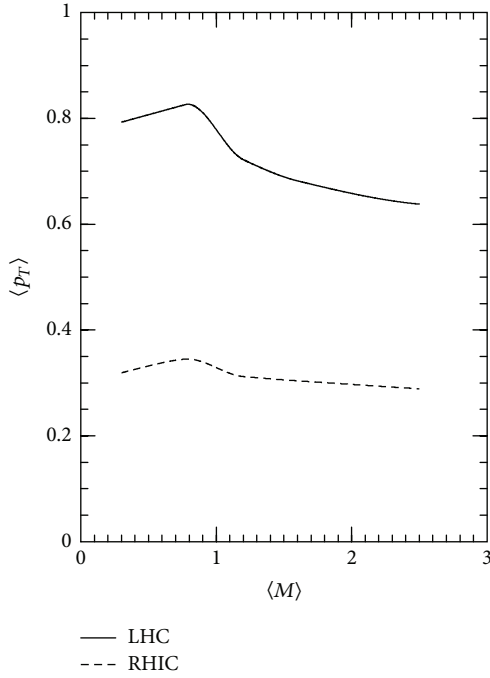
FIGURE 33: Variation of $\langle p_T \rangle$ as function of M (see (80)).

Though the duration of particle emission is more at LHC compared to RHIC (shown in Figure 36), the larger flow (corresponds to smaller size) at LHC [126] than that of RHIC compensates other factor (like duration of emission) which has an enhancing effect on R_{out}. So the value R_{out} at LHC is smaller than that of RHIC.

8.4. Radial Flow from HBT Radii. According to the discussion given in the Section 8.2, R_{side} is independent of q_{side} in the absence of radial flow. R_{side} is related to radial flow as follows:

$$R_{\text{side}}(M) = \frac{\mathscr{K}}{\langle p_T(M) \rangle}; \quad \langle P_T(M) \rangle = T_{\text{av}} + M v_r^2. \quad (80)$$

The values of $R_{\text{side}}(M)$ are obtained for different $\langle M \rangle$ windows (shown in Figure 31). The higher mass, that is, $\langle M \rangle = 2.5$ GeV, corresponds to the initial stage of collision where the flow is not developed fully. So assume for $\langle M \rangle = 2.5$, $v_r = 0$, and $T = T_i$ the value of $\mathscr{K} = T_i \times R_{\text{side}}|_{\langle M \rangle = 2.5}$. Once we know the value of $\mathscr{K}$, we can calculate the $\langle p_T(M) \rangle (= \mathscr{K}/R_{\text{side}}(M))$ The variation of $\langle p_T \rangle$ with $\langle M \rangle$ has been displayed in Figure 33.

The high $\langle M \rangle$ regions are dominated by the early partonic phase where the collective flow has not been developed fully and hence show smaller $\langle p_T \rangle$. In contrast, due to larger collective flow for the lepton pairs with $M \sim m_\rho$, emitted from the late hadronic phase, $\langle p_T \rangle$ is larger. The larger value of $\langle p_T \rangle$ around the ρ-mass region is due to the contribution of large flow in the hadronic phase. Thus the variation of R_{side} with M (Figure 31) can be used as an efficient tool to measure the collectivity in various phases of matter.

8.5. Sensitivity of HBT Radii on p_{iT}. In this section, the sensitivity of the HBT radii for different values of the individual transverse momentum of the pairs is described. In Figure 34, the variation of R_{side} and R_{out} with $\langle M \rangle$ is shown for $p_{1T} = 1$ and 2 GeV. The lepton pairs coming from higher p_T and high mass region enable us to quantify the size of hotter zone. As mentioned before, the p_T contains the effect of flow as well as thermal motion. Hence the larger R_{side} at $M \sim M_\rho$ for $p_T = 2$ GeV is associated with longer flow and hence smaller source size. The observed bump in R_{out} (Figure 34(b)) is resulted from the fact that it contains both the size of the system as well as the duration of dilepton emission as discussed earlier.

8.6. Duration of Particle Emission from HBT Radii. The HBT radii, R_{out} and R_{side}, provide the information of average source size. However, in the ratio, $R_{\text{out}}/R_{\text{side}}$, some of the uncertainties associated with the space time evolution get canceled out. The quantity, $R_{\text{out}}/R_{\text{side}}$ gives the duration of particle emission [134, 135, 140, 141] for various domains of M. The difference between $R_{\text{side}}^2(K)$ and $R_{\text{out}}^2(K)$ at nonzero in K is then only due to the explicit K dependence in (78), that is, the term $v_r \langle t^2 \rangle$. This implies that the explicit K dependence dominates if the emission duration is sufficiently large or if the position-momentum correlations in the source are sufficiently weak:

$$R_{\text{diff}}^2 = R_{\text{out}}^2(K) - R_{\text{side}}^2(K) = v_r \left\langle t^2 \right\rangle. \quad (81)$$

In this case, the difference between these two HBT radius parameters gives direct access to the average emission duration $\langle t^2 \rangle$ of the source and allows to partially disentangle the spatial and temporal information contained in (78).

Figure 35 shows the $R_{\text{out}}/R_{\text{side}}$ and the difference $\sqrt{R_{\text{out}}^2 - R_{\text{side}}^2}$ as a function of $\langle M \rangle$ for Au+Au collisions at $\sqrt{s_{NN}} = 200$ GeV. Both show a nonmonotonic dependence on $\langle M \rangle$. The smaller values of both the quantities, particularly at high mass region, reflect the contributions from the early partonic phase of the system. The peak around ρ-meson mass reflects dominance of the contribution from hadronic phase as discussed before. Figure 36 shows a comparative study of the above two quantities (the ratio and the difference of R_{out} and R_{side}) for RHIC and LHC energies. They reflect a larger life time of thermal system for LHC than RHIC.

9. Elliptic Flow of Thermal Dileptons

It has been argued that the anisotropic momentum distribution of the hadrons can bring the information on the interaction of the dense phase of the system [142] despite the fact that the hadrons are emitted from the freezeout surfaces when the system is too dilute to support collectivity. Therefore, a suitable dynamical model is required to extrapolate the final hadronic spectra backward in time to get the information about the early dense phase. Such an extrapolation is not required for lepton pairs because they are emitted from the entire space-time volume of the system. Therefore, the v_2 of lepton pairs provides information of the hot and dense
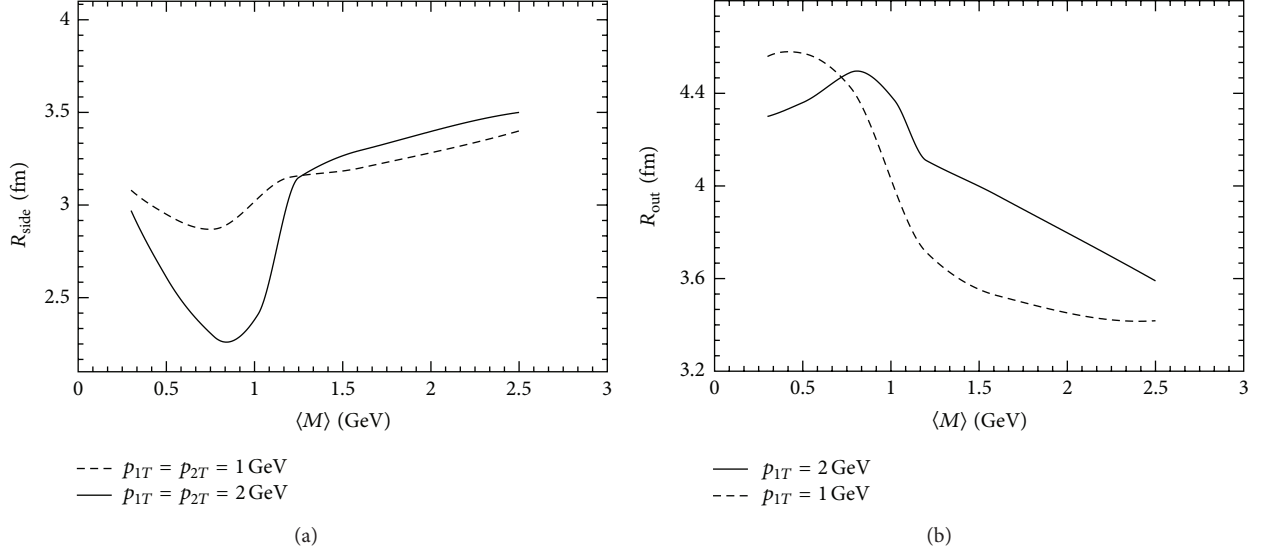
FIGURE 34: (a) Shows R_{side} as a function of $\langle M \rangle$ which is evaluated with $p_{1T} = p_{2T} = 1$ and 2 GeV and $\psi_2 = 0$ and similarly (b) shows R_{out} as a function of for $\psi_1 = \psi_2 = 0$ and $p_{1T} = 1$ and 2 GeV $\langle M \rangle$. The $p_{1T} = 1$ and 2 GeV results are shown as dashed line and solid line, respectively.
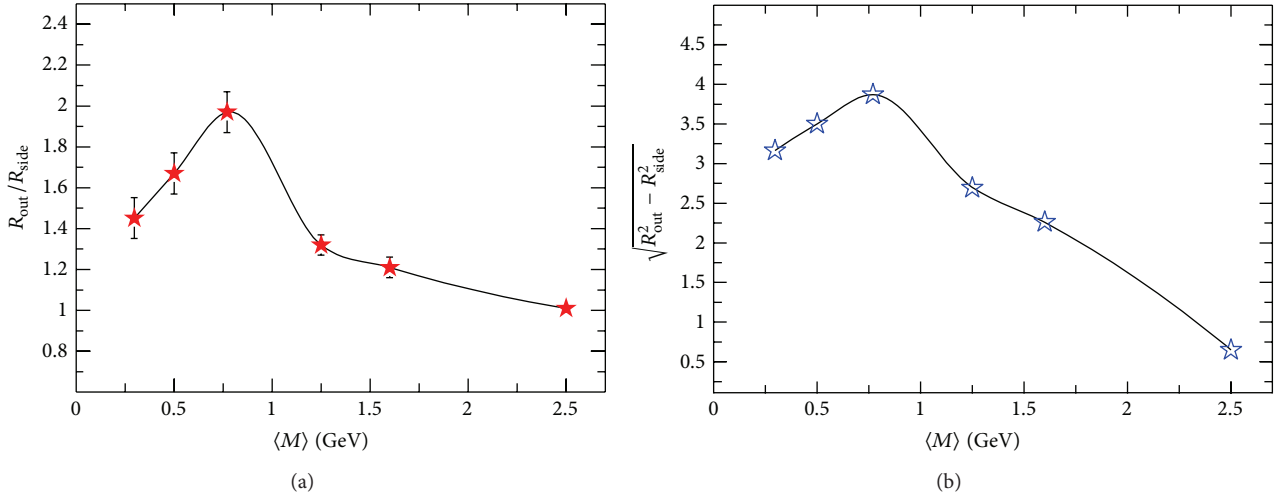

FIGURE 35: The ratio R_{out}/R_{side} and the difference $\sqrt{R_{out}^2 - R_{side}^2}$ as a function of $\langle M \rangle$ [14, 15].

phase directly. The v_2 of dileptons can also be used to to test the validity and efficiency of the extrapolation required for hadronic v_2. The v_2 of real photons and dileptons [128, 143–146] has been evaluated for RHIC energies and shown that it can be used as effective probes to extract the properties of the partonic plasma. The sensitivity of the v_2 of lepton pairs on EoS has been elaborated in [145] for RHIC collision conditions. The lepton pairs are produced from each space time point of the system and hence the study of v_2 of lepton pairs will shed light on the time evolution of collectivity in the system [12, 147]. The radial flow alters the shape of the p_T spectra of dileptons; it kicks the low p_T pairs to the higher p_T domain, making the spectra flatter. Therefore, the presence of large radial flow may diminish the magnitude of v_2 at low p_T [37, 38], and this effect will be larger when the radial flow

is large, that is, in the hadronic phase which corresponds to lepton pairs with $M \sim m_\rho$.

9.1. Formalism of Elliptic Flow of Dilepton. The elliptic flow of dilepton, v_2, can be defined as

$$v_2\left(p_T, M\right)$$

$$= \langle \cos 2\phi \rangle$$

$$= \frac{\sum_{i=Q,H} \int \cos\left(2\phi\right)\left(dN^{\gamma*}/d^2 p_T dM^2 dy\big|_{y=0}\right)_i d\phi}{\sum_{i=Q,H} \int \left(dN^{\gamma*}/d^2 p_T dM^2 dy\big|_{y=0}\right)_i d\phi},$$
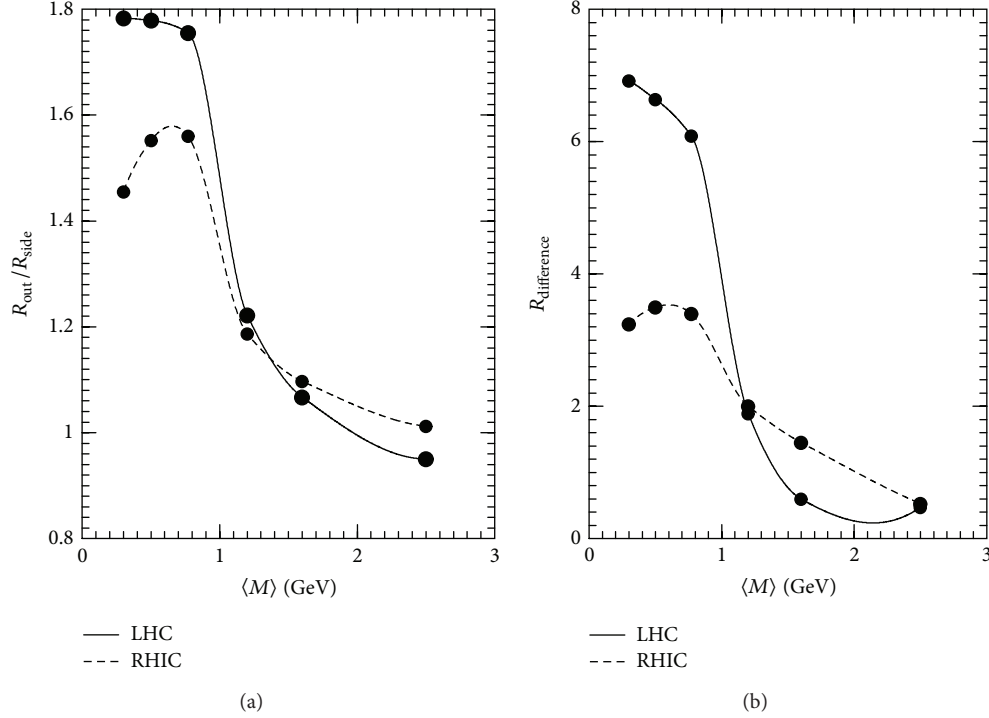
$$(82)$$

FIGURE 36: The ratio $R_{\text{out}}/R_{\text{side}}$ (a) and the difference $\sqrt{R_{\text{out}}^2 - R_{\text{side}}^2}$ (b) as a function of $\langle M \rangle$ for RHIC (dashed line) and LHC (solid line) energies are shown.

where the $\sum$ stands for summation over quark matter (QM) and hadronic matter (HM) phases. The quantity $dN/d^2 p_T dM^2 dy|_{y=0}$ appearing in (82) can be obtained from the dilepton production per unit four volume, $dN/d^4 p d^4 x$ in a thermalized medium by integrating over the space-time evolution of the system. The $dN/d^4 p d^4 x$ for lepton pairs for QGP and hadrons are discussed in Sections 6.1 and 6.2, respectively (see [13, 109] for details).

To evaluate v_2 from (82) one needs to integrate the fixed temperature production rate given by (9) over the space time evolution of the system—from the initial QGP phase to the final hadronic freezeout state through a phase transition in the intermediate stage. The space-time evolution is done over the 4-volume, which is defined as $d^4 x (= \tau d\tau dx dy d\eta)$ are expressed in terms of $x^\mu = (\tau, x, y, \eta)$. We assume that the matter is formed in QGP phase with zero net baryon density in Pb+Pb collision at $\sqrt{s_{NN}} = 2.76$ TeV. The energy of the lepton pair (p_0) should be replaced by its value in the comoving frame of the expanding system which is given by $[p \cdot u = \gamma_T (M_T \cosh(y - \eta) - v_x p_T \cos\phi - v_y p_T \sin\phi)]$, $p_\mu = (M_T \cosh y, p_T \cos\phi, p_T \sin\phi, M_T \sinh y)$, and $u^\mu = \gamma_T(\cosh\eta, v_x, v_y, \sinh\eta)$. The EoS required to close the hydrodynamic equations is constructed by complementing Wuppertal-Budapest lattice simulation [48] with a hadron resonance gas comprising all the hadronic resonances up to mass of 2.5 GeV [148, 149]. The necessary initial conditions to solve the hydrodynamic equations are $T_i = 456$ MeV, the value of the temperature corresponding to the maximum of the initial energy profile for 30–40%

centrality at $\sqrt{s_{NN}} = 2.76$ TeV, with $\tau_i = 0.6$ fm/c, the thermalization time. The transition temperature, T_c, for quark hadron conversion is taken as 175 MeV. The system is assumed to get out of chemical equilibrium at $T = T_{\text{ch}} = 170$ MeV [69]. The kinetic freezeout temperature $T_F = 130$ MeV is fixed from the p_T spectra of the produced hadrons at the same collision energy of Pb+Pb system. The EoS and the values of the parameters mentioned above are constrained by the p_T spectra (for 0–5% centrality) and elliptic flow (for 10–50% centrality) of charged hadrons [148] measured by ALICE collaboration [150, 151].

9.2. Results and Discussion. In Figure 37 we depict the constant temperature contours corresponding to $T_c = 175$ MeV and $T_f = 130$ MeV in the τ-x plane (at zero abscissa) indicating the boundaries for the QM and HM phases, respectively.

The life time of the QM phase ~6 fm/c and the duration of the HM are ~6–12 fm/c. Throughout this work by early and late will approximately mean the duration of the QM and HM, respectively.

With all the ingredients mentioned above we evaluate the p_T integrated M distribution of lepton pairs originating from QM and HM (with and without medium effects on the spectral functions of ρ and ω). The results are displayed in Figure 38 for the initial conditions and centrality mentioned above. We observe that for $M > M_\phi$ the QM contributions dominate. For $M_\rho \leq M \leq M_\phi$ the HM shines brighter than QM. For $M < M_\rho$, the HM (solid line) over shines
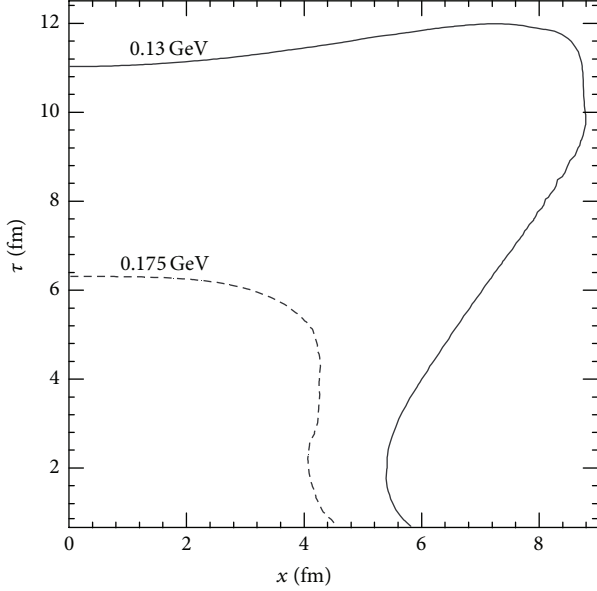
FIGURE 37: Constant temperature contours denoting space-time boundaries of the QGP and hadronic phase.

--- Quark matter
— Hadronic matter (medium)
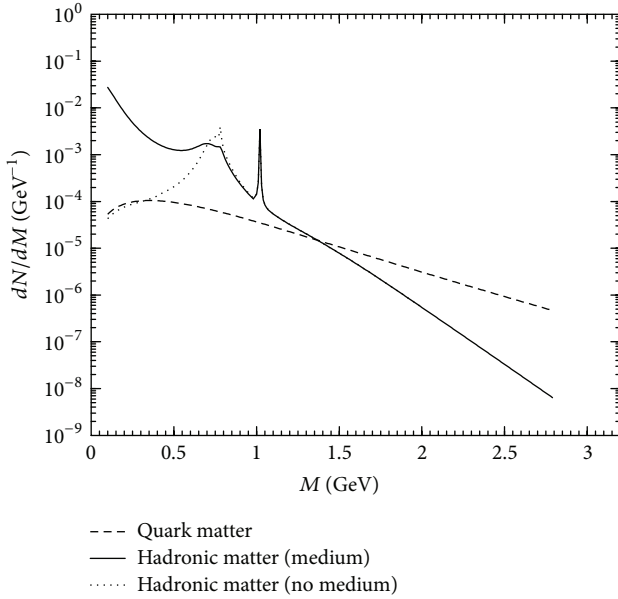⋯⋯ Hadronic matter (no medium)

FIGURE 38: Invariant mass distribution of lepton pairs from quark matter and hadronic matter [13].

the QM due to the enhanced contributions primarily from the medium-induced broadening of ρ spectral function. However, the contributions from QM and HM become comparable in this region of M if the medium effects on ρ spectral function are ignored (dotted line). Therefore, the results depicted in Figure 38 indicate that a suitable choice of M window will enable us to unravel the contributions from a particular phase (QM or HM).

- - - $\langle M \rangle = 0.3$ GeV (no medium)   —— $\langle M \rangle = 1.02$ GeV
—— $\langle M \rangle = 0.3$ GeV   —·— $\langle M \rangle = 2.5$ GeV
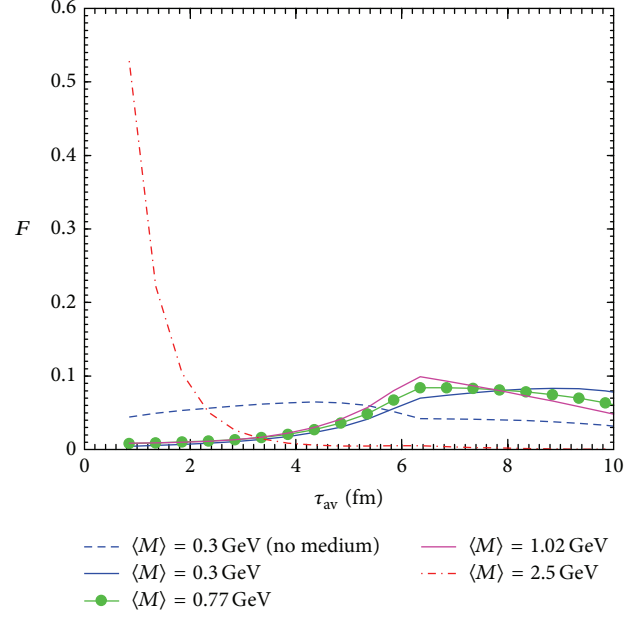—●— $\langle M \rangle = 0.77$ GeV

FIGURE 39: Fractional contribution of lepton pairs for various invariant mass windows as a function of average proper time (see text for details) [13].
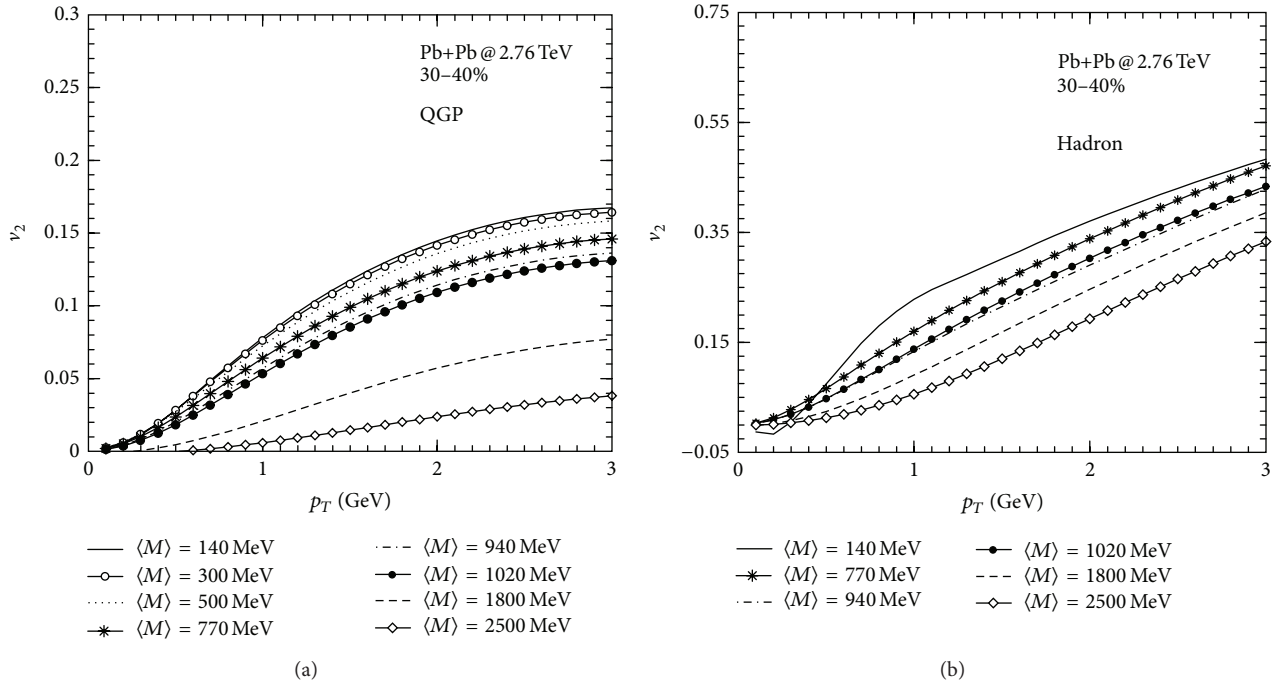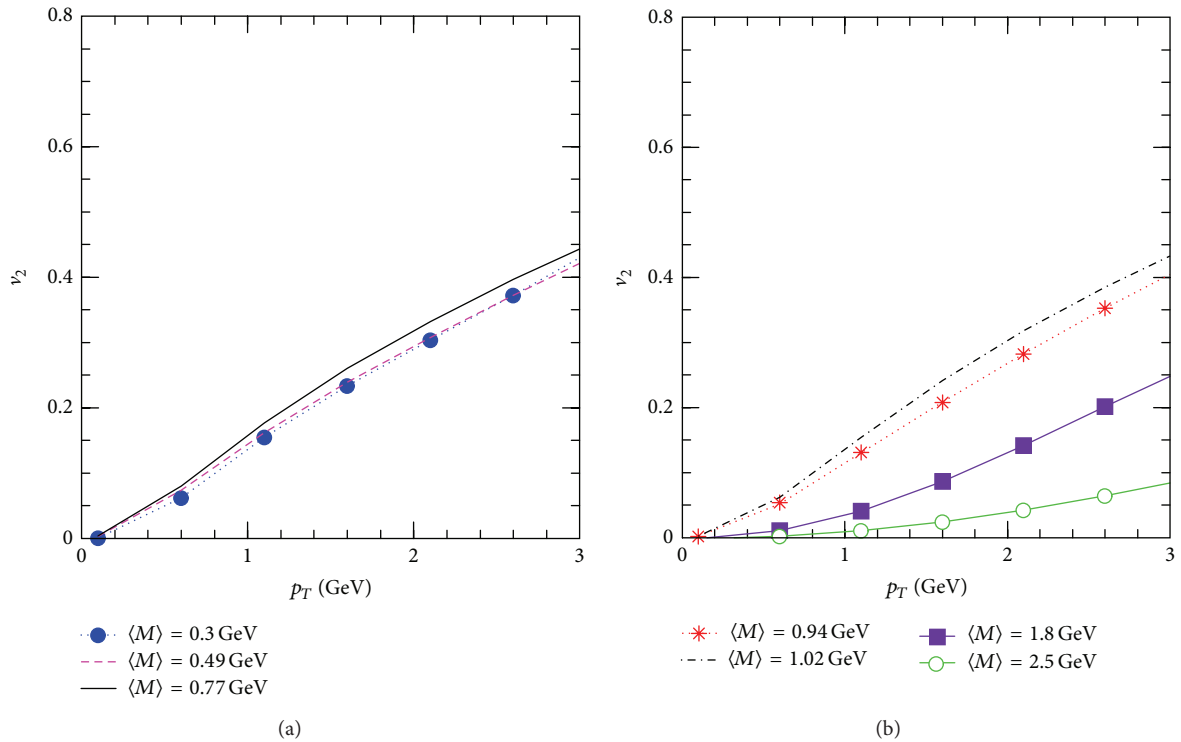
To further quantify these issues we evaluate the following quantity:

$$F = \frac{\int' \left(dN/d^4x d^2 p_T dM^2 dy \right) dx dy d\eta d\tau d\tau d^2 p_T dM^2}{\int \left(dN/d^4x d^2 p_T dM^2 dy \right) dx dy d\eta d\tau d\tau d^2 p_T dM^2}, \quad (83)$$

where the M integration in both the numerator and denominator is performed for selective M windows from M_1 to M_2 with mean M defined as $\langle M \rangle = (M_1 + M_2)/2$. The prime in $\int'$ in the numerator indicates that the τ integration in the numerator is done from $\tau_1 = \tau_i$ to $\tau_2 = \tau_i + \Delta\tau$ with progressive increment of $\Delta\tau$, while in the denominator the integration is done over the entire lifetime of the system. In Figure 39, F is plotted against $\tau_{av} (= (\tau_1 + \tau_2)/2)$. The results substantiate the fact that pairs with high $\langle M \rangle \sim 2.5$ GeV originate from QM ($\tau_{av} \leq 6$ fm/c, QGP phase) and pairs with $\langle M \rangle \sim 0.77$ GeV mostly emanate from the HM phase ($\tau_{av} \geq 6$ fm/c). The change in the properties of ρ due to its interaction with thermal hadrons in the bath is also visible through F evaluated for $\langle M \rangle \sim 0.3$ GeV with and without medium effects. This clearly indicates that the $\langle M \rangle$ distribution of lepton pairs can be exploited to extract collectivity of different phases of the evolving matter.

Figure 40(a) shows the differential elliptic flow, $v_2(p_T)$, of dileptons arising from various $\langle M \rangle$ domains in quark matter. Similarly Figure 40(b) shows the differential elliptic flow, $v_2(p_T)$, of dileptons arising from various $\langle M \rangle$ domains from hadronic matter. The individual v_2 for QM and HM is obtained by doing an integration over specific invariant masses (M) window as well as space time integration over the regime where $T_c < T(\tau, x, y) < T_i$ and $T_f < T(\tau, x, y) < T_c$, respectively. The v_2 is small at low p_T and gradually increases

FIGURE 40: Elliptic flow of quark matter (a) and hadronic matter (b) as a function of p_T for various mass windows.

FIGURE 41: Total elliptic flow as function of p_T for various mass windows.

and attains large value around $p_T \sim$ 2-3 GeV/c. Also there is clear mass ordering that has been observed for $v_2(p_T)$ for QM; that is, v_2 decreases with increase in M. This is because dileptons come from high M region, $M > M_\phi$, come mostly from hot partonic phase where the fluid velocity is not strong to support the collectivity but the spatial eccentricity of the source is large. On the other hand dileptons that come from low M region, M below ϕ peak dominantly come from late hadronic matter where the collectivity is strong and the spatial asymmetry dissolve into momentum asymmetry.

Figure 41 shows the differential elliptic flow, $v_2(p_T)$ of dileptons arising from various $\langle M \rangle$ domains. We observe

that, for $\langle M \rangle$ = 2.5 GeV, v_2 is small for the entire p_T range because these pairs arise from the early epoch (see Figure 39) when the flow is not developed entirely. However, the v_2 is large for $\langle M \rangle$ = 0.77 GeV as these pairs originate predominantly from the late hadronic phase when the flow is fully developed.

It is also interesting to note that the medium-induced enhancement of ρ spectral function provides a visible modification in v_2 for dileptons below ρ peak. **Figure 42** shows the comparison between $v_2(p_T)$ of dilepton at $\langle M \rangle$ = 300 MeV with and without medium effects.

In **Figure 43** we depict the variation of R_Q with p_T for $\langle M \rangle$ = 0.3 GeV (line with solid circle) 0.77 GeV (solid line) and 2.5 GeV (line with open circle). The quantity R_Q and R_H is defined as

$$R_Q = \frac{v_2^{QM}}{v_2^{QM} + v_2^{HM}},$$

$$R_H = \frac{v_2^{HM}}{v_2^{QM} + v_2^{HM}}, \tag{84}$$

where v_2^{QM} and v_2^{HM} are the elliptic flow of QM and HM phases, respectively. The results clearly illustrate that v_2 of lepton pairs in the large $\langle M \rangle (= 2.5$ GeV) domain (open circle in **Figure 43**) originates from QM for the entire p_T range considered here. The value of R_Q is large in this domain because of the large (negligibly small) contributions from QM (HM) phase. f_{QM} is large here. It is also clear that the contribution from QM phase to the elliptic flow for $\langle M \rangle (= 0.77$ GeV$)$ is very small (solid line in **Figure 43**). The value of R_H for $\langle M \rangle$ = 0.77 GeV is large (not shown in the figure). The v_2 at the (late) hadronic phase (either at ρ or ϕ peak) is larger than the (early) QGP phase (say at $\langle M \rangle$ = 2.5 GeV) for the entire p_T range considered here. Therefore, the p_T-integrated values of v_2 should also retain this character of v_2 at the corresponding values of $\langle M \rangle$. It is also important to note that the differential elliptic flow, $v_2(p_T)$, obtained here at LHC is larger than the values obtained at RHIC [143–145] for all the invariant mass windows. The value of R_H for $\langle M \rangle$ = 0.77 GeV is large (not shown in the figure).

The v_2 at the HM phase (either at ρ or ϕ peak) is larger than its value in the QGP phase (say at $\langle M \rangle$ = 2.5 GeV) for the entire p_T-range considered here. Therefore, the p_T integrated values of v_2 should also retain this character at the corresponding values of $\langle M \rangle$, which is clearly observed in **Figure 44** which displays the variation of $v_2(\langle M \rangle)$ with $\langle M \rangle$. The $v_2(\propto \epsilon_p)$ of QM is small because of the small pressure gradient in the QGP phase. The v_2 resulting from hadronic phase has a peak around ρ pole indicating the full development of the flow in the HM phase. For $\langle M \rangle > m_\phi$ the v_2 obtained from the combined phases approachs the value corresponding to the v_2 for QGP. Therefore, measurement of v_2 for large $\langle M \rangle$ will bring information of the QGP phase at the earliest time of the evolution. It is important to note that the p_T-integrated $v_2(\langle M \rangle)$ of lepton pairs with $\langle M \rangle \sim m_\pi, m_K$ is close to the hadronic v_2^π and v_2^K (symbol ∗ in **Figure 44**) if the thermal effects on ρ properties are included. Exclusion of

FIGURE 42: The figure displays the effect of the broadening of ρ spectral function on the elliptic flow for $\langle M \rangle$ = 300 MeV.

FIGURE 43: It shows the variation of R_Q (see text) with p_T for $\langle M \rangle$ = 0.3 GeV, 0.77 GeV and 2.5 GeV.

medium effects gives lower v_2 for lepton pairs compared to hadrons. The fact that the v_2 of the (penetrating) lepton pairs is similar in magnitude to the v_2 of hadrons for ($\langle M \rangle \sim m_\pi$, m_K, m_{proton}, etc.) ascertains that the anisotropic momentum distribution of hadrons carries the information of the HM phase with duration ~6–12 fm/c [13]. We also observe that the variation of $v_2(\langle M \rangle)$ with $\langle M \rangle$ has a structure similar to dN/dM versus M. As indicated by (82) we can write

FIGURE 44: (Color online) Variation of dilepton elliptic flow as function of $\langle M \rangle$ for QM, HM (with and without medium effects), and for the entire evolution. The symbol $*$ indicates the value of v_2 for hadrons, for example, π, kaon, proton, and ϕ.

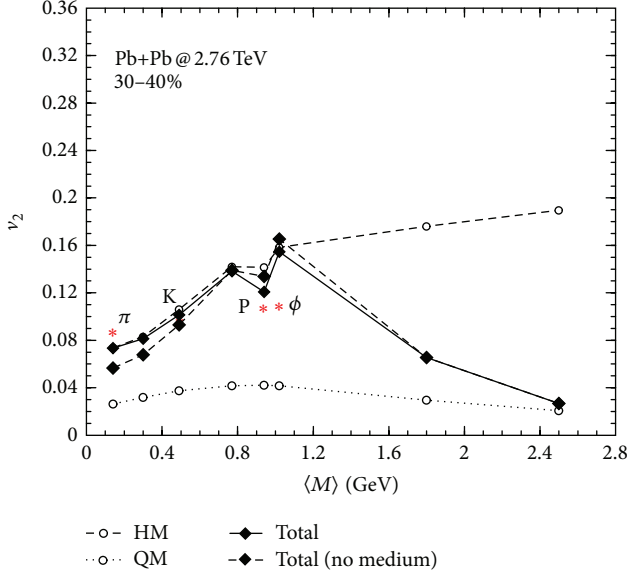$v_2(\langle M \rangle) \sim \sum_{i=\text{QM,HM}} v_2^i \times f_i$, where f_i is the fraction of QM or HM from various space-time regions. The structure of dN/dM is reflected in $v_2(\langle M \rangle)$ through f_i. We find that the magnitude of $v_2(\langle M \rangle)$ at LHC is larger than its value at RHIC [143–145].

10. Summary

In this review, we have attempted to summarize the photon and dilepton spectra measured at different beam energies by different experimental collaborations which have been analyzed to understand the evaluation of collectivity in the system. The initial conditions of the evolving matter required to calculate the photon and dilepton spectra have been constrained to reproduce the measured multiplicity in these collisions. The EoS, the other crucial input to the calculations, has been taken from lattice QCD calculations. The deviation of the hadronic phase from chemical equilibrium is taken into account by introducing nonzero chemical potential for each hadronic species. For dilepton emission from hot hadrons, the spectral function of ρ, ω at finite temperature and ϕ in vacuum is considered. We have also observed the dissipative effects on the photon spectra by taking into account the viscous contribution to phase space factors of all the participating partons/hadrons in the photon production rate as well as to the expansion dynamics with finite shear viscosity.

It is shown that simultaneous measurements of photon and dilepton spectra in heavy ion collisions will enable us to quantify the evolution of the average radial flow velocity for the system, and the nature of the variation of radial flow with invariant mass will indicate the formation of partonic phase. All this study suggests with judicious choice of p_T and

M window will infer information of partonic and hadronic phase separately.

In this work, we present a new proposal for carrying out an experimental measurement of dilepton interferometry both for RHIC and LHC. We establish through a hydrodynamical model-based space-time evolution the promise of such a dilepton interferometry analysis that will be useful to understand the properties of the partonic phase. We have evaluated the correlation function, C_2, for two dilepton pairs for various invariant mass domains and extracted the HBT radii, that is R_{side} and R_{out} as a function of M. These HBT radii show a nonmonotonic dependence on the invariant mass, reflecting the evolution of collective flow in the system which can be considered as a signal of the QGP formation in heavy ion collisions. The M dependence of the $R_{\text{out}}/R_{\text{side}}$ and $\sqrt{R_{\text{out}}^2 - R_{\text{side}}^2}$ which can be experimentally measured could be used to characterize the source properties at various instances of the evolution.

We have evaluated the v_2 of dileptons originating from the Pb+Pb collisions at $\sqrt{s_{NN}} = 2.76$ TeV for 30–40% centrality. Our study shows that $v_2(M)$ provides useful information on the collective motion of the evolving QCD matter formed in high energy heavy-ion collisions. The present work indicates that experimental observation of the reduction of $v_2(M)$ with increasing M beyond ϕ mass would reflect the presence of small momentum space anisotropy through small collective motion in the partonic phase. We observe that $v_2(\langle M \rangle)$ of the penetrating probe (lepton pairs) for $\langle M \rangle = m_\pi$ and m_K is similar to the hadronic v_2^π and v_2^K when the medium-induced change in the ρ spectral function is included in evaluating the dilepton spectra. Since the medium effects are large during the dense phase of the system, therefore, this validates the statement that the hadronic v_2 carries the information of the early dense phase of the collisions. Our study also establishes the fact that the invariant mass dependence of dilepton v_2 can in principle act as a clock for the space time evolution of the system formed in HIC.

Some comments on effect of magnetic field on photon and dilepton production are in order here. The magnetic contribution is significant when photons propagate perpendicular to magnetic field or in reaction plane in noncentral collision [152]. Recently, Tuchin has implemented the magnetic field effect on the photon as well as dilepton production which is summarized here. Recently in [153, 154], it has been argued that photons, in particular thermal and direct photons from earliest times of QGP, will be affected by the magnetic field. In dilepton sector, the magnetic contribution is important at lower electron energies (below ~0.5 GeV at midrapidity at RHIC). In fact, it becomes dominant source of dileptons at lower electron energies. For LHC energies, the effect of magnetic field on dilepton should be taken seriously because 40% of energy density of the QGP resides in the strong magnetic field (~10^{18} Gauss [152]), which can be generated in heavy ion collision at LHC. Whereas in RHIC energy this fraction is within 3% so can be safely ignored. Some more realistic calculation and hydrodynamic model with magnetic field are required to conclude anything in future.

Appendix

Phase Space

In this appendix we derive (37) from (12). The photon production rate from the process, $1 + 2 \rightarrow 3 + \gamma$ is given by

$$
\begin{aligned}
E\frac{dR}{d^3p} &= \frac{1}{2}\frac{\mathcal{N}}{(2\pi)^8} \\
&\times \int \frac{d^3p_1}{2E_1} \int \frac{d^3p_2}{2E_2} \int \frac{d^3p_3}{2E_1} f_1(E_1) f_2(E_2) \\
&\times [1 \pm f_3(E_3)]\overline{|M|^2}\delta \\
&\times (p_1 + p_2 - p_3 - p).
\end{aligned}
\tag{A.1}
$$

Performing the d^3p_3 integration using the delta function and using $d^3p/E = p_T dp_T dy d\phi$ we get

$$
\begin{aligned}
E\frac{dR}{d^3p} &= \frac{1}{16}\frac{\mathcal{N}}{(2\pi)^8} \int p_{1T} dp_{1T} dy_1 d\phi_1 p_{2T} dp_{2T} dy_2 d\phi_2 \\
&\times \frac{1}{E_3} f_1(E_1) f_2(E_2)[1 \pm f_3(E_3)] \\
&\times \overline{|M|^2}\delta(E_1 + E_2 - E_3 - E),
\end{aligned}
\tag{A.2}
$$

where ϕ_1 and ϕ_2 are the angles made by the transverse momenta of first and second particles with the transverse momentum of the emitted photon. The momentum conservation along the z-direction: $p_{3z} = p_{1z} + p_{2z} - p_z$ can be written in terms of rapidity as

$$
m_{3T}\sinh y_3 = m_{1T}\sinh y_1 + m_{2T}\sinh y_2 - p_T \sinh y.
\tag{A.3}
$$

Now the energy, E_3, can be written as

$$
E_3 = m_{3T}\cosh y_3 = \sqrt{m_{3T}^2 + m_{3T}^2 \sinh^2 y_3}.
\tag{A.4}
$$

Substituting (A.3) in (A.4) we get

$$
E_3 = \left[(m_{1T}\sinh y_1 + m_{2T}\sinh y_2 - p_T \sinh y)^2 + m_{3T}^2\right]^{1/2}.
\tag{A.5}
$$

Considering the energy conservation ($E_3 = E_1 + E_2 - E$) and writing the energies in terms of rapidity ($E_i = m_{iT}\cosh y_i$) we get

$$
E_3 = m_{1T}\cosh y_1 + m_{2T}\cosh y_2 - p_T \cosh y.
\tag{A.6}
$$

Equating (A.5) and (A.6) we have

$$
\begin{aligned}
m_{3T} = \big[& m_{1T}^2 + m_{2T}^2 + p_T^2 + 2m_{1T}m_{2T}\cosh(y_1 - y_2) \\
& -2m_{1T}p_T \cosh(y_1 - y) - 2m_{2T}p_T \cosh(y_2 - y)\big]^{1/2}.
\end{aligned}
\tag{A.7}
$$

However, we also have

$$
\begin{aligned}
m_{3T} &= \left(p_{3T}^2 + m_3^2\right)^{1/2} \\
&= \left[(p_{1T} + p_{2T} - p_T)^2 + m_3^2\right]^{1/2} \\
&= \big[p_{1T}^2 + p_{2T}^2 + p_T^2 + 2p_{1T}p_{2T}\cos(\phi_{12}) \\
&\quad -2p_T p_{1T}\cos(\phi_1) - 2p_T p_{2T}\cos(\phi_2) + m_3^2\big]^{1/2},
\end{aligned}
\tag{A.8}
$$

where

$$
\cos(\phi_{12}) = \cos(\phi_1)\cos(\phi_2) + \sin(\phi_1)\sin(\phi_2).
\tag{A.9}
$$

Equating (A.7) with (A.8) leads to the expression:

$$
\begin{aligned}
\big[(p_{1T}&\cos\phi_1 - p_T)\cos\phi_2 + p_{1T}\sin\phi_1 \sin\phi_2\big] \\
&= \frac{1}{2p_{2T}}\big[(m_1^2 + m_2^2 - m_3^2) + 2m_{1T}m_{2T}\cosh(y_1 - y_2) \\
&\quad - 2m_{1T}p_T \cosh(y_1 - y) - 2m_{2T}p_T \cosh(y_2 - y) \\
&\quad + 2p_T p_{1T}\cos\phi_1\big].
\end{aligned}
\tag{A.10}
$$

Solving (A.10) for ϕ_2 one gets

$$
\phi_2^0 = \tan^{-1}\left(\frac{p_{1T}\sin\phi_1}{p_{1T}\cos\phi_1 - p_T}\right) - \cos^{-1}\frac{H}{2Rp_{2T}},
\tag{A.11}
$$

where

$$
R = \sqrt{p_{1T}^2 + p_T^2 - 2p_{1T}p_T \cos\phi_1},
\tag{A.12}
$$

$$
\begin{aligned}
H = \ & (m_1^2 + m_2^2 - m_3^2) + 2m_{1T}m_{2T}\cosh(y_1 - y_2) \\
& - 2m_{1T}p_T \cosh(y_1 - y) - 2m_{2T}p_T \cosh(y_2 - y) \\
& + 2p_T p_{1T}\cos\phi_1.
\end{aligned}
\tag{A.13}
$$

Now we express the argument of the delta function in (A.2) as function of ϕ_2 as

$$
\begin{aligned}
f(\phi_2) &= E_1 + E_2 - E_3 - E \\
&= m_{1T}\cosh y_1 + m_{2T}\cosh y_2 - p_T \cosh y \\
&\quad - \left[m_{3T}^2 + (m_{1T}\sinh y_1 + m_{2T}\sinh y_2 - p_T \sinh y)^2\right]^{1/2},
\end{aligned}
\tag{A.14}
$$

and performing the ϕ_2 integration in (A.2) we get

$$
\begin{aligned}
E\frac{dR}{d^3p} = {} & \frac{1}{16}\frac{\mathcal{N}}{(2\pi)^8}\int_0^\infty p_{1T}dp_{1T}\int_0^\infty dp_{2T} \\
& \times \int_{-\infty}^\infty dy_1 \int_{-\infty}^\infty dy_2 \int_0^{2\pi} d\phi_1 \\
& \times f_1(E_1)f_2(E_2)\left[1 \pm f_3(E_3)\right] \\
& \times \frac{\overline{|M|^2}}{\left|p_{1T}\sin(\phi_1-\phi_2)+p_T\sin\phi_2\right|_{\phi_2^0}}
\end{aligned}
\tag{A.15}
$$

with the constraint $|H/2Rp_{2T}| \leq 1$ originating from $|\cos(\phi)| \leq 1$.

Acknowledgments

References

[1] L. D. McLerran and T. Toimela, "Photon and dilepton emission from the quark-gluon plasma: some general considerations," *Physical Review D*, vol. 31, pp. 545–563, 1985.

[2] C. Gale and J. Kapusta, "Dilepton radiation from high temperature nuclear matter," *Physical Review C*, vol. 35, no. 6, pp. 2107–2116, 1987.

[3] C. Gale and J. I. Kapusta, "Vector dominance model at finite temperature," *Nuclear Physics B*, vol. 357, no. 1, pp. 65–89, 1991.

[4] H. A. Weldon, "Reformulation of finite-temperature dilepton production," *Physical Review D*, vol. 42, pp. 2384–2387, 1990.

[5] R. Rapp and J. Wambach, "Chiral symmetry restoration and dileptons in relativistic heavy-ion collisions," *Advances in Nuclear Physics*, vol. 25, pp. 1–205, 2000.

[6] "Elementary particles, nuclei and atoms," *Relativistic Heavy Ion Physics*, vol. 23, pp. 134–175, 2010.

[7] J.-E. Alam, S. Raha, and B. Sinha, "Electromagnetic probes of quark gluon plasma," *Physics Reports*, vol. 273, no. 5–6, pp. 243–362, 1996.

[8] J.-E. Alam, S. Sarkar, P. Roy, T. Hatsuda, and B. Sinha, "Thermal photons and Lepton pairs from Quark Gluon plasma and hot hadronic matter," *Annals of Physics*, vol. 286, no. 2, pp. 159–248, 2000.

[9] R. Chatterjee, L. Bhattacharya, and D. K. Shrivastava, "Electromagnetic probes," *Lecture Notes in Physics*, vol. 785, pp. 219–264, 2010.

[10] H. van Hees and R. Rapp, "Dilepton radiation at the CERN super-proton synchrotron," *Nuclear Physics A*, vol. 806, no. 1–4, pp. 339–387, 2008.

[11] R. Rapp, "Theory of soft electromagnetic emission in heavy-ion collisions," *Acta Physica Polonica B*, vol. 42, no. 12, p. 2823, 2011.

[12] P. Mohanty, J. K. Nayak, J.-E. Alam, and S. K. Das, "Radial flow from electromagnetic probes and signal of quark gluon plasma," *Physical Review C*, vol. 82, no. 3, Article ID 034901, 2010.

[13] P. Mohanty, V. Roy, S. Ghosh, S. K. Das, B. Mohanty et al., "Elliptic flow of thermal dileptons as a probe of QCD matter," *Physical Review C*, vol. 85, Article ID 031903, 2012.

[14] P. Mohanty, J.-E. Alam, and B. Mohanty, "Evolution of collectivity as a signal of quark gluon plasma formation in heavy ion collisions," *Physical Review C*, vol. 84, no. 2, Article ID 024903, 2011.

[15] P. Mohanty, J.-E. Alam, and B. Mohanty, "Characterizing quark gluon plasma by dilepton interferometry," *Nuclear Physics A*, vol. 862, pp. 301–303, 2011.

[16] J. K. Nayak, J.-E. Alam, S. Sarkar, and B. Sinha, "Thermal photon to dilepton ratio in high energy nuclear collisions," *Physical Review C*, vol. 78, no. 3, Article ID 034903, 2008.

[17] J. I. Kapusta and E. V. Shuryak, "Weinberg-type sum rules at zero and finite temperature," *Physical Review D*, vol. 49, pp. 4694–4704, 1994.

[18] C. Y. Wong, *Introduction of High Energy Heavy Ion Collisions*, World Scientific, Singapore, 1994.

[19] J.-E. Alam, D. K. Srivastava, B. Sinha, and D. N. Basu, "Transverse flow effects on high-energy photons emitted by expanding quark-gluon plasma," *Physical Review D*, vol. 48, pp. 1117–1131, 1993.

[20] J. Ruppert, C. Gale, T. Renk, P. Lichard, and J. I. Kapusta, "Low mass dimuons produced in relativistic nuclear collisions," *Physical Review Letters*, vol. 100, Article ID 162301, 2008.

[21] S. D. Drell and T.-M. Yan, "Massive lepton-pair production in hadron-hadron collisions at high energies," *Physical Review Letters*, vol. 25, no. 5, pp. 316–320, 1970.

[22] S. D. Drell and T. M. Yan, "Massive Lepton-pair production in Hadron-Hadron collisions at high energies," *Physical Review Letters*, vol. 25, p. 902, 1970.

[23] S. Gavin, P. L. McGaughey, P. V. Ruuskanen, and R. Vogt, "Lepton production from charm decay in nuclear collisions at $\sqrt{s} = 200$ GeV and 5.5 TeV per nucleon," *Physical Review C*, vol. 54, no. 5, pp. 2606–2623, 1996.

[24] N. Armesto, N. Borghini, S. Jeon, U. A. Wiedemann et al., "Heavy-ion collisions at the LHC-Last call for predictions," *Journal of Physics G*, vol. 35, Article ID 054001, 2008.

[25] R. Rapp, "Duality and chiral restoration from low-mass dileptons at the CERN-SpS," *Nuclear Physics A*, vol. 661, no. 1–4, Article ID 990734, pp. 33–44, 1999.

[26] R. Rapp and J. Wambach, "Low-mass dileptons at the CERN-SpS: evidence for chiral restoration?" *The European Physical Journal A*, vol. 6, pp. 415–420, 1999.

[27] E. L. Feinberg, "Direct production of photons and dileptons in thermodynamic models of multiple hadron production," *Nuovo Cimento A*, vol. 34, pp. 391–412, 1976.

[28] S. Sarkar, "Photons from ultra-relativistic heavy ion collisions," http://arxiv.org/abs/nucl-th/0007011.

[29] A. Das, *Finite Temperature Field Theory*, World Scientific, Singapore, 1997.

[30] R. Kobes and G. Semenoff, "Discontinuities of green functions in field theory at finite temperature and density," *Nuclear Physics B*, vol. 260, no. 3–4, pp. 714–746, 1985.

[31] R. Kobes and G. Semenoff, "Discontinuities of green functions in field theory at finite temperature and density (II)," *Nuclear Physics B*, vol. 272, no. 2, pp. 329–364, 1986.

[32] F. Gelis, "Cutting rules in the real-time formalisms at finite temperature," *Nuclear Physics B*, vol. 508, no. 1-2, pp. 483–505, 1997.

[33] S. Sarkar, J.-E. Alam, P. Roy, A. K. Dutt-Mazumder, B. Dutta-Roy, and B. Sinha, "Photons from hadronic matter at finite temperature," *Nuclear Physics A*, vol. 634, no. 1–2, pp. 206–230, 1998.

[34] T. Hirano and Y. Nara, "Hydrodynamic afterburner for the color glass condensate and the parton energy loss," *Nuclear Physics A*, vol. 743, no. 4, pp. 305–328, 2004.

[35] D. Teaney, J. Lauret, and E. V. Shuryak, "Flow at the SPS and RHIC as a Quark-Gluon plasma signature," *Physical Review Letters*, vol. 86, pp. 4783–4786, 2001.

[36] P. F. Kolb, P. Huovinen, U. W. Heinz, and H. Heiselberg, "Elliptic flow at SPS and RHIC: from kinetic transport to hydrodynamics," *Physics Letters B*, vol. 500, no. 3–4, pp. 232–240, 2001.

[37] P. Huovinen, P. F. Kolb, U. Heinz, P. V. Ruuskanen, and S. A. Voloshin, "Radial and elliptic flow at RHIC: further predictions," *Physics Letters, Section B*, vol. 503, no. 1-2, pp. 58–64, 2001.

[38] T. Hirano and M. Gyulassy, "Perfect fluidity of the quark-gluon plasma core as seen through its dissipative hadronic corona," *Nuclear Physics A*, vol. 769, no. 1–4, pp. 71–94, 2006.

[39] C. Nokana and S. A. Bass, "Space-time evolution of bulk QCD matter," *Physical Review C*, vol. 75, Article ID 014902, 2007.

[40] L. D. Landau, "On the multiple production of particles in high energy collisions," *Izvestiya Akademii Nauk Azerbaidzhanskoi SSR. Seriya Fiziko-Tekhnicheskikh*, vol. 17, p. 51, 1953.

[41] J. D. Bjorken, "Highly relativistic nucleus-nucleus collisions: the central rapidity region," *Physical Review D*, vol. 27, no. 1, pp. 140–151, 1983.

[42] T. Hirano, N. van der Kolk, and A. Bilandzic, "Hydrodynamics and flow," *Lecture Notes in Physics*, vol. 785, pp. 139–178, 2010.

[43] J.-Y. Ollitrault, "Relativistic hydrodynamics for heavy-ion collisions," *European Journal of Physics*, vol. 29, no. 2, pp. 275–302, 2008.

[44] S. Weinberg, "Entropy generation and the survival of proto-galaxies in an expanding universe," *The Astronomical Journal*, vol. 168, pp. 175–194, 1971.

[45] P. Danielewich and m. Gyulassy, "Dissipative phenomena in quark-gluon plasmas," *Physical Review D*, vol. 31, pp. 53–62, 1985.

[46] R. C. Hwa and K. Kajantie, "Diagnosing quark matter by measuring the total entropy and the photon or dilepton emission rates," *Physical Review D*, vol. 32, pp. 1109–1118, 1985.

[47] D. Kharzeev and M. Nardi, "Hadron production in nuclear collisions at RHIC and high-density QCD," *Physics Letters B*, vol. 507, no. 1–4, pp. 121–128, 2001.

[48] S. Borsanyi, G. Endrodi, Z. Fodor, A. Jakovac et al., "The QCD equation of state with dynamical quarks," *Journal of High Energy Physics*, vol. 1011, p. 077, 2010.

[49] F. Cooper and G. Frye, "Single-particle distribution in the hydrodynamic and statistical thermodynamic models of multiparticle production," *Physical Review D*, vol. 10, no. 1, pp. 186–189, 1974.

[50] R. Bair, H. Nakkagawa, A. Niegawa, and K. Redlich, "Production rate of hard thermal photons and screening of quark mass singularity," *Zeitschrift für Physik C Particles and Fields*, vol. 53, no. 3, pp. 433–438, 1992.

[51] E. Braaten and R. D. Pisarski, "Soft amplitudes in hot gauge theories: a general analysis," *Nuclear Physics B*, vol. 337, no. 3, pp. 569–634, 1990.

[52] E. Braaten and R. D. Pisarski, "Deducing hard thermal loops from Ward identities," *Nuclear Physics B*, vol. 339, no. 2, pp. 310–324, 1990.

[53] P. Aurenche, F. Gelis, R. Kobes, and H. Zaraket, "Bremsstrahlung and photon production in thermal QCD," *Physical Review D*, vol. 58, Article ID 085003, 1998.

[54] P. Arnold, G. D. Moore, and L. G. Yaffe, "Photon emission from ultrarelativistic plasmas," *Journal of High Energy Physics*, vol. 0111, Article ID 057, 2001.

[55] P. Arnold, G. D. Moore, and L. G. Yaffe, "Photon emission from Quark-Gluon plasma: complete leading order results," *Journal of High Energy Physics*, vol. 0112, Article ID 009, 2001.

[56] O. Kaczmarek and F. Zantow, "Static quark-antiquark interactions in zero and finite temperature QCD: I. Heavy quark free energies, running coupling, and quarkonium binding," *Physical Review D*, vol. 71, Article ID 114510, 2005.

[57] P. Roy, S. Sarkar, J.-E. Alam, and B. Sinha, "Electromagnetic radiation from hot and dense hadronic matter," *Nuclear Physics A*, vol. 653, no. 3, pp. 277–300, 1999.

[58] J.-E. Alam, P. Roy, and S. Sarkar, "Comment on "Hadronic production of thermal photons"," *Physical Review C*, vol. 71, Article ID 059802, 2005.

[59] S. Mitra, P. Mohanty, S. Ghosh, S. Sarkar, and J.-E. Alam, "Characterizing quark gluon plasma by thermal photons and lepton pairs," http://arxiv.org/abs/1303.0675.

[60] J. J. Sakurai, *Currents and Mesons*, The University of Chicago Press, Chicago, Ill, USA, 1969.

[61] R. K. Bhaduri, *Models of Nucleon—From Quarks to Soliton*, Addison-Wesley, 1988.

[62] S. Turbide, R. Rapp, and C. Gale, "Hadronic production of thermal photons," *Physical Review C*, vol. 69, no. 1, Article ID 014903, 2004.

[63] K. L. Haglin, "Photon production from hot hadronic matter," *Journal of Physics G*, vol. 30, p. L27, 2004.

[64] H. Von Gersdorff, L. D. McLerran, M. Kataja, and P. V. Ruuskanen, "Studies of the hydrodynamic evolution of matter produced in fluctuations in $p\bar{p}$ collisions and in ultrarelativistic nuclear collisions," *Physical Review D*, vol. 34, pp. 794–810, 1986.

[65] M. M. Aggarwal, A. Agnihotri, Z. Ahammed, WA98 Collaboration et al., "Observation of direct photons in central 158A GeV ^{208}P^{208}b+Pb collisions," *Physical Review Letters*, vol. 85, pp. 3595–3599, 2000.

[66] C. Bernard, T. Burch, C. DeTar et al., "QCD equation of state with 2+1 flavors of improved staggered quarks," *Physical Review D*, vol. 75, Article ID 094505, 2007.

[67] I. Arsene, I. G. Bearden, D. Beavis, BRAHMS Collaboration et al., "Quark-gluon plasma and color glass condensate at RHIC? The perspective from the BRAHMSexperiment," *Nuclear Physics A*, vol. 757, no. 1–2, pp. 1–27, 2005.

[68] B. B. Back, M. D. Baker, M. Ballintijn, PHOBOS Collaboration et al., "THE PHOBOS perspective on discoveries at RHIC," *Nuclear Physics A*, vol. 757, no. 1–2, pp. 28–101, 2005.

[69] T. Hirano and K. Tsuda, "Collective flow and two-pion correlations from a relativistic hydrodynamic model with early chemical freeze-out," *Physical Review C*, vol. 66, Article ID 054905, 2002.

[70] D. L. Adams, N. Achurin, N. I. Belikov, E704 Collaboration et al., "Measurement of single spin asymmetry for direct photon production in pp collisions at 200 GeV/c," *Physics Letters B*, vol. 345, no. 4, pp. 569–575, 1995.

[71] T. Renk, "A comprehensive description of multiple observables in heavy-ion collisions at SPS," *Journal of Physics G*, vol. 30, Article ID 064905, p. 1495, 2004.

[72] T. Renk, "Photonic measurements of the longitudinal expansion dynamics in relativistic heavy-ion collisions," *Physical Review C*, vol. 71, Article ID 064905, 2005.

[73] J.-E. Alam, S. Sarkar, T. Hatsuda, T. K. Nayak, and B. Sinha, "Photons from Pb-Pb collisions at ultrarelativistic energies," *Physical Review C*, vol. 63, Article ID 021901, 2001.

[74] D. K. Srivastava and B. Sinha, "Radiation of single photons from Pb+Pb collisions at relativistic energies and the quark-hadron phase transition," *Physical Review C*, vol. 64, Article ID 034902, 2001.

[75] P. Huovinen, P. V. Ruuskanen, and S. S. Räsänen, "Photon emission in heavy ion collisions at the CERN SPS," *Physics Letters, Section B*, vol. 535, no. 1–4, pp. 109–116, 2002.

[76] K. Gallmeister, B. Kämpfer, and O. P. Pavelenko, "Unique large thermal source of real and virtual photons in the reactions Pb(158A GeV) + Pb, Au," *Physical Review C*, vol. 62, Article ID 057901, 2000.

[77] F. D. Steffen and M. H. Thoma, "Hard thermal photon production in relativistic heavy ion collisions," *Physics Letters B*, vol. 510, no. 1–4, pp. 98–106, 2001.

[78] R. Chatterjee, D. K. Srivastava, and S. Jeon, "Single photons from relativistic collisions of lead nuclei at energies available at the CERN Super Proton Synchrotron (SPS): a reanalysis," *Physical Review C*, vol. 79, Article ID 034906, 2009.

[79] A. Adare, S. Afanasiev, C. Aidala, PHENIX collaboration et al., "Enhanced production of direct photons in Au+Au collisions at $\sqrt{s_{NN}}$ = 200 GeV and implications for the initial temperature," *Physical Review Letters*, vol. 104, Article ID 132301, 2010.

[80] S. S. Adler, S. Afanasiev, C. Aidala, PHENIX collaboration et al., "Suppressed π^0 Production at Large Transverse Momentum in Central Au+Au Collisions at $\sqrt{s_{NN}}$ = 200 GeV," *Physical Review Letters*, vol. 91, Article ID 072301, 2003.

[81] F. M. Liu, T. Hirano, K. Werner, and Y. Zhu, "Centrality-dependent direct photon pt spectra in Au+Au collisions at the BNL Relativistic Heavy Ion Collider (RHIC) energy $\sqrt{s_{NN}}$ = 200 GeV," *Physical Review C*, vol. 79, Article ID 014905, 2009.

[82] S. Sarkar, P. Roy, J.-E. Alam, S. Raha, and B. Sinha, "Dissipative effects in photon diagnostics of quark—gluon plasma," *Journal of Physics G*, vol. 23, p. 469, 1997.

[83] A. K. Chaudhuri, "Effect of viscosity on one dimensional hydrodynamic flow and direct photons from 200 AGeV S+Au collisions at CERN SPS," *Physica Scripta*, vol. 61, p. 311, 2000.

[84] A. K. Chaudhuri and B. Sinha, "Direct photon production from viscous quark-gluon plasma," *Physical Review C*, vol. 83, Article ID 034905, 2010.

[85] J. R. Bhatt, H. Mishra, and V. Sreekanth, "Thermal photons in QGP and non-ideal effects," *Journal of High Energy Physics*, vol. 1011, p. 106, 2010.

[86] K. Dusling, "Photons as a viscometer of heavy ion collisions," *Nuclear Physics A*, vol. 839, no. 1–4, pp. 70–77, 2010.

[87] S. Mitra, P. Mohanty, S. Sarkar, and J.-E. Alam, "Thermal radiation from an evolving viscous Quark Gluon plasma," *International Journal of Modern Physics E*, vol. 22, Article ID 1350004, 2013.

[88] D. Teaney, "Effect of shear viscosity on spectra, elliptic flow, and Hanbury Brown-Twiss radii," *Physical Review C*, vol. 68, Article ID 034913, 2003.

[89] P. Danielewicz and M. Gyulassy, "Dissipative phenomena in quark-gluon plasmas," *Physical Review D*, vol. 31, no. 1, pp. 53–62, 1985.

[90] H. B. Meyer, "Calculation of the shear viscosity in SU(3) gluodynamics," *Physical Review D*, vol. 76, Article ID 101701, 2007.

[91] P. Arnold, G. D. Moore, and L. G. Yaffe, "Transport coefficients in high temperature gauge theories: (II) Beyond leading log," *Journal of High Energy Physics*, vol. 0305, Article ID 051, 2003.

[92] J.-W. Chen, H. Dong, K. Ohnishi, and Q. Wang, "Shear viscosity of a gluon plasma in perturbative QCD," *Physics Letters, Section B*, vol. 685, no. 4-5, pp. 277–282, 2010.

[93] S. K. Das and J. Alam, "Transport coefficients of gluonic fluid," *Physical Review D*, vol. 83, Article ID 114011, 2011.

[94] Z. Xu and C. Greiner, "Shear viscosity in a Gluon gas," *Physical Review Letters*, vol. 100, Article ID 172301, 2008.

[95] K. Itakura, O. Morimatsu, and H. Otomo, "Shear viscosity of a hadronic gas mixture," *Physical Review D*, vol. 77, no. 1, Article ID 014014, 2008.

[96] A. Dobado and I. J. Llanes-Estrada, "Viscosity of meson matter," *Physical Review D*, vol. 69, Article ID 116004, 2004.

[97] P. Chakraborty and J. I. Kapusta, "Quasiparticle theory of shear and bulk viscosities of hadronic matter," *Physical Review C*, vol. 83, no. 1, Article ID 014906, 2011.

[98] A. S. Khvorostukhin, V. D. Toneev, and D. N. Voskresensky, "Viscosity coefficients for hadron and quark-gluon phases," *Nuclear Physics A*, vol. 845, no. 1–4, pp. 106–146, 2010.

[99] I. Tserruya, "Summary of low-mass dilepton and direct photon results," *Nuclear Physics A*, vol. 590, no. 1–2, pp. 127–138, 1995.

[100] J. Cleymans, J. Fingberg, and K. Redlich, "Transverse-momentum distribution of dileptons in different scenarios for the QCD phase transition," *Physical Review D*, vol. 35, pp. 2153–2165, 1987.

[101] K. Dusling and I. Zahed, "Transverse momentum spectra of dileptons measured by the NA60 Collaboration in In+In collisions at 158 GeV/nucleon," *Physical Review C*, vol. 80, no. 1, Article ID 014902, 2009.

[102] T. Altherr and P. V. Ruuskanen, "Low-mass dileptons at high momenta in ultra-relativistic heavy-ion collisions," *Nuclear Physics B*, vol. 380, no. 3, pp. 377–390, 1992.

[103] M. H. Thoma and C. T. Traxler, "Production of energetic dileptons with small invariant masses from the quark-gluon plasma," *Physical Review D*, vol. 56, no. 1, pp. 198–202, 1997.

[104] E. V. Shuryak, "Correlation functions in the QCD vacuum," *Reviews of Modern Physics*, vol. 65, pp. 1–46, 1993.

[105] R. Barate, D. Buskulic, D. Decamp, ALEPH Collaboration et al., "Measurement of the axial-vector τ spectral functions and determination of $\alpha_3(M_\tau^2)$ from hadronic τ decays," *The European Physical Journal C*, vol. 4, no. 3, pp. 409–431, 1998.

[106] K. Ackerstaff, G. Alexander, J. Allison et al., "Measurement of the strong coupling constant and the vector α_3 and axial-vector spectral functions in hadronic tau decays," *The European Physical Journal C*, vol. 7, pp. 571–593, 1999.

[107] S. Sarkar, "Hadrons at finite temperature," *Nuclear Physics A*, vol. 862-863, pp. 13–19, 2011.

[108] S. Mallik and S. Sarkar, "Vector and axial-vector mesons at finite temperature," *The European Physical Journal C*, vol. 25, pp. 445–452, 2002.

[109] S. Ghosh, S. Mallik, and S. Sarkar, "Analytic structure of ρ meson propagator at finite temperature," *The European Physical Journal C*, vol. 70, pp. 251–262, 2010.

[110] S. Ghosh and S. Sarkar, "ρ self-energy at finite temperature and density in the real-time formalism," *Nuclear Physics A*, vol. 870-871, no. 1, pp. 94–111, 2011.

[111] S. Ghosh and S. Sarkar, "Analysis of self-energy at finite temperature and density in the real-time formalism," *The European Physical Journal A*, vol. 49, article 97, 2013.

[112] S. Sarkar and S. Ghosh, "In-medium vector mesons and low mass lepton pairs from heavy ion collisions," *Journal of Physics*, vol. 374, Article ID 012010, 2012.

[113] J. K. Nayak, J.-E. Alam, T. Hirano, S. Sarkar, and B. Sinha, "Muon pairs from In + In collision at energies available at the CERN Super Proton Synchrotron," *Physical Review C*, vol. 85, Article ID 064906, 2012.

[114] R. Arnaldi, R. Averbeck, K. Banicz et al., "First measurement of the ρ spectral function in high-energy nuclear collisions," *Physical Review Letters*, vol. 96, Article ID 162302, 2006.

[115] R. Arnaldi, R. Averbeck, K. Banicz et al., "Evidence for radial flow of thermal dileptons in high-energy nuclear collisions," *Physical Review Letters*, vol. 100, Article ID 022302, 2008.

[116] V. L. Eletsky, M. Belkacem, P. J. Ellis, and J. I. Kapusta, "Properties of ρ and ω mesons at finite temperature and density as inferred from experiment," *Physical Review C*, vol. 64, Article ID 035202, 2001.

[117] H. Van Hees and R. Rapp, "Comprehensive interpretation of thermal dileptons measured at the CERN super proton synchrotron," *Physical Review Letters*, vol. 97, no. 10, Article ID 102301, 2006.

[118] R. Rapp, G. Chanfray, and J. Wambach, "Rho Meson propagation and dilepton enhancement in hot hadronic matter," *Nuclear Physics A*, vol. 617, pp. 472–495, 1997.

[119] A. Toia and PHENIX Collaboration, "e^+e^- pairs: a clock and a thermometer of heavy ion collisions," *Journal of Physics G*, vol. 35, Article ID 104037, 2008.

[120] A. Adare, S. Afanasiev, C. Aidala, PHENIX Collaboration et al., "Detailed measurement of the e^+e^- pair continuum in p+p and Au+Au collisions at $\sqrt{s_{NN}}$ = 200 GeV and implications for direct photon production," *Physical Review C*, vol. 81, Article ID 034911, 2010.

[121] P. Lichard and J. Jura, "Electron-positron annihilation into four charged pions and the $a_1\rho\pi$ Lagrangian," *Physical Review D*, vol. 76, Article ID 094030, 2007.

[122] K. Aamodt, N. Abel, U. Abeysekara, ALICE collaboration et al., "Charged-particle multiplicity measurement in proton-proton collisions at $\sqrt{s}$ = 0.9 and 2.36 TeV with ALICE at LHC," *The European Physical Journal C*, vol. 68, pp. 89–108, 2010.

[123] F. -M. Liu, T. Hirano, K. Werner, and Y. Zhu, "Centrality-dependent direct photon p_t spectra in Au+Au collisions at the BNL Relativistic Heavy Ion Collider (RHIC) energy $\sqrt{s_{NN}}$ = 200 GeV," *Physical Review C*, vol. 79, Article ID 014905, 2009.

[124] B. Schenke, S. Jeon, and C. Gale, "(3+1)D hydrodynamic simulation of relativistic heavy-ion collisions," *Physical Review C*, vol. 82, Article ID 014903, 2010.

[125] B. Schenke, S. Jeon, and C. Gale, "Higher flow harmonics from (3+1)D event-by-event viscous hydrodynamics," *Physical Review C*, vol. 85, Article ID 024901, 2012.

[126] J. K. Nayak and J. Alam, "Measuring radial flow of partonic and hadronic phases in relativistic heavy-ion collisions," *Physical Review C*, vol. 80, Article ID 064906, 2009.

[127] B. Sinha, "Universal signals of a quark-gluon plasma," *Physics Letters B*, vol. 128, no. 1-2, pp. 91–94, 1983.

[128] R. Chatterjee, E. S. Frodermann, U. Heinz, and D. K. Srivastava, "Elliptic flow of thermal photons in relativistic nuclear collisions," *Physical Review Letters*, vol. 96, no. 20, Article ID 202302, 2006.

[129] R. Hanbury Brown and R. Q. Twiss, "A test of a new type of stellar interferometer on sirius," *Nature*, vol. 178, pp. 1046–1048, 1956.

[130] D. Peressounko, "Hanbury Brown-Twiss interferometry of direct photons in heavy ion collisions," *Physical Review C*, vol. 67, Article ID 014905, 2003.

[131] Y. M. Sinyukov, "Hanbury Brown/Twiss correlations for expanding hadron and quark-gluon matter," *Nuclear Physics A*, vol. 498, pp. 151–159, 1989.

[132] A. Adare, S. Afanasiev, C. Aidala et al., "Energy loss and flow of heavy Quarks in Au+Au collisions at $\sqrt{s_{NN}}$ = 200 GeV," *Physical Review Letters*, vol. 98, Article ID 172301, 2007.

[133] B. Abelev, B. Abelev, A. A. Quintana, The ALICE Collaboration et al., "Charged-particle multiplicity density at Midrapidity in central Pb-Pb collisions at $\sqrt{s_{NN}}$ = 2.76 TeV," *Physical Review Letters*, vol. 105, Article ID 252301, 2010.

[134] S. Pratt, "Pion interferometry for exploding sources," *Physical Review Letters*, vol. 53, no. 13, pp. 1219–1221, 1984.

[135] S. Pratt, "Pion interferometry of quark-gluon plasma," *Physical Review D*, vol. 33, pp. 1314–1327, 1986.

[136] U. A. Widemann and U. Heinz, "Particle interferometry for relativistic heavy-ion collisions," *Physics Reports*, vol. 319, no. 4–5, pp. 145–230, 1999.

[137] U. Heinz and B. V. Jacak, "Two-particle correlations in relativistic heavy-ion collisions," *Annual Review of Nuclear and Particle Science*, vol. 49, no. 1, pp. 529–579, 1999.

[138] T. Csörgő and B. Lörstad, "Bose-Einstein correlations for three-dimensionally expanding, cylindrically symmetric, finite systems," *Physical Review C*, vol. 54, pp. 1390–1403, 1996.

[139] D. H. Rischke and M. Gyulassy, "The time-delay signature of quark-gluon plasma formation in relativistic nuclear collisions," *Nuclear Physics A*, vol. 608, no. 4, pp. 479–512, 1996.

[140] S. Chapman, P. Scotto, and U. Heinz, "New cross term in the two-particle Hanbury-Brown-Twiss correlation function in ultrarelativistic heavy-ion collisions," *Physical Review Letters*, vol. 74, no. 22, pp. 4400–4403, 1995.

[141] M. Herrmann and G. F. Bertsch, "Source dimensions in ultrarelativistic heavy-ion collisions," *Physical Review C*, vol. 51, pp. 328–338, 1995.

[142] P. Huovinen and P. V. Ruuskanen, "Hydrodynamic models for heavy ion collisions," *Annual Review of Nuclear and Particle Science*, vol. 56, pp. 163–206, 2006.

[143] R. Chatterjee, D. K. Srivastava, U. W. Heinz, and C. Gale, "Elliptic flow of thermal dileptons in relativistic nuclear collisions," *Physical Review C*, vol. 75, Article ID 054909, 2007.

[144] R. Chatterjee, D. K. Srivastava, U. W. Heinz, and C. Gale, "Elliptic flow of thermal dileptons in relativistic nuclear collisions," *Physical Review C*, vol. 75, Article ID 054909, 2007.

[145] J. Deng, Q. Wang, N. Xu, and P. Zhuang, "Dilepton flow and deconfinement phase transition in heavy ion collisions," *Physics Letters B*, vol. 701, pp. 581–586, 2011.

[146] H. Van Hees, C. Gale, and R. Rapp, "Thermal photons and collective flow at energies available at the BNL relativistic heavy-ion collider," *Physical Review C*, vol. 84, no. 5, Article ID 054906, 2011.

[147] T. Renk and J. Ruppert, "Dimuon transverse momentum spectra as a tool to characterize the emission region in heavy-ion

collisions," *Physical Review C*, vol. 77, no. 2, Article ID 024907, 2008.

[148] V. Roy and A. K. Choudhuri, "Charged particle's elliptic flow in (2+12+1)D viscous hydrodynamics at LHC ($\sqrt{s}$ = 2.76 TeV) energy in Pb + Pb collision," *Physics Letters B*, vol. 703, no. 3, pp. 313–317, 2011.

[149] B. Mohanty and J. Alam, "Velocity of sound in relativistic heavy-ion collisions," *Physical Review C*, Article ID 064903, 2003.

[150] K. Aamodt, A. Abrahantes Quintana, D. Adamova', ALICE Collaboration et al., "Centrality dependence of the charged-particle multiplicity density at midrapidity in Pb-Pb collisions at $\sqrt{s_{NN}}$ = 2.76TeV," *Physical Review Letters*, vol. 106, Article ID 032301, 2011.

[151] K. Aamodt, A. Abrahantes Quintana, D. Adamova', ALICE Collaboration et al., "Suppression of charged particle production at large transverse momentum in central Pb-Pb collisions at $\sqrt{s_{NN}}$ = 2.76 TeV," *Physics Letters B*, vol. 696, p. 30, 2011.

[152] K. Itakura, "Strong-field physics as a new probe of early-time dynamics in heavy-ion collisions," *Journal of Physics*, vol. 422, Article ID 012029, 2013.

[153] K. Tuchin, "Photon decay in a strong magnetic field in heavy-ioncollisions," *Physical Review C*, vol. 83, Article ID 017901, 2011.

[154] K. Tuchin, "Electromagnetic radiation by quark-gluon plasma in a magnetic field," *Physical Review C*, vol. 87, Article ID 024912, 2013.